ADVANCED OPTICAL DIAGNOSTICS FOR DUST CLOUD PARTICLE, FLOW, AND COMBUSTION MEASUREMENTS IN A MINIMUM IGNITION ENERGY TESTING DEVICE

A Dissertation

by

CHRISTIAN M. SCHWEIZER

Submitted to the Office of Graduate and Professional Studies of
Texas A&M University
in partial fulfillment of the requirements for the degree of

DOCTOR OF PHILOSOPHY

Chair of Committee,	Waruna D. Kulatilaka
Co-Chair,	Chad V. Mashuga
Committee Members,	Eric L. Petersen
	Timothy J. Jacobs
Head of Department,	Guillermo Aguilar

August 2023

Major Subject: Mechanical Engineering

ABSTRACT

Dust explosions threaten people, assets, and the environment across a wide range of industries. To identify hazards and manage risks, dust materials must be tested with standard methods and equipment like the MIKE3 minimum ignition energy (MIE) testing device. The MIKE3 device, while important for safety testing, is also appealing for the scientific investigation of dust cloud ignitability. Dust explosion conditions in the MIKE3 device can be easily controlled, and the resulting MIE data is easily interpreted within the context of industrial safety. However, conventional MIE measurements are not sufficient to resolve the multi-scale physics and chemistry of dust explosions, and advanced methods must be developed to probe the dust cloud dispersion, ignition, and flame propagation processes that evolve inside the MIKE3 device. Optical diagnostics offer promising pathways to new experimental investigations with the MIKE3 device through in-situ, non-intrusive, multi-scale, and multi-dimensional measurement capabilities. Therefore, the objective of this research is to develop advanced optical diagnostics for novel dust cloud particle, flow, and combustion measurements that are compatible with the MIKE3 device over a wide range of relevant material types and testing conditions.

Firstly, particle and flow diagnostics were implemented to investigate the dynamics of dust clouds prior to ignition. Digital in-line holography (DIH) was implemented during the dust cloud dispersion process for micro-scale particle detection and tracking in three-dimensional (3D) space. Quantitative particle size, concentration, and velocity measurements revealed how different dust sample properties can influence the observed characteristics of the dust cloud in the ignition zone. Next, particle image velocimetry (PIV) was combined with DIH in the MIKE3 glass tube for micro-scale particle diagnostics, macro-scale flow visualizations, and two-dimensional (2D) flow velocity and vorticity field measurements. Multiple experimental runs were repeated to accommodate the stochastic dust cloud dispersion process, and key particle and flow statistics were assessed.

Secondly, combustion diagnostics were implemented to investigate the ignition and flame propagation behaviors of combustible dusts. Broadband imaging and excited-state hydroxyl (OH*) and methylidyne (CH*) chemiluminescence imaging were implemented to obtain quantitative size, position, and velocity measurements during the early flame kernel development process. An asymmetric motion of the flame kernel away from the central ignition zone was discovered, and differences between organic and metal dust cloud ignition were identified. Finally, hydroxyl planar laser-induced fluorescence (OH-PLIF) imaging was implemented to analyze the 2D flame structure of burning dust clouds. OH-PLIF images were used to visualize the flame structure and categorize flames based on their qualitative features. Quantitative flame area and curvature measurements were then used to characterize the expanding flame surface.

Overall, the completed research represents significant forward progress for dust explosion diagnostics research. The developed methods leverage the capabilities of advanced imaging devices, lasers, and instrumentation while remaining compatible with the geometry and operation of the MIKE3 device. This research has enhanced our fundamental understanding of dust explosions, produced valuable validation data for numerical dust explosion models, and provided dust cloud ignitability insights that are relevant to industrial safety.

DEDICATION

To my friends and family.

ACKNOWLEDGMENTS

I would like to thank my advisor Dr. Waruna Kulatilaka for his unwavering support and guidance throughout my time at Texas A&M University. I thank him for introducing me to a challenging research topic and helping me grow as an engineer, a researcher, a teacher, and a person. I would also like to thank Dr. Chad Mashuga for serving as my secondary advisor. He graciously provided access to the MIKE3 device and his expertise in the area of safety, without which this research would not be possible. Additionally, I thank Dr. Eric Petersen and Dr. Timothy Jacobs for serving on my committee and providing helpful feedback for my research. Thanks must also go to the members of Dr. Mashuga's research group and my colleagues in the Optical Diagnostics and Imaging Laboratory for engaging with me in many fruitful research discussions and providing much-appreciated experimental assistance. Finally, I thank my friends and family for their unconditional love and support.

CONTRIBUTORS AND FUNDING SOURCES

Contributors

This work was supervised by a dissertation committee consisting of Dr. Waruna D. Kulatilaka (advisor, chair), Dr. Eric L. Petersen, and Dr. Timothy J. Jacobs of the J. Mike Walker '66 Department of Mechanical Engineering, along with Dr. Chad V. Mashuga (co-chair) of the Artie McFerrin Department of Chemical Engineering.

All work for this dissertation was completed by the student, with experimental setup and operation assistance from Matthew Hay, Pradeep Parajuli, and Yejung Wang of the J. Mike Walker '66 Department of Mechanical Engineering, along with Pranav Bagaria, Colson Johnson, Shrey Prasad, and Ankit Saini of the Artie McFerrin Department of Chemical Engineering.

Funding Sources

Funding and facilities support for this research was provided by the J. Mike Walker '66 Department of Mechanical Engineering, the Mary Kay O'Connor Process Safety Center, the Texas A&M Engineering Experiment Station (TEES) Tubomachinery Laboratory, and Eli Lilly and Company.

NOMENCLATURE

ABBREVIATIONS AND ACRONYMS

2D	Two-dimensional
3D	Three-dimensional
ASTM	American Society for Testing and Materials
Al	Aluminum atom
C	Carbon atom
CCD	Charge-coupled device
CDF	Cumulative distribution function
CH*	Excited-state methylidyne radical
CMOS	Complementary metal-oxide semiconductor
COV	Coefficient of variation
DIH	Digital in-line holography
FFT	Fast Fourier Transform
H	Hydrogen atom
HWA	Hot-wire anemometry
ICCD	Intensified charge-coupled device
LDV	Laser-doppler velocimetry
LIF	Laser-induced fluorescence
MIE	Minimum ignition energy
N	Nitrogen atom
O	Oxygen atom
OH	Hydroxyl radical
OH*	Excited-state hydroxyl radical

PDF	Probability density function
PIV	Particle image velocimetry
PLIF	Planar laser-induced fluorescence
PSM	Process safety management
RBPS	Risk based process safety
SMD	Sauter mean diameter
SNR	Signal-to-noise ratio
SSA	Specific surface area
UV	Ultraviolet

TABLE OF CONTENTS

LIST OF FIGURES

LIST OF TABLES

TABLE Page

1. INTRODUCTION

1.1 Background

Why do we study dust explosions? More than 3,000 dust explosion accidents have occurred around the world since the first reported case in 1785 [1]. These explosions have caused serious and often catastrophic harm to people, assets, and the environment [1–4]. A wide range of industries are vulnerable to dust explosions because many materials can cause an explosion when in dust form, including wood, food, pharmaceuticals, plastics, metals, and coal [5]. Additionally, combustible dust can exist as a raw material, intermediate product, incidental byproduct, and finished good. Therefore, there are many opportunities for combustible dust hazards to arise in an industrial facility. These hazards may then remain unrecognized until a dust explosion occurs. Furthermore, seemingly isolated hazards can quickly spread to other parts of an industrial plant. For example, the blast wave from a primary dust explosion can disturb nearby accumulated dust layers and initiate extensive secondary dust explosions [5].

While the number of dust explosions worldwide has generally decreased, accidents are likely to continue as global industrialization increases [1]. Unique hazards may also arise as new materials, processes, and products are invented. It is expected that dust explosions will continue to threaten industries around the world, and thus a considerable amount of effort has been devoted to developing systematic and consensus approaches to dust explosion loss prevention [6–8]. A foundational element of modern Process Safety Management (PSM) systems and the risk based process safety (RBPS) framework is identifying and understanding hazards so that they can be effectively avoided or controlled [9]. Therefore, we study dust explosions and the hazards that cause them to prevent future accidents and mitigate their damaging effects.

How can optical diagnostics help us understand dust explosions? Dust explosions are fundamentally interesting because they are a complex example of solids combustion. The characteristics of a dust explosion depend on many factors, such as the type of fuel material, the composition of the oxidizer, the degree of dispersion and confinement, and the properties of the ignition source. Since a dust cloud is a two-phase mixture of solid particles and gaseous oxidizer, dust cloud combustion will involve both heterogeneous and homogeneous chemical reactions. Additionally, multi-phase flow, turbulence, and radiation effects will influence the dispersion and combustion of the dust cloud [10]. If dust explosions are to be fully understood, these complex phenomena must be comprehensively measured.

While many techniques are available to study dust explosions, optical approaches offer several key advantages for measuring the dust cloud dispersion, ignition, and flame propagation processes. Unlike physical probes, cameras can non-intrusively image the dust cloud from a safe distance and laser probes can traverse the measurement space with minimal effect on the flow or chemistry. Optical diagnostics can thus be implemented for in-situ measurements in extreme environments, where physical probes might disturb the dust cloud or be damaged from the combustion. Finally, modern high-speed cameras enable time-resolved investigations, and sophisticated lens and laser configurations allow for 2D and 3D measurements at the relevant spatial scale. Therefore, optical diagnostics offer us new ways to observe and measure the physics and chemistry of dust explosions.

How can the MIKE3 device help us understand dust explosions? The MIKE3 device is used to measure the minimum ignition energy (MIE) of a dust cloud. The MIE of a dust cloud is the lowest energy required to ignite the combustible mixture with a high-voltage spark discharge [11], and is an important parameter to consider during dust explosion risk assessment. To make measurements, the MIKE3 device creates a dust cloud inside an vertical glass tube with a burst of compressed air and initiates a spark discharge at a predefined time and energy. To ensure the production of accurate MIE data, the MIKE3 device operates in accordance with standards like ASTM E2019 [11] and ISO/IEC 80079-20-2 [12]. Additionally, the current manufacturer of the MIKE3 device (Cesana AG) hosts regular calibration round robins [13], whereby dust samples are distributed to laboratories around the world for testing. Measurements from the participants are then used to calculate reference MIE values and determine equipment calibration requirements. Therefore, the MIKE3 device provides us with a reliable testing system for producing dust explosions and trusted MIE data.

1.2 Significance of the Research

The primary thrust of this research is to leverage the MIKE3 device as a platform for comprehensive dust explosion investigations. Since the MIKE3 is already used for standard dust cloud MIE measurements in industry, it can also be used to reliably reproduce dust explosions for new experimental studies. Importantly, the MIKE3 device has a simple and optically accessible geometry, which permits the dust cloud dispersion, ignition, and flame propagation processes to be measured by cameras, lasers, and other sensors. Therefore, optical measurements inside the MIKE3 device can probe the fundamental physics and chemistry of dust explosions within the standardized ignitability testing framework that is familiar to industry. ***Through the comprehensive measurement of the pre- and post-ignition processes occurring in dust clouds, this research sets out to expand the current knowledge of the complex particle, flow, and combustion behaviors that constitute dust explosions.***

From this research, new particle, flow, and combustion measurements will provide experimental evidence to support specific hypotheses about dust cloud ignitability that cannot be assessed by standard ignitability and explosibility parameters alone. Furthermore, experimental investigations with the MIKE3 device will provide validation data for numerical dust explosion models. Finally, new insights will promote the improvement of the next generation of combustible dust testing standards and equipment. Thus, this research will improve our fundamental understanding of dust explosions and produce practical safety insights for industry as well. However, to achieve these benefits, the unique constraints associated with the MIKE3 device, the wide range of dust materials and test conditions, and the complex nature of dust explosions must be considered. Strategies must also be developed to interpret the new measurements in relation to conventional dust explosion hazard data.

1.3 Research Outline

The overall goal of this research is to develop advanced optical diagnostics for novel dust cloud particle, flow, and combustion measurements that are compatible with the MIKE3 device over a wide range of relevant material types and testing conditions. To achieve this goal, the research is sub-divided into four main tasks: (i) characterization of the particle cloud near the spark gap prior to ignition, (ii) combined characterization of the flow structures and particle distributions in the dust cloud prior to ignition, (iii) characterization of the flame kernel dynamics at the onset of dust cloud ignition and early times after, and (iv) characterization of the reaction zone and flame propagation after dust cloud ignition.

Accordingly, the following four optical/laser diagnostic experiments are completed for this research: (a) digital in-line holography (DIH) for dust cloud particle diagnostics prior to ignition, (b) combined digital in-line holography (DIH) and particle image velocimetry (PIV) for dust cloud particle and flow diagnostics prior to ignition, (c) chemiluminescence imaging for dust cloud ignition diagnostics, and (d) hydroxyl planar laser-induced fluorescence (OH-PLIF) imaging for dust cloud combustion diagnostics after ignition.

Given these tasks and their corresponding experiments, this dissertation is structured as follows. Chapter 2 provides a review of dust explosions, particle size distributions, DIH, PIV, chemiluminescence imaging, and PLIF. Chapters 3 and 4 present work on DIH and PIV for new dust cloud particle and flow measurements prior to ignition. Chapter 5 presents work on chemiluminescence imaging for new dust cloud ignition measurements. Chapter 6 presents work on OH-PLIF for new dust flame measurements after ignition. Finally, concluding remarks and areas for future study are given in Chapter 7.

2. LITERATURE REVIEW

2.1 Introduction to Dust Explosions

A dust explosion can be defined as the rapid combustion of finely divided solid material that is confined and suspended in a gaseous oxidizer [5]. Five elements are required for a dust explosion to occur: fuel (combustible dust), oxidizer, dispersion of the dust to create a dust cloud, confinement of the combustible mixture, and a sufficiently energetic ignition source. These elements are depicted with the "dust explosion pentagon" in Fig. 2.1, which is a helpful conceptual model for understanding the simultaneous requirements for a dust explosion [6]. If at least one element is missing from the pentagon, a dust explosion cannot occur. When contrasted with the familiar "fire triangle", which can also be seen in Fig. 2.1, we see that dispersion and confinement are additional requirements for a dust explosion. This is because the fuel is in the solid phase and must be suspended in the surrounding oxidizer with a sufficient concentration. Partial or total confinement of the combustible mixture then enables the development of an overpressure that can damage equipment and cause nearby dust layers to be lifted into the air.

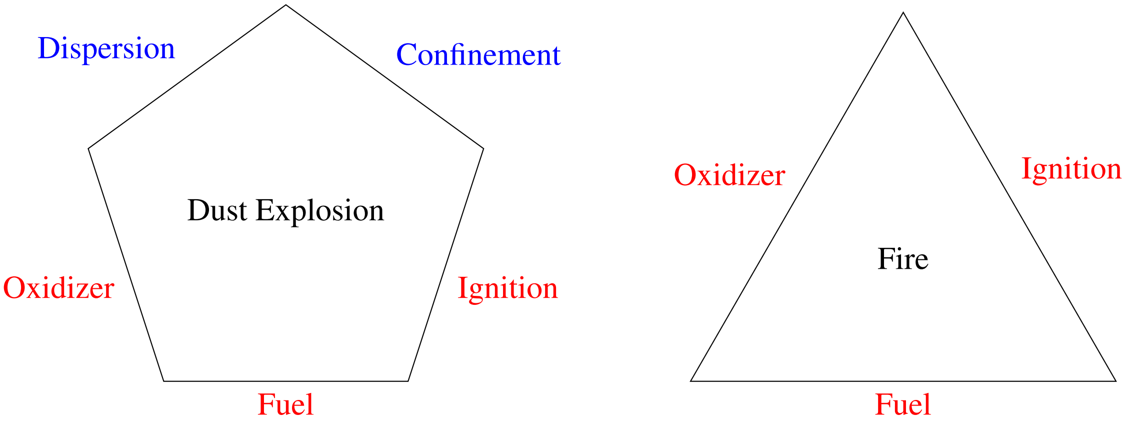

Figure 2.1: The dust explosion pentagon and the fire triangle. Common elements between the pentagon and the triangle are labeled in red. Additional dust explosion causation factors are labeled in blue. Adapted from [6].

Combustible dust, which serves as the fuel for a dust explosion, can be defined as any finely divided solid material that creates a flash fire or explosion hazard when suspended in a gaseous oxidizer [14]. Combustible dusts can also be defined according to a 500-μm size criterion (capable of passing through a U.S. No. 35 standard sieve), as dusts that are greater than this size are unlikely to produce the aforementioned hazards. While this size criterion may serve as a helpful rule-of-thumb, the evaluation of combustible dust hazards should be ultimately determined by standard screening procedures and test data. Nevertheless, this definition of a combustible dust emphasizes the importance of dust fineness, or the degree of subdivision, to the associated hazard. In general, combustible dusts that are more finely divided, up to a limit, will be easier to ignite and cause more damage [5]. Dust fineness can be characterized by the specific surface area (SSA), or the total amount of surface area per unit of mass. For a poly-sized collection of spherical particles, the SSA is given by:

$$S = \frac{6}{\rho D(3,2)}. \tag{2.1}$$

Here S is the SSA, ρ is the dust material density, and $D(3,2)$ is the Sauter mean diameter (SMD). The SMD of a poly-sized collection of spherical particles is the diameter of a particle with the same volume-to-surface-area ratio as the entire collection. Alternatively, the SMD defines a hypothetical mono-sized collection of particles with a total volume and surface area that is equivalent to the original poly-sized particle collection [15]. The SSA and SMD establish intuitive notions of dust fineness and enable different particle size distributions to be described and compared. Additionally, the SSA and SMD can be independently measured via adsorption methods or particle size analysis, respectively [16]. Thus, Eq. (2.1) is useful for relating the two quantities, especially when one is easier to measure. While particle size and surface area are the primary factors that influence the likelihood and severity of a dust explosion, other dust properties must also be considered, such as the particle size polydispersity (distribution of sizes), morphology (shape), and chemical composition (dust material).

2.1.1 Dust Explosion Risk Analysis

Risk analysis provides a useful framework to prevent dust explosions and mitigate their damaging effects to industrial systems. To understand the fundamental elements of risk analysis, it is important to distinguish between the central concepts of "hazard" and "risk". Firstly, a hazard can be defined as the inherent potential for something (machines, materials, processes, conditions, etc.) to cause damage to people, assets, the environment, or anything else that we value. Conversely, risk represents a measure of potential loss due to an exposure to one or more hazards. The risk depends on the specific nature of the hazard exposure, and therefore it conveys additional information about the likelihood and severity of an undesired outcome. These definitions reveal that industrial facilities can be exposed to different risks, even if they contain identical hazards. Therefore, risk analysis is the process of assessing, managing, and communicating risk [17]. These core activities aim to eliminate risk or reduce it to a level which is "As Low As Reasonably Practicable" (ALARP), whereby the costs of reducing the risk even further would be grossly disproportionate to the benefit gained. In other words, risk reduction must be balanced against the time, effort, and resources that must be expended to achieve it.

Risks can be qualitatively or quantitatively evaluated by performing a risk assessment. Risk assessment can be succinctly summarized as the process of answering three basic questions [18]: (1) What can go wrong? (2) How likely is it to happen? (3) What are the consequences of it happening? These three questions emphasize that in order to adequately assess risks, we must identify scenarios that could lead to undesirable outcomes, estimate the probabilities of these scenarios, and estimate the severity of the outcomes.

In dust explosion risk assessment, we must identify combustible dust hazards and scenarios in which the conditions required for a dust explosion are satisfied. Several ignitability and explosibility parameters can then be measured to assess the probability of ignition and the severity of the resulting explosion, respectively. These parameters, along with plant-specific knowledge, will inform how explosion prevention and mitigation measures are implemented to reduce dust explosion risks. Examples of these parameters are the minimum ignition energy (MIE), minimum explosible concentration (MEC), minimum oxygen concentration (MOC), maximum explosion pressure P_{max}, maximum rate of pressure rise $(dP/dt)_{\text{max}}$, and the dust deflagration index K_{st}. The primary focus of this work is the MIE, which predicts the likelihood of dust cloud ignition from an electrostatic discharge. Since ignition sensitivity will vary according to the specific dust, MIE measurements are essential for implementing appropriate strategies to control static electricity hazards. For example, powder handling or collection systems may require bonding and grounding to prevent sparks from forming in dusty and confined spaces. If ignition sources cannot be eliminate, an inerting procedure may also be implemented to reduce oxidizer concentrations in the area of concern [19].

2.1.2 Prior Dust Cloud MIE Research

Although the MIE has been indispensable as a standard indicator of relative ignition sensitivity, it was recognized relatively early on that dust clouds are not characterized by the MIE as simply as combustible gas mixtures. Early studies demonstrated that dust cloud ignitability is strongly influenced by the spark circuit's series resistance [20], and that sufficiently short sparks can potentially inhibit ignition by removing combustible material from the ignition zone [21]. Additionally, many studies have demonstrated that dust characteristics like particle size [22–24], polydispersity [25], and morphology [26–28] can influence the measurement of the MIE as well. As alluded to above, aspects of the testing environment, such as the spark discharge method [29–31], oxidizer composition [32–34], and turbulence levels [35] can also lead to varied MIE results. These findings are consistent with the aforementioned dust explosion pentagon in Fig. 2.1, and suggest that each of the essential causation factors can influence the measured MIE [6]. While these previous investigations have clearly demonstrated the complex dependencies of the MIE, there is still a considerable lack of evidence for explaining the mechanisms that produce these dependencies.

2.2 Dust Particle Size Distributions

While it is often beneficial to assume that all of the particles in a dust cloud are the same size, in most cases the particles will span a range of different sizes. Thus, a robust theoretical understanding of particle size distributions is required to qualitatively and quantitatively describe different dust particle systems. Since dust samples often comprise a very large number of particles, statistical methods can be applied to particle size distributions to characterize their properties.

As a starting point, the size distribution of a collection of poly-sized spherical particles can be assessed with a histogram, whereby the different particle diameters are organized into discrete intervals or size classes [36]. These intervals, also know as bins, must be adjacent and span the full range of possible sizes from the smallest to largest diameter $[D_{\text{min}}, D_{\text{max}}]$. Additionally, the bin width Δ_i must be carefully chosen to accurately depict the shape of the distribution. Finally, the height of each bin must be proportional to the number of particles in each size class. The procedure for constructing a histogram to represent the particle size distribution is given below.

First, the height of the i^{th} bin is given by $n(D_i) = n_i$, where D_i is the midpoint diameter of the size class and n_i is the number of particles in the interval. Next, the bin height is scaled to the proportion $p(D_i) = n_i / \sum_i n_i = n_i/N$, which estimates the probability of finding a particle in the given size class. The proportions given by $p(D_i)$ have the usual probability properties whereby $0 \leq p(D_i) \leq 1$ and $\sum_i p(D_i) = 1$. While the bin heights provided by $n(D_i)$ and $p(D_i)$ are a helpful starting point, the computed values are ultimately dependent on the bin width. Therefore, the bin height is scaled again to remove the bin width dependence. The final histogram bin height is thus determined by the probability density given by:

$$f(D_i) = \frac{p(D_i)}{\Delta_i} = \frac{n_i}{\Delta_i \, N}. \tag{2.2}$$

Accordingly, the probability is proportional to the area of the bin $f(D_i)\Delta_i$ and the sum of all probabilities is maintained, with $\sum_i f(D_i)\Delta_i = 1$. An example histogram showing a distribution of particle sizes can be seen in Fig. 2.2. Even with discrete rectangular bins, the histogram bin height closely matches the shape of the continuous theoretical curve, which is also known as the probability density function (PDF). Using smaller bins would result in an even better match. In other words, as the bin width becomes infinitesimally small ($\Delta_i \rightarrow dD$), the probability density approaches the continuous PDF [36]. The continuous function is expressed as $f_0(D)$ and is named the "number PDF" since it is derived from the number of particles found in a given size interval.

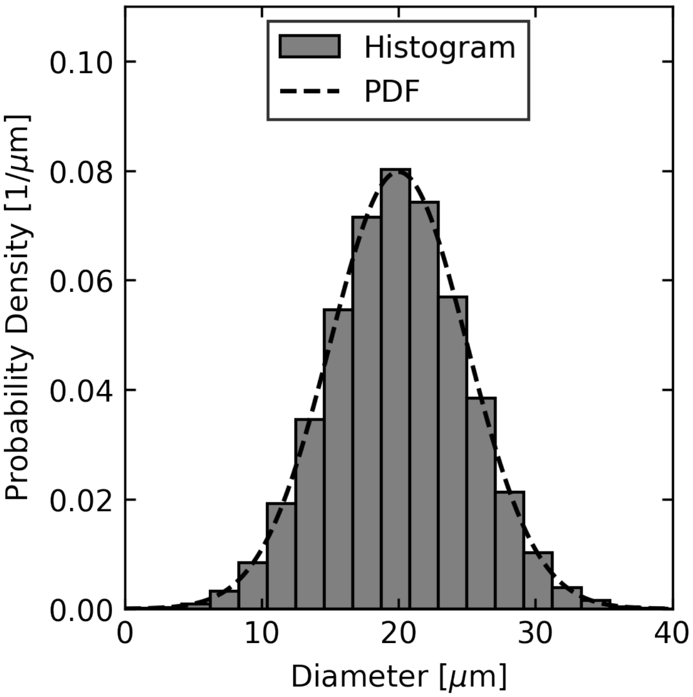

Figure 2.2: Example histogram showing a particle size distribution. The underlying particle data was randomly sampled from a normal (Gaussian) distribution with a mean of 20 µm and standard deviation of 5 µm.

For the random variable $\mathcal{D}$, the quantity $f_0(D)\,dD$ represents the probability of finding a particle with diameter $\mathcal{D}$ in the interval $[D, D + dD]$. The number PDF can thus be defined in integral form with:

$$\int_a^b f_0(D)\,dD = P[a \leq \mathcal{D} \leq b]. \tag{2.3}$$

The number PDF is non-negative everywhere and is normalized such that the integral $\int_{-\infty}^{+\infty} f_0(D)\,dD = 1$. The number PDF can also be defined in terms of the number cumulative distribution function (CDF), which yields the accumulated probability up to a given diameter. The number CDF is given by:

$$F_0(D) = P[\mathcal{D} \leq D] = \int_{-\infty}^{D} f_0(D)\, dD. \tag{2.4}$$

From these definitions it can be seen that probabilities are integrals of the PDF and ordinate intercepts of the CDF. Familiar statistical quantities like the mean, median, mode, variance, standard deviation, and coefficient of variation can now be defined with respect to the number PDF and CDF [37].

2.2.1 Measures of Location

Mean, Median, and Mode

The arithmetic mean diameter of a particle size distribution is the mathematical expectation of the random variable $\mathcal{D}$, and may also be referred to as the first raw moment of $\mathcal{D}$. The arithmetic mean diameter is given by:

$$\mu = E[\mathcal{D}] = \int_{-\infty}^{+\infty} D f_0(D)\, dD. \tag{2.5}$$

The arithmetic mean diameter of the particle size distribution can be estimated with the sample arithmetic mean, given by:

$$\bar{D} = \frac{1}{N} \sum_i n_i D_i. \tag{2.6}$$

Next, the median diameter is the midpoint of the number CDF, or the diameter for which 50% of the particles are smaller and 50% are larger. The median diameter is given by:

$$F_0(m_e) = \frac{1}{2} = \int_{-\infty}^{m_e} f_0(D)\, dD. \tag{2.7}$$

Finally, the mode m_o is the diameter corresponding to the global maximum of the number PDF. A particle size distribution can also be described as multimodal if it has more than one diameter maxima. For a symmetric distribution, the mean, median, and mode are equivalent.

2.2.2 Measures of Dispersion

Variance, Standard Deviation, and Coefficient of Variation

The variance of the particle size distribution is the second central moment of $\mathcal{D}$, given by:

$$\sigma^2 = E[(\mathcal{D} - \mu)^2] = \int_{-\infty}^{+\infty} (D - \mu)^2 f_0(D)\, dD. \tag{2.8}$$

The standard deviation σ is simply the square root of the variance. It is often preferable to use the standard deviation, rather than the variance, as a measure of spread since it has the same units as the mean. The standard deviation of the particle size distribution can be estimated with the sample standard deviation, given by:

$$s = \sqrt{\frac{\sum_i n_i (D_i - \bar{D})^2}{N - 1}}. \tag{2.9}$$

Finally, the coefficient of variation (COV) expresses the variability of the particle size distribution relative to the mean. Assuming a non-zero mean, the COV is the standard deviation divided by the mean, and is estimated with $s/\bar{D}$. Therefore, the COV is unitless, and is often expressed as a percentage.

2.2.3 Weighted Probability Density Functions

As seen above, the moments of a particle size distribution are crucial for defining the familiar measures of location and dispersion such as the mean and standard deviation, respectively. Distribution moments can also be used to define other important mean particle diameters. To define generalized mean particle diameters, the notion of weighted particle size distributions and PDFs must first be presented. In general, a weighted PDF [38] is given by:

$$f_w(x) = \frac{w(x)\, f(x)}{E[w(X)]}. \tag{2.10}$$

It can be seen that the weighted PDF $f_w(x)$ is the product of the original PDF $f(x)$ and a weighting function $w(x)$. The denominator $E[w(X)]$ is the normalizing factor that keeps the area under $f_w(x)$ equal to unity. A weighting function of the form $w(x) = D^r$ is a natural choice since particle number, length, surface area, and volume are all proportional to D^r. For $w(x) = D^r$ and $f(x) = f_0(D)$, the weighted PDF becomes:

$$f_r(D) = \frac{D^r f_0(D)}{\int_{-\infty}^{\infty} D^r f_0(D) dD}. \tag{2.11}$$

Importantly, Eq. (2.11) can be used to model particle size distribution measurements from different experimental techniques, which yield results with different weighting effects [39]. For example, optical particle counters will detect particles on a number basis, yielding a primary measurement of the number PDF. Conversely, laser diffraction measurements will produce a size distribution that is weighted by particle volume. Particle size distributions can be transformed from one weighting to another in order to compare results from different measurement methods, or analyze particle data from an alternative perspective. However, care must be taken when transforming a particle size distribution from one weighting to another, as different measurement methods may have different sensitivities across the full range of size classes.

Two common transformations implement particle surface area and volume weightings. The surface-weighted PDF is given by:

$$f_2(D) = \frac{f_0(D) D^2}{\int_{-\infty}^{+\infty} f_0(D) D^2 \, dD}. \tag{2.12}$$

Similarly, the volume-weighted PDF is given by:

$$f_3(D) = \frac{f_0(D) D^3}{\int_{-\infty}^{+\infty} f_0(D) D^3 \, dD}. \tag{2.13}$$

The impact of different weightings on the shape of a particle size distribution can be seen in Fig. 2.3, which shows the number, surface-weighted, and volume-weighted PDFs of a two-component Gaussian particle size distribution. Here $f_0(D)$ shows two modes of equal height, indicating an equal number of particles from each Gaussian component. Despite this, $f_2(D)$ and $f_3(D)$ show that a greater proportion of the total surface area and volume is taken up by the larger particles in the distribution.

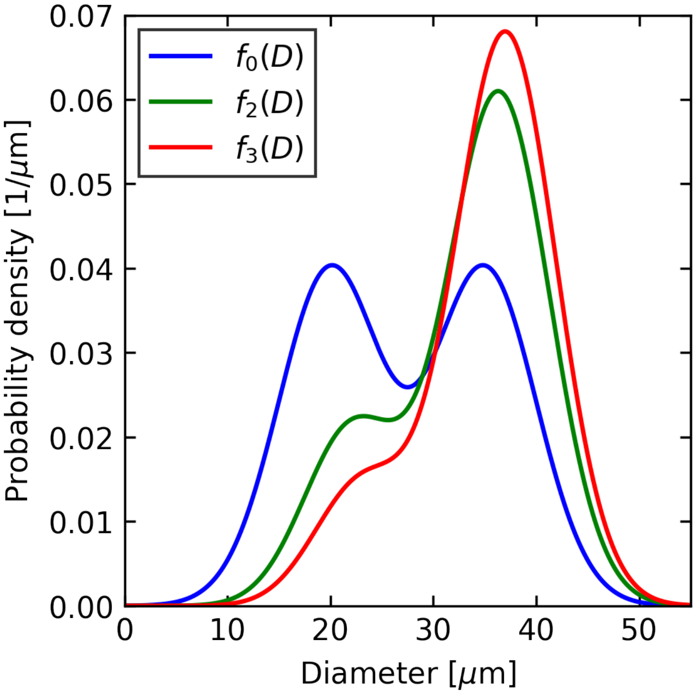

Figure 2.3: Number, surface-weighted, and volume-weighted probability density functions.

The volume-weighted PDF is frequently used because it represents the composition of the sample in terms of the easily-measured volume or mass. Volume percentile diameters are then commonly used to characterize the shape of the volume-weighted distribution. The x^{th} volume percentile diameter d_x is given by:

$$F_3(d_x) = \frac{x}{100} = \int_{-\infty}^{d_x} f_3(D)\, dD, \quad \text{where } 0 \leq x \leq 100. \tag{2.14}$$

In this work, lower-case notation is used for the volume percentile diameter in Eq. (2.14) to differentiate it from other types of mean diameters.

2.2.4 Generalized Distribution Moments and Mean Particle Diameters

Using Eq. (2.10), the k^{th} raw moment of an r-weighted size distribution $M_{k,r}$ is given by:

$$M_{k,r} = \int_{-\infty}^{\infty} D^k f_r(D) dD = \frac{\int_{-\infty}^{\infty} D^{k+r} f_0(D) dD}{\int_{-\infty}^{\infty} D^r f_0(D) dD} = \frac{M_{k+r,0}}{M_{r,0}}. \tag{2.15}$$

The generalized mean particle diameter $D_{k,r}$ is then extracted from the weighted distribution moment with:

$$D_{k,r} = \sqrt[k]{M_{k,r}}. \tag{2.16}$$

This representation of mean particle diameters has been referred to as the "German (DIN) System" [40]. From Eq. (2.15), it can be seen that a generalized distribution moment can also be expressed as a ratio of moments, each including the original number PDF. In the alternative Moment-Ratio (M-R) system, which has been extensively developed by Alderliesten [41], generalized mean particle diameters are estimated with:

$$D(p,q) = \left[\frac{\sum_i n_i D_i^p}{\sum_i n_i D_i^q}\right]^{\frac{1}{(p-q)}}, \quad \text{if } p \neq q. \tag{2.17}$$

$$D(q,q) = \exp\left[\frac{\sum_i n_i D_i^q \ln D_i}{\sum_i n_i D_i^q}\right], \quad \text{if } p = q. \tag{2.18}$$

It is important to note that the DIN system and the M-R system are related by $p = k + r$ and $q = r$. One example of a mean diameter than can be defined with the M-R system is the SMD, which appears in Eq. (2.1). Using Eq. (2.17) with $p = 3$ and $q = 2$, the SMD is given by:

$$D(3,2) = \frac{\sum_i n_i D_i^3}{\sum_i n_i D_i^2}. \tag{2.19}$$

The arithmetic mean diameter defined in Eq. (2.6) can also be defined with the M-R system using Eq. (2.17) with $p = 1$ and $q = 0$, yielding $\bar{D} = D(1,0)$. The M-R system provides a consistent nomenclature framework to convey the physical meaning behind the different types of mean diameters. For example, the SMD in Eq. (2.19) can be re-expressed as:

$$D(3,2) = \sum_i \frac{n_i D_i^2}{\sum_j n_j D_j^2} D_i. \tag{2.20}$$

From Eq. (2.20), it can be seen that the averaged variable is the particle diameter D with a relative-surface weighting factor. Thus, the SMD is designated the surface-weighted mean diameter. Finally, the mean particle diameters obtained with the M-R system can be correlated with other measurable sample properties. As such, the mean diameter most relevant to a given physical or chemical process can be empirically determined.

2.3 Introduction to Digital In-Line Holography

Digital in-line holography (DIH) is a laser-based measurement technique that is frequently used to visualize and quantify 3D flow structures and particle dynamics [42]. The process of using holography, or wavefront reconstruction, for 3D imaging was first demonstrated by Gabor [43], who also coined the term hologram. A hologram is a record of the interference between an object wavefront (light scattered from the object of interest) and a second known wavefront (reference beam). When the known reference beam subsequently illuminates the hologram, the light is diffracted to reproduce the object wavefront. Thus, the reference beam and the hologram allow for the object of interest to be viewed even if it is no longer physically present. Despite holography being first demonstrated in 1948, major advancements would not occur until the subsequent development of the laser in the early 1960s [42]. Along with suitable laser technology, the invention of DIH would also require the development of digital cameras.

With the DIH technique, the aforementioned two-step process: (1) hologram recording and (2) wavefront reconstruction, is completed with a coherent light source (laser) and a digital image sensor (camera) that are aligned along a single optical axis. In this variation of holography, a single laser is used to create the hologram, with the undisturbed portion of the laser beam also acting as the reference beam. In the first step, the hologram is recorded using a digital image sensor, with the diffraction pattern encoded as intensity variations across the sensor's pixels. In the second step, the object wavefront is reconstructed at different locations along the optical axis using the equations describing the wave propagation of light. This reconstruction step is useful for visualizing and "traversing" the 3D region of interest. Additional numerical post-processing algorithms can then be subsequently implemented to detect objects at their correct 3D position and track them across multiple images. The reconstruction step can also be applied to simulate or predict the holograms that would be produced from different types of objects.

DIH has been successfully employed in laboratory and field applications to detect, size, and track objects in a wide variety of flows [44–49]. The single-axis DIH configuration enables the investigation of particle dynamics with a relatively simple experimental setup. With respect to digital image sensors, charge-coupled-device (CCD) cameras are frequently implemented due to their high spatial resolution and low noise characteristics. The high-speed imaging capabilities of modern complementary metal-oxide-semiconductor (CMOS) cameras can also be leveraged for time-resolved investigations [50, 51].

2.3.1 Digital Reconstruction of Holograms

During the digital reconstruction process, the optical field is determined by calculating the diffraction from a 2D complex aperture which approximates the hologram [42]. The optical field is given by:

$$\tilde{U}_R = \iint_{x,y} \tilde{U}_R(\xi, \eta, z = 0) \left[-\frac{\partial G}{\partial n}(x - \xi, y - \eta, z) \right] d\xi d\eta. \tag{2.21}$$

Here $\tilde{U}_R$ is the reconstructed optical field, $\tilde{U}_R(\xi, \eta, z = 0)$ is the optical field encoded in the hologram, and $\frac{\partial G}{\partial n}$ is the normal derivative of Green's function evaluated at the aperture plane. Two kernel or Green's functions are frequently used, depending on the boundary conditions imposed to solve the diffraction problem. The first function is the Rayleigh-Sommerfeld formula:

$$-\frac{\partial G}{\partial n}(x, y; z) = \frac{1}{\lambda} \frac{\exp(-jk\sqrt{x^2 + y^2 + z^2})}{\sqrt{x^2 + y^2 + z^2}} \cos\theta. \tag{2.22}$$

In this expression, the quantity $\cos\theta = z/\sqrt{x^2 + y^2 + z^2}$ is often assumed to be approximately unity for simplicity. The second function is the Kirchoff-Fresnel formula:

$$-\frac{\partial G}{\partial n}(x, y; z) = \frac{\exp(jkz)}{j\lambda z} \exp\left\{ j\frac{k}{2z}\left(x^2 + y^2\right) \right\}. \tag{2.23}$$

The expression in Eq. 2.21 can be evaluated through a multiplication in the frequency domain with $\tilde{U}_R(x, y, z) = \mathcal{F}^{-1}\left\{\mathcal{F}\{\tilde{U}_R\} \cdot \tilde{G}\right\}$, whereby $\tilde{G} = \mathcal{F}\left\{\frac{\partial G}{\partial n}\right\}$. Practical methods have been developed for the simulation and reconstruction of in-line holograms using the Fast Fourier Transform (FFT) algorithm [52]. Sophisticated holography data processors have also been developed to automatically extract 3D particle property measurements from experimental holograms [53].

2.4 Introduction to Particle Image Velocimetry

Particle Image Velocimetry (PIV) refers to a class of methods used in experimental fluid mechanics for qualitative flow field visualization and quantitative flow field measurement [54]. In PIV, instantaneous velocities are obtained by measuring the displacement of marked regions of the flow at two or more times. First, the flow is seeded by mircrometric particles that accurately follow the motion of the surrounding fluid. Next, a subset of particles in the flow are illuminated by at least two pulsed laser sheets. Finally, the scattered light from the particles is imaged with a camera. The particle displacements and the known time increment between the illuminating laser pulses combine, in the fundamental definition of velocity, to yield an estimate of the fluid velocity in the 2D plane of interest. In the simplest implementation of PIV, a single double-pulse laser and camera are used to measure two velocity components in a plane (2D2C). Additional cameras and an expanded laser sheet can also be used to measure all three velocity components in a three-dimensional space (3D3C). Since the development of PIV, it has largely superseded other point-wise velocity measurement techniques such as hot-wire anemometry (HWA) and laser-Doppler velocimetry (LDV), although these techniques are still well-suited to particular types of flow situations. Nevertheless, PIV has led to major advancements in experimental fluid mechanics from studies over a wide range of geometries, flow conditions, and spatial scales [55].

2.4.1 Determination of Particle Displacements

All PIV methods inherently measure the velocities of particles as determined by their displacements over a known time period. In PIV, statistical methods are employed to track the displacement of small groups of particles rather than individual particles. This is most commonly achieved by cross-correlating the images of particles within small interrogation windows, which are subregions of the larger field of view [54]. The cross-correlation for a given interrogation window W is given by:

$$R(\vec{s}) = \int_W I_1(\boldsymbol{X}) I_2(\boldsymbol{X} + \vec{s}) d\boldsymbol{X}. \tag{2.24}$$

Here $R(\vec{s})$ is the correlation estimator, $I_1(\boldsymbol{X})$ is the first image, and $I_2(\boldsymbol{X} + \vec{s})$ is the second image shifted with respect to the first by the displacement $\vec{s}$. The cross-correlation is a measure of similarity between the two images, and thus will have large values when the particle images overlap. Thus, the maximum of $R(\vec{s})$ determines the most-likely displacement of the particles. Since many particles reside in each image, false correlation peaks will also be measured when different particles coincidentally overlap at different displacements. Thus, a sufficient number of particles must be enclosed by the interrogation window to ensure that the particle displacement peak in the $\vec{s}$-plane will be much larger than any of the false peaks. Furthermore, since the cross-correlation method relies on the same group of particles being in both images, care must be taken to consider the loss of particles by out-of-plane motion away from the light sheet.

2.5 Introduction to Chemiluminescence Imaging

Chemiluminescence imaging is one of the most widely used optical diagnostic techniques for combustion [56]. Chemiluminescence in flames refers to the emission of light from chemically-excited species as they return to their electronic ground state [57]. In this technique, chemiluminescence emissions are imaged with a camera to reveal the spatial features of the flame front, the primary combustion reaction zone, and the areas of high local heat release. Chemiluminescence imaging is attractive for combustion diagnostics since it is simple relative to more sophisticated laser diagnostic techniques, and only requires optical access to the flame and a suitable imaging system [58] . An appropriate filter must also be used to selectively collect the emissions from the excited-state species. The most-commonly imaged intermediate species are the excited-state hydroxyl (OH*) and excited-state methylidyne (CH*) molecules, which have peak emissions near 308 nm and 431 nm, respectively. In certain hydrocarbon-air flames, well-calibrated OH* and CH* measurements can be coupled for additional equivalence ratio sensing capabilities [59].

The chemiluminescence process involves increasing the total energy of a molecule by means of chemical reactions. Excited-state species can be formed through collisions and destroyed via spontaneous emission and collisional quenching. Thus the chemiluminescence process can be illustrated with the following reactions:

$$A + B \rightarrow C^* + \text{(other species)} \tag{2.25a}$$

$$C^* \rightarrow C + h\nu \tag{2.25b}$$

$$C^* + M \rightarrow C + M \tag{2.25c}$$

Here A, B, and C are ground-state species, C^* is an excited-state species, M is a third-body species, and $h\nu$ is an emitted photon. From these reactions it can be seen that not all excited-state species contribute to the generation of chemiluminescence emissions, as some simply collide with other species to return to the ground state.

2.6 Introduction to Planar Laser-Induced Fluorescence

Laser induced-fluorescence (LIF) is a diagnostic technique that has found widespread application in the combustion sciences for the sensitive detection of reactive chemical intermediates in flames [60]. Fluorescence refers to the spontaneous emission of light from an atom or molecule that has been excited to a higher energy level via the absorption of radiation. In LIF, this excitation is achieved through the use of a laser that is tuned to a specific electronic absorption transition. In planar laser-induced fluorescence (PLIF) imaging, the exciting laser is formed into a sheet to excite a planar section of the region of interest, and the resulting emission is imaged with a camera. Thus, PLIF imaging enables in-situ, non-intrusive, and 2D visualization and measurement of the species concentrations in flames [61].

2.7 Single-Photon LIF

The basic physics leveraged for single-photon LIF will be presented by considering a simple two energy level model [62], which is depicted in Fig. 2.4. This two-level system is appropriate for atomic species and certain molecular systems in equilibrium, although more complex models are used in practice for quantitative data reduction [62]. In Fig. 2.4, b_{12} and b_{21} are the rate constants for absorption and stimulated emission, respectively. These rate constants are related to the Einstein B coefficient with:

$$b = \frac{BI_\nu}{c} \tag{2.26}$$

Here, I_ν is the spectral irradiance and c is the speed of light. Furthermore, A_{21} is the rate constant for spontaneous emission given by the Einstein A coefficient, P is the rate constant for predissociation, W_{2i} is the rate constant for photoionization, and Q_{21} is the rate constant for collisional quenching. Thus the rate constants illustrated in Fig. 2.4 represent the various processes by which the species of interest can move between the two energy levels of interest. Rate equations

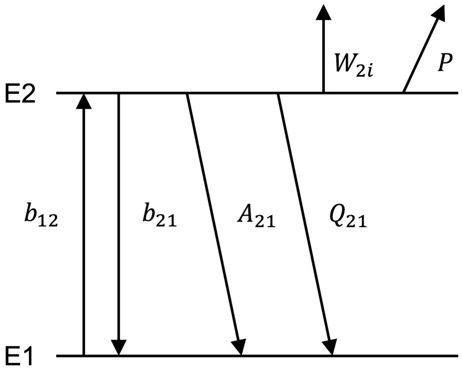

Figure 2.4: Two-level energy model for LIF modeling. Adapted from [62].

for the time derivatives of the population densities at the given state N_i are then given with:

$$\frac{dN_1}{dt} = -N_1 b_{12} + N_2(b_{21} + A_{21} + Q_{21}) \tag{2.27}$$

$$\frac{dN_2}{dt} = N_1 b_{12} - N_2(b_{21} + A_{21} + Q_{21} + P + W_{2i}) \tag{2.28}$$

Assuming a closed system and negligible predissociation and photoionization, adding Eqs. 2.27 and 2.28 yields:

$$\frac{dN_2}{dt} + \frac{dN_2}{dt} = \frac{d}{dt}(N_1 + N_2) = 0 \tag{2.29}$$

$$N_1 + N_2 = constant = N_1^0 \tag{2.30}$$

Here, the population density of the two energy levels is equal to N_1^0, which is the population density in the ground state prior to laser excitation. This also assumes that the initial excited-state population is negligible. At low laser excitation irradiances, the fluorescence signal power F is given by:

$$F = \frac{h\nu}{c}\frac{\Omega}{4\pi} l A N_1^0 B_{12} I_\nu \frac{A_{21}}{A_{21} + Q_{21}} \tag{2.31}$$

Here, h is Planck's constant, Ω is the solid angle of collection, l is the axial extent along the beam from which the fluorescence is observed, and A is the focal area of the laser beam. With this expression, the fluorescence is said to be in the linear regime, since it is linearly proportional to the input laser irradiance.

3. DIGITAL IN-LINE HOLOGRAPHY FOR DUST CLOUD PARTICLE DIAGNOSTICS*

3.1 DIH Introduction

Evaluation of hazards presented by combustible dust is critical to risk assessment and mitigation in the industries that are susceptible to accidental dust explosions. Standard methods [11, 63–66] have been developed and adopted to assess the two major components of the associated risk, namely explosion probability, and severity. The minimum ignition energy (MIE)—the lowest energy required to ignite a combustible mixture with a capacitive spark discharge—is one of many key parameters that relates the explosive characteristics of various dust clouds. Although the MIE has been indispensable as a standard indicator of relative ignition sensitivity, it was recognized relatively early on that dust clouds are not characterized by the MIE as simply as combustible gas mixtures [20, 21]. Early studies have demonstrated that dust ignitability is strongly influenced by the spark circuit's series resistance [20], and that sufficiently short sparks can potentially inhibit ignition by removing combustible material from the ignition zone [21]. A recent study by Eckhoff [67] has even produced a mathematical model that reasonably fits available dust explosion data, indicating an improved understanding of how a testing device's features might affect MIE measurements. Conversely, many studies have demonstrated that dust characteristics like particle size [23, 24], polydispersity [25], and morphology [26, 27] can influence the measurement of the MIE as well. The atmosphere used in testing [33, 34] has also been shown to be an MIE influencing parameter. Hence, it is clear that many complex factors must be considered to build a complete understanding of dust cloud ignitability in standard testing configurations.

Given the comprehensive review of the dust explosion research field given by Eckhoff [68], it is apparent that increasingly sophisticated and flexible methods will be developed to meet the evolving dust explosion prevention and mitigation needs of vulnerable industries. The utilization of advanced optical diagnostic techniques to characterize dust clouds in MIE devices has been

---

*Reprinted with permission from "High-speed digital in-line holography for in-situ dust cloud characterization in a minimum ignition energy device" by C. Schweizer, S. Prasad, A. Saini, C. V. Mashuga, and W. D. Kulatilaka, 2020. *Powder Technology*, vol. 376, pp. 612-621, Copyright [2020] by Elsevier B.V.

identified as a research thrust that is well-aligned with the trends reported above. Research in this area will investigate fundamental aspects of dust cloud ignitability within the practical context of internationally recognized standards, equipment, and explosion parameters. High-speed digital in-line holography (DIH) [69], a laser-based volumetric imaging technique, provides a wide range of desirable particle diagnostic capabilities to conduct studies of this nature. DIH uses a single coherent light source to create interference patterns that are recorded using a digital image sensor [42]. The resulting interference pattern images, or holograms, are then numerically refocused through a specified depth during post-processing to reveal objects, such as dust particles, inside the volume of interest. DIH has been successfully employed in laboratory and field applications to detect, size, and track objects in a wide variety of flows [44–49]. While charge-coupled-device (CCD) cameras are often utilized in holography experiments due to their high spatial resolution and low noise characteristics, the increased availability and performance of high-quality complementary metal-oxide-semiconductor (CMOS) cameras has enabled investigation of transient particle dynamics through high-speed imaging [50, 51]. Thus, DIH systems incorporating modern CMOS cameras can combine a relatively simple and flexible diagnostic scheme with high-frequency, time-resolved measurements.

In the present study, high-speed DIH is utilized to image and characterize dust particles inside a Kühner MIKE3 MIE device at 20 kHz (20,000 images/second). Minor modifications to the Kühner MIKE3 Hartmann dispersion tube are necessary to satisfy the optical requirements of the high-speed DIH system. However, the electrodes and tube are maintained in their standard configurations. Without disturbing the flow, the experimental system is able to extract information from small amounts of material in the ignition zone with precise timing. This experiment demonstrates new capability and flexibility over previous experimental and computational attempts to characterize dispersed clouds of dust [70, 71]. This research also represents an extension of recent applications of holographic methods for dust research. These efforts have focused primarily on coal powder characterization using CCD cameras at relatively low image acquisition rates [72–75].

For this experiment, two different dust samples are selected to establish baseline capability for the high-speed DIH system and identify areas for further development. A Borosilicate glass bead sample, which has a relatively large and broad size distribution, is used to identify a provisional upper bound on mass loadings that are compatible with the high-speed DIH system. A soda-lime glass microsphere sample is used to demonstrate characterization capability for smaller and narrower size distributions and establish a tentative lower size detection limit. Sizing measurements, collected from 5 ms of hologram video, are compared with the results from a dedicated particle sizer. The transient behaviors of both dust clouds are also examined to demonstrate how dispersion conditions in the ignition zone can be measured and compared. The experimental apparatus, sample preparation, and data analysis are described in detail in Section 3.2. The experimental results obtained from this experiment are reported and discussed in Section 3.3. Finally, the major conclusions of this work and areas for future study are summarized in Section 3.4.

3.2 DIH Experimental

The experimental apparatus used to produce high-speed hologram sequences of dust dispersions is shown schematically in Fig. 3.1. The experimental apparatus comprises a high-speed DIH system synchronized with a modified MIE device. Dust particle illumination is produced by a single-longitudinal-mode, diode-pumped solid-state laser (Oxxius, 250 mW, 532 nm, continuous-wave). The output beam from the laser head is expanded and collimated to form a 50 mm diameter beam using a combination of negative and positive lenses, as shown. Additionally, a neutral density filter is placed in the beam path to attenuate the laser energy to prevent camera saturation.

The output beam from the laser system is then passed through a modified MIE device (Kühner MIKE3). For this study, the 1.2 L glass tube that is utilized for standard MIE tests is replaced by a customized polycarbonate tube of identical dimensions. The polycarbonate tube has been fitted with two high-quality optical windows that provide unobstructed optical access to the dust cloud region of interest around the electrodes. The two ignition electrodes are placed into the tube perpendicular to the laser axis. The electrode gap is maintained at 6 mm, and the electrode height is 100 mm from the bottom of the dispersion cup. Although spark generation is possible with

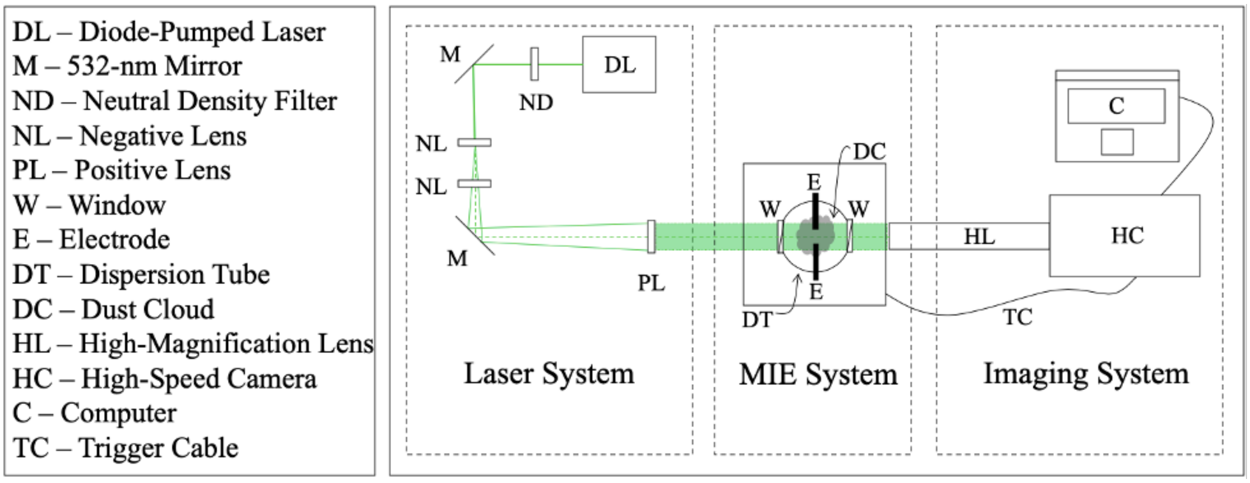

Figure 3.1: Schematic of the experimental apparatus configured for high-speed DIH of dust dispersions. Reprinted from [79].

the modified tube, no sparks were initiated for the dispersion studies in this experiment, since the primary objective here is to characterize the dust cloud prior to ignition. Dust is then dispersed upwards through the tube by a pulse of compressed air (7 bar) from a mushroom-shaped nozzle. A lid assembly with a stainless-steel flapper prevents the resulting dust cloud from escaping into the environment.

The collimated laser beam passes through the dust cloud in the dispersion tube and generates diffraction patterns from the edges of the particles. The resulting in-line holograms are recorded at 20 kHz with a high-speed CMOS camera (Photron FASTCAM SA-Z, monochrome, 1024 × 1024 pixels). A long-distance microscope lens (Infinity K2 DistaMax with CF-4 objective) is fitted in front of the camera to achieve magnification levels that are appropriate for each dust sample. The magnification level of the imaging system is quantified using a calibration image of a 1951 USAF resolution test chart. The chart, which contains line patterns with precise spatial frequencies, is maneuvered until an in-focus image is captured. A magnification factor of approximately 225 pixel/mm (i.e., $\sim$4.4 µm/pixel) is used for imaging the larger borosilicate glass particles. For the smaller soda-lime glass particles, a magnification factor of 283 pixel/mm (i.e., $\sim$3.5 µm/pixel) is used. For all imaging configurations, the front focal plane of the imaging system is located at the center of the dispersion tube. Thus, the size of the square image window at the front focal plane is approximately 4.55 mm × 4.55 mm for the borosilicate glass dispersions, and 3.62 mm × 3.62 mm for the soda-lime glass dispersions. The size, orientation, and in-plane coordinate axes of the image window with respect to the electrodes for each configuration are illustrated in Fig. 3.2.

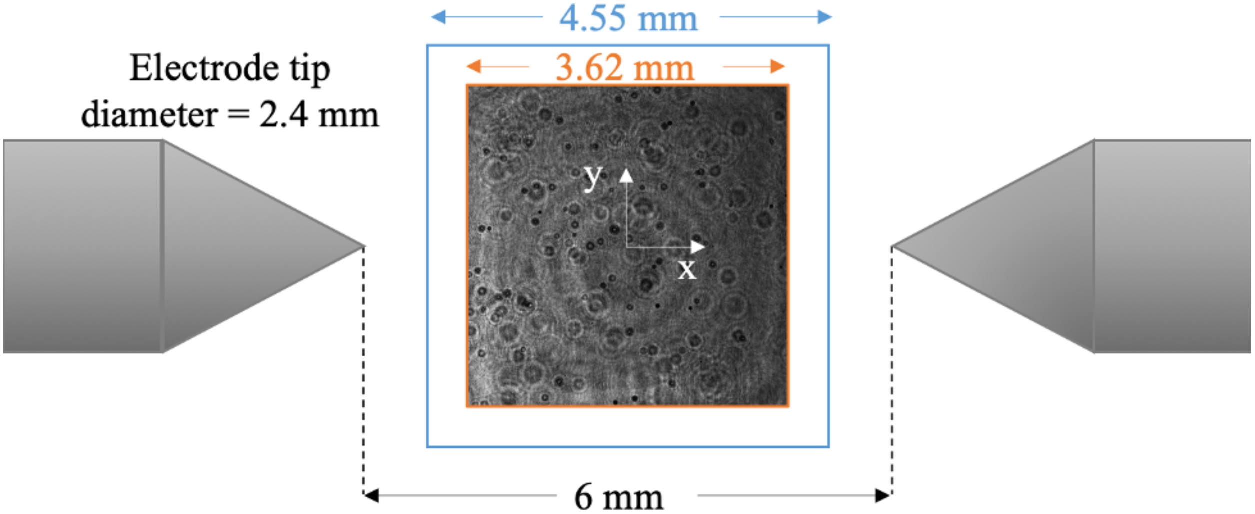

Figure 3.2: Square image window size, orientation, and in-plane coordinate axes for the borosilicate glass dispersions (blue), and the soda-lime glass dispersions (orange). Reprinted from [79].

To synchronize the high-speed DIH system to the MIE device, a 5-volt TTL trigger signal from the MIE device solenoid valve, which controls the air pulse to the mushroom-shaped nozzle, is sent to the camera to start each experimental recording. The experimental system's timing precision, in a statistical sense, is characterized by a separate high-speed video analysis. For this analysis a total of 32 videos were recorded, without laser illumination or dust present in the tube, to capture images of ignition sparks initiated with a delay set at 120 ms between the dispersion initiation and the spark formation. The corresponding actual delay time is obtained by finding the camera frame with the spark in the 20-kHz video recording. The mean spark time obtained by this method is 119.437 ± 0.021 ms, based on a 95% confidence interval. The interval width of 42 µs is smaller than the 50 µs duration between successive images at 20 kHz. Thus, the temporal location of the mean spark time for all dispersions generated with the synchronized experimental system can be associated with a single camera frame.

A photograph of the experimental apparatus is shown in Fig. 3.3. The high-speed DIH system is mounted to a 300×450-mm optical breadboard with height-adjustable supports, allowing precise position control. Additionally, a smaller optical breadboard plate is utilized inside the MIE device to ensure precise and repeatable alignment of the dispersion tube. The corresponding three-dimensional coordinate axes for this experiment with respect to the laser beam and electrodes are also shown in Fig. 3.3.

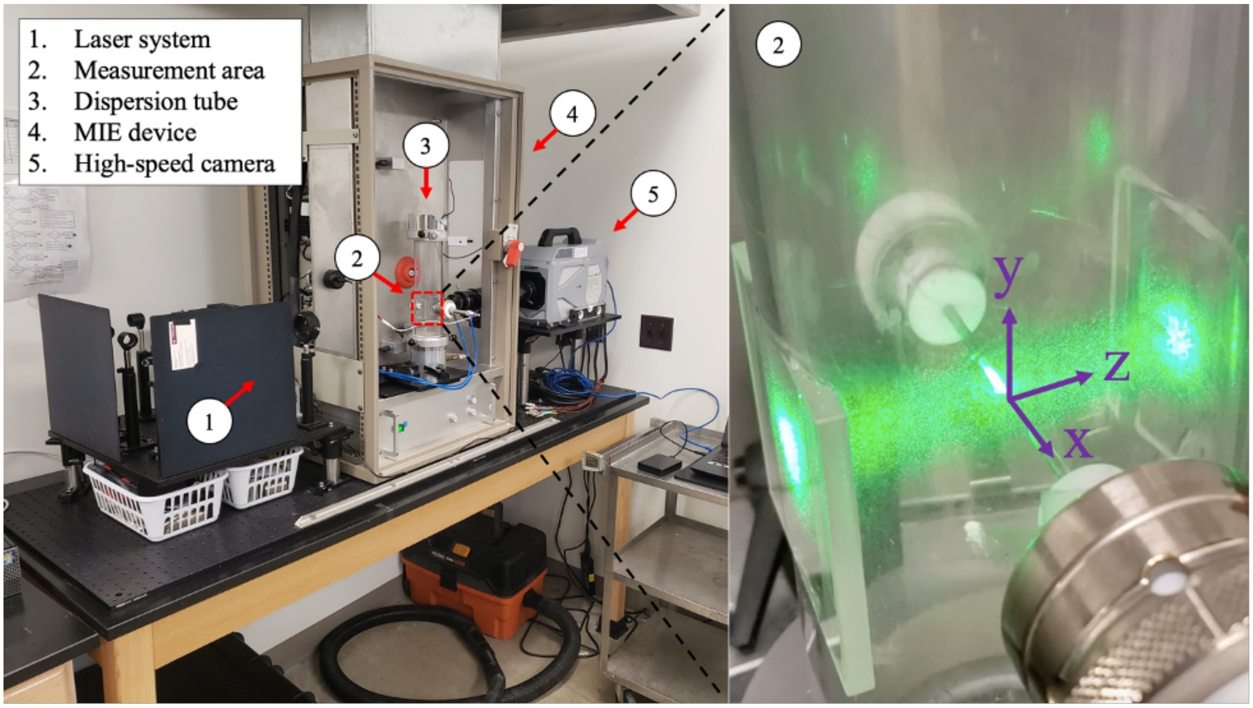

Figure 3.3: Photograph of the experimental apparatus configured for high-speed DIH of dust dispersions. The full three-dimensional coordinate axes for this experiment are also shown with respect to the laser beam and electrodes. Reprinted from [79].

After the experiments, the holograms are transferred to an off-site workstation for processing. Although more than 1 second of video is collected for each dust dispersion, only selected images corresponding to a 5 ms window, from 117–122 ms, around the mean spark time are processed. An example of an unprocessed hologram acquired from the imaging configuration with 225 pixels/mm magnification is shown in Fig. 3.4 (a). The zoomed-in view in Fig. 3.4 (b) shows a mix of in-focus particles with sharp edges and out-of-focus particles with ring-shaped fringes. In-focus particles in the hologram are located near the front focal plane of the imaging system, while the out-of-focus particles are farther away from the front focal plane. Thus, the experimental holograms produced by the high-speed DIH system encode depth information (z-direction) in addition to the x-y location of the particles in the volume of interest.

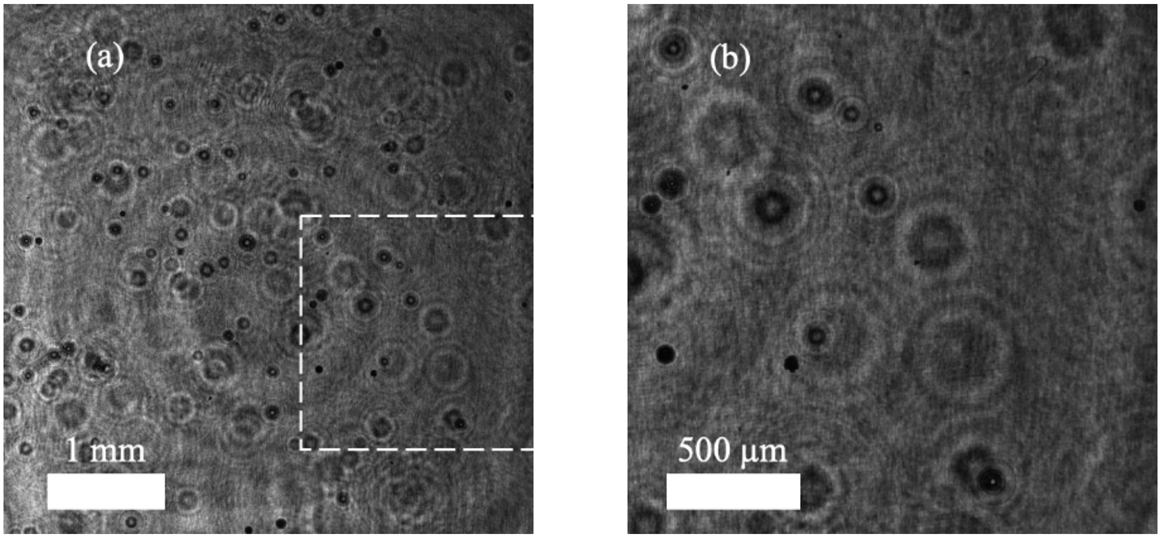

Figure 3.4: (a) Unprocessed hologram, and (b) zoomed-in region showing particles in and out of focus. Reprinted from [79].

3.2.1 *Dust Samples*

For the present study, borosilicate glass (Sigma-Aldrich, spherical) and soda-lime glass (Cospheric LLC, 2.5 g/cm^3, > 99.9% by wt., spherical) are prepared to permit several layers of particle characterization capability testing. To establish a sizing benchmark, a reference size distribution is measured for each sample using a laser diffraction particle size analyzer (Beckman Coulter LS 13 320). These reference size distributions are plotted in Fig. 3.5, and their associated representative statistics are reported in Table 3.1. The included quantities are the Sauter mean diameter D(3,2), the tenth percentile diameter d_{10}, the median diameter d_{50}, the ninetieth percentile diameter d_{90}, and the polydispersity σ_D, defined in Eq. 3.1 as:

$$\sigma_D = \frac{d_{90} - d_{10}}{d_{50}} \tag{3.1}$$

From Fig. 3.5 it is evident that the borosilicate glass size distribution is more than 2× broader

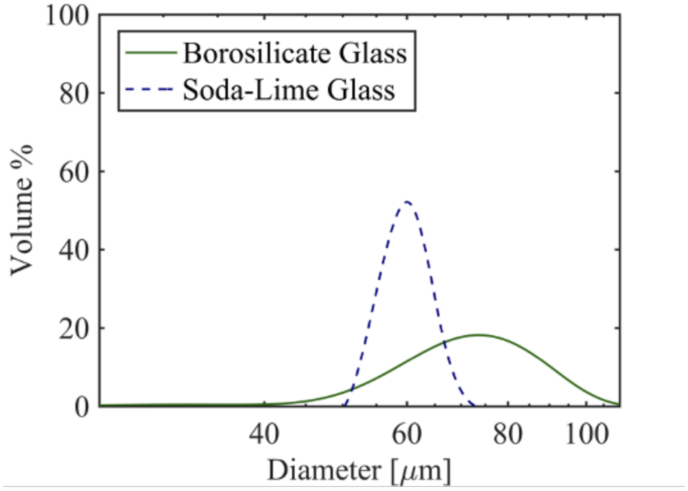

Figure 3.5: Reference particle size distributions for the borosilicate glass and soda-lime glass samples measured by the Beckman Coulter LS 13 320. Reprinted from [79].

than the soda-lime glass size distribution. Additionally, the borosilicate glass distribution is centered around 73 µm whereas the soda-lime glass distribution is centered around 60 µm. These visual observations are confirmed by the representative diameter and polydispersity values reported in Table 3.1. These reference size distributions and their corresponding representative statistics demonstrate that the samples selected for this experiment allow for the characterization of spherical morphologies over a wide range of size conditions.

It is determined from several preliminary hologram videos that for a given mass loaded into the MIE dispersion tube, borosilicate glass dispersions have fewer particles present in the volume of interest to obstruct the high-speed DIH system's line-of-sight. Thus, a relatively larger sample can be used to characterize the borosilicate glass dispersions while still maintaining sufficient hologram quality for individual particle detection and analysis. The borosilicate glass sample is therefore used to determine a provisional maximum dispersion mass loading that is compatible with the high-speed DIH system. Although the soda-lime glass sample enables the characterization of a more MIE testing suitable dust size, the larger associated particle number density severely constrains the mass loadings that are compatible with the high-speed DIH experimental system. Hence, for the borosilicate glass, measurements are performed from mass loadings of 150 mg,

Table 3.1: Particle size distribution statistics measured with the Beckman Coulter LS 13 320. Reprinted from [79].

	D(3,2) [µm]	d_{10} [µm]	d_{50} [µm]	d_{90} [µm]	Polydispersity σ_D
Borosilicate Glass	50.1	46.8	64.5	81.9	0.54
Soda-Lime Glass	59.7	54.3	59.9	66.1	0.20

while mass loadings of 15 mg are used for the soda-lime glass. Thus, this experiment establishes particle detection and tracking capability for laboratory or small-scale dispersion scenarios.

Each sample is dried in a nitrogen-purged oven before characterization to eliminate moisture-induced agglomeration during dispersion. Also, due to the stochastic nature of the clouds created by the MIE device, the experiments are repeated 2–3 times to develop a statistically averaged characterization. After each dispersion, the entire loading is removed and replaced to reduce the probability and influence of particle breakage and electrostatic wall attrition, which can affect the size distribution of particles from one dispersion to the next [23].

3.2.2 Data Analysis

Data analysis is conducted on a separate workstation with DIH processing codes [53] that sequentially process each image comprising the high-speed hologram video. In this processing code, particles are detected, sized, and tracked using the methods developed by Guildenbecher et al. [76] and Gao et al. [77], whereby experimental holograms are numerically refocused through a user-specified depth along the laser axis (z-direction). This process is represented mathematically by the solution of the diffraction integral equation, from Guildenbecher et al. [76], given by Eq. 3.2:

$$E(x, y; z) = [I_0(x, y)E_r^*(x, y)] \otimes g(x, y; z) \tag{3.2}$$

Here $E(x, y; z)$ is the reconstructed complex amplitude at the specified axial depth z, $I_0(x, y)$ is the intensity of the experimental hologram produced by the high-speed DIH system, $E_r^*(x, y)$ is the conjugate reference wave, $\otimes$ is the convolution operator, and $g(x, y; z)$ is the Rayleigh-

Sommerfeld diffraction kernel. $E(x, y; z)$ in Eq. 3.2 is computed in the frequency domain using a fast Fourier transform (FFT) algorithm and Eq. 3.3, given by:

$$E(x, y; z) = \mathcal{F}^{-1}\left\{\mathcal{F}\{I_0(x, y)\} \cdot \exp\left(\frac{2\pi i z}{\lambda}\sqrt{1 - \lambda^2 f_x^2 - \lambda^2 f_y^2}\right)\right\} \tag{3.3}$$

Here, $\mathcal{F}$ denotes the Fourier transform, λ is the illumination wavelength, and f_x and f_y are the transverse spatial frequencies. Finally, the intensity of the reconstructed field calculated with $I = |E|^2$.

A particle detection algorithm then assesses the features in the reconstructed or refocused planes. For this study, a hybrid method including minimum intensity and maximum edge sharpness focus criteria is utilized to determine the three-dimensional spatial locations and sizes of particles in the interrogation volume. The rationale behind utilizing these focus metrics is that minimum intensity information can be used to accurately capture particle morphology and in-plane position, while maximum edge sharpness information can be used to accurately capture particle depth. In simplified terms, particles that are in-focus are usually observed as dark shapes with sharp edges against a bright background. By assessing these focus criteria at different reconstructed depths, the hybrid particle detection algorithm can accurately determine a particle's size and location in the interrogation volume.

Detailed descriptions of the hybrid particle detection algorithm are provided by Guildenbecher et al. [76] and Gao et al. [77], and a brief summary of the method is provided here. To initiate the particle detection procedure with a given experimental hologram, the reconstructed field intensity is calculated at various depths throughout the volume of interest. A minimum intensity map is then created by collecting the lowest intensity value for each pixel in the image array across all reconstructed depths. This map reveals dark particle features in the interrogation volume and projects them onto a single plane for further analysis. A global binary threshold is then applied to the minimum intensity map to roughly segment the entire particle field from the background. The particle edges created by this binarization are then assessed for sharpness via the Tenengrad operator. The global threshold is subsequently modified until the sharpness of the created edges is maximized. Once a global threshold has been selected to optimize the contrast between the entire particle field and the background, the thresholding and sharpness assessment procedure is repeated for each individual particle to refine the local contrast. Once optimal local thresholds are selected for each particle, an initial depth estimate is made by averaging the depth values along each particle's edge. In the hybrid detection algorithm's final step, the initial depth estimates extracted from the minimum intensity map are used to detect individual particles directly via reconstruction of the original experimental hologram. Compared to the minimum intensity map, the reconstructed intensity better represents particle size and shape. The thresholding and sharpness assessment procedure is repeated in the reconstructed image to extract fully refined particle sizes, in-plane positions, and depths from each particle. The overall hybrid detection algorithm is then applied to the next experimental hologram in the video sequence.

After the particles are detected, located, and sized, another algorithm links these objects in subsequent images to reveal distinct particle trajectories. Each particle's velocity in the three-dimensional domain can therefore be calculated as well. It is important to note that because the observed flow phenomena are slow relative to the imaging rate, a given set of particles can remain in the field of view for many frames. Therefore, ensuring that unique particles are accurately identified from frame to frame is crucial for minimizing multiple-counting bias. The regression-based multiframe tracking algorithm [53] implemented in this work initially links particles based on in-plane positional proximity and size similarity. These initial in-plane trajectories are extrapolated forward in time based on a regression-based quadratic model. Trajectories that sufficiently overlap get linked together. This linking process repeats until no more overlapping trajectories are found, and trajectories of insufficient length are removed. Finally, a regression-based linear model is used to fit the measured depth positions for each unique trajectory. Based on this description, it can be seen that the particle tracking algorithm also functions as a filtering process. Therefore, processing parameters must be carefully chosen to avoid the introduction of additional bias into the final result. Previous work [53] has demonstrated that the regression-based multiframe tracking algorithm is able to significantly reduce the uncertainty associated with determining the depth of a given particle. This study reported a z-coordinate uncertainty of 30% of the mean particle diameter.

Because particles can be uniquely tracked over the entire duration of the hologram video, it is possible to produce time-integrated characterizations for a given dispersion. Integrating information about the number and size of unique particles detected in the interrogation volume over 5 ms of video permits dynamically measured particle size distributions. These size distributions are presented and compared to their corresponding reference size distributions in the Results and Discussion section. For this study, an interrogation depth of 35 mm is traversed, which corresponds to the radius of the dust dispersion tube. The interrogation volume is therefore defined by the depth traversal distance multiplied by the image window area. For the borosilicate glass dispersions, reconstructions through this volume are conducted in steps of 35 μm. For the soda-lime glass samples, a smaller step size of 17.5 μm is selected.

While time-integrated characterizations are useful for accumulating information from the entire processed video, it is also of interest to characterize the instantaneous state of a transient dispersion process as well. Thus, the data processing routine is also configured to measure information from only the particles detected in a given image, and track the evolution of that information in time. The resulting transient volume, concentration, and mean in-plane velocity profiles from the borosilicate glass and soda-lime glass dispersions are also presented and compared in the following section.

3.3 DIH Results and Discussion

3.3.1 Particle Detection and Tracking

An example output image from the data analysis routine outlined above is shown in Fig. 3.6. This composite image consolidates information from many reconstructed planes. It shows all detected particles in-focus and with colored outlines corresponding to the particle size and arrows showing the in-plane velocity vectors. Such processed images are sequenced together to form an output video that shows the evolution of the particle field in the ignition zone during the time window of interest. From Fig. 3.6, it can be seen that the image processing algorithm has not

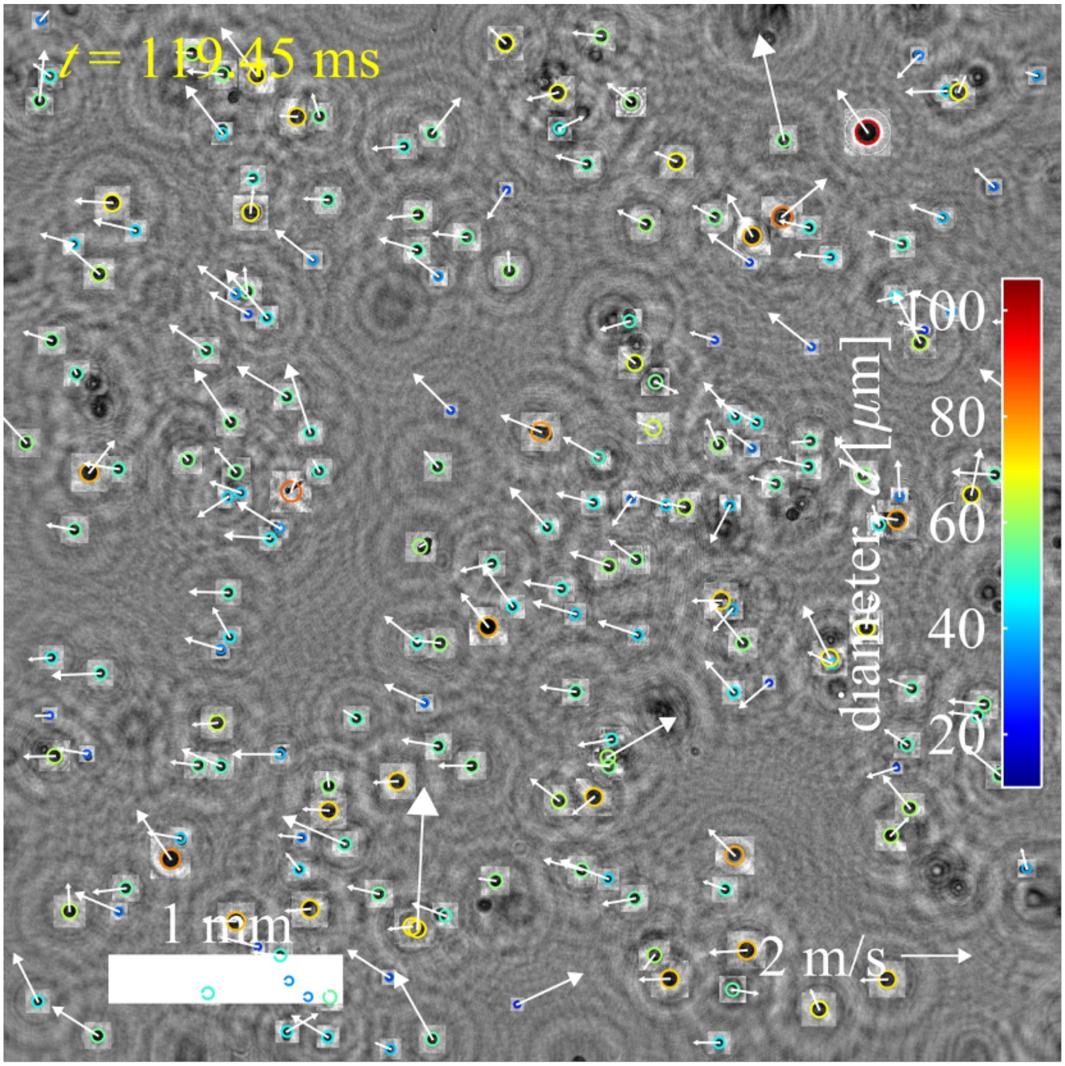

Figure 3.6: Example processed hologram from a borosilicate glass dispersion at 119.45 ms. Reprinted from [79].

successfully detected some particle-like features. The selection of appropriate detection sensitivity parameters is a crucial step in maximizing the proportion of successfully detected particles while also minimizing the number of spurious detections. While a priori knowledge of a given dust sample's size distribution can be applied to optimize particle detection, the same detection sensitivity parameters are used for both samples in this study for consistency. A detailed detection efficiency study is beyond the scope of the present work, although efforts in this area using the same hybrid detection method have been presented by Falgout et al. [78]. Falgout et al. also report a detection limit for the unmodified hybrid particle detection algorithm of 3.5× the pixel size. This value is in good agreement with the detection limit reported by the present work, namely 13 μm given a 3.5 μm pixel size.

To extend the time-resolved visualization of a given particle field into more dimensions, particle trajectories are displayed over space and time. A subset of particle trajectories from a soda-lime glass dispersion is shown in Fig. 3.7. In this figure, particle trajectories from the interrogation volume are shown statically in three spatial dimensions, with colors that indicate when a given particle is located at a specific position in space. It can be seen from this subset of trajectories that the data processing algorithm successfully detects particles throughout the entire interrogation volume, suggesting that a sizable experimental working distance is compatible with the data processing routine. Such detailed information about the spatial and temporal distribution of particles will be useful for producing and validating complex models of dust dispersion processes.

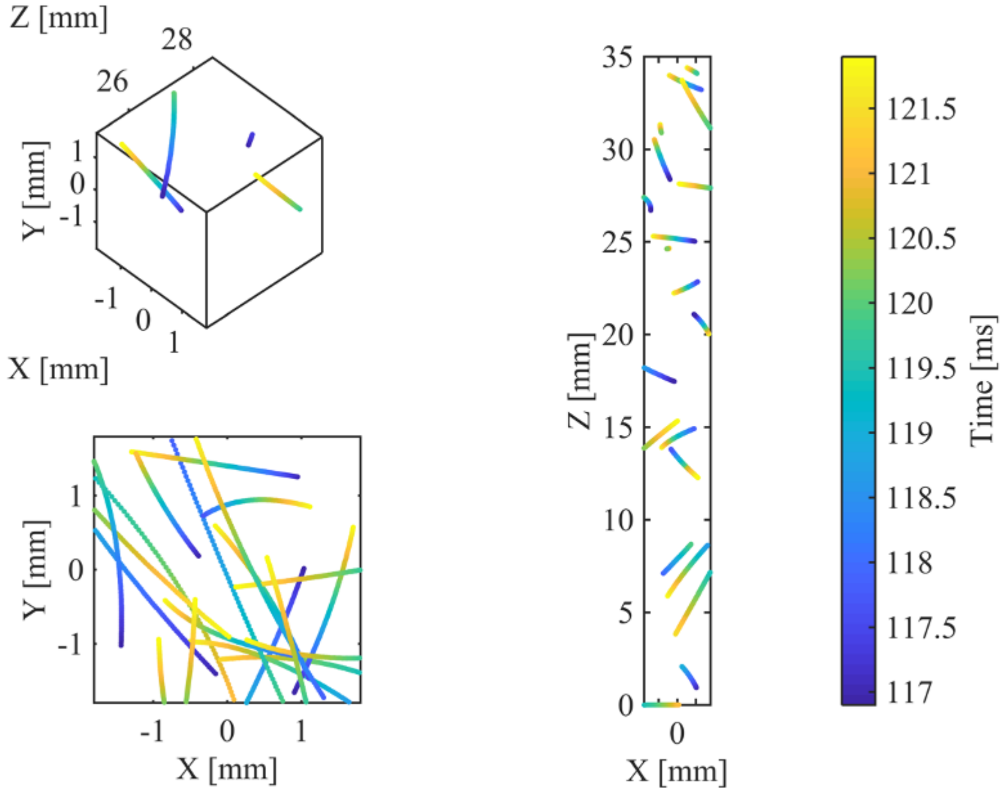

Figure 3.7: Example selection of 20 soda-lime glass particle trajectories in the domain of interest. Reprinted from [79].

Although the data presented in Figs. 3.6 & 3.7 are useful for visually assessing features of the particle field; they are less informative to discern trends that aggregate over time and across many dispersions. Here, time-integrated and transient characterizations can convey the same information in a concise and interpretable way.

3.3.2 Time-Integrated Characterization

It is seen that with a limited number of dispersions, 5 ms of video, and relatively low mass loadings, the high-speed DIH system can generate size distributions that corroborate reasonably good agreement with the reference distributions generated by the dedicated particle size analyzer. First, the DIH-derived size distributions for the borosilicate glass sample are compared with the reference distribution in Fig. 3.8. The trends from two repeated experiments match reasonably well with each other and with the reference distribution, especially at larger sizes and at the distribution tails. For both runs, more particles are detected between the 30–60 µm range than the reference distribution. However, the general upward trend in this range is well captured. There is also deviation near the mode of the reference distribution. Possible sources of these deviations are discussed further below.

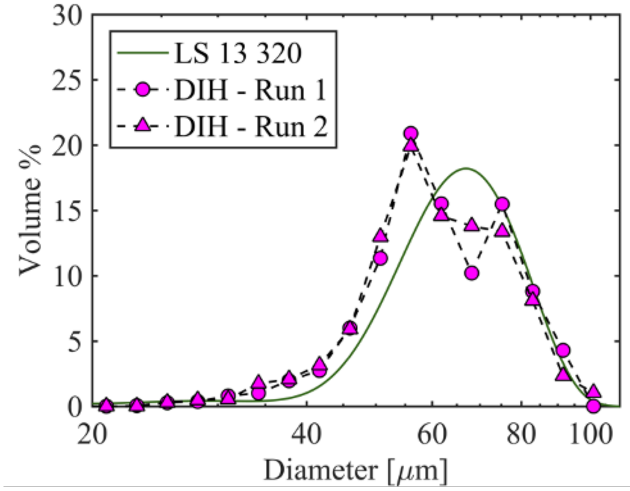

Figure 3.8: Borosilicate glass particle size distribution comparison between the Beckman Coulter LS 13 320 (solid) and high-speed DIH (dashed). Reprinted from [79].

From the three DIH-derived soda-lime glass size distributions shown in Fig. 3.9, it is seen that the second run agrees very well with the reference distribution. The other two runs appear to capture the general shape of the reference distribution but are slightly biased towards larger sizes. For both the borosilicate glass and soda-lime glass samples, it is suspected that more insight can be gained by examining the average behavior of a larger number of experimental realizations. However, the computational demands of the method limited the number of videos that could be processed during these proof-of-principle experiments. For future experiments, we plan to integrate the current data processing routine with a high-performance computing facility to investigate whether better convergence appears for a larger number of repeated dispersions.

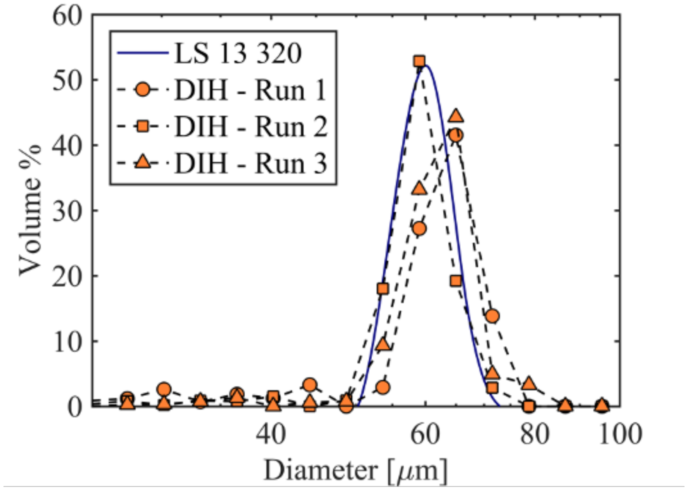

Figure 3.9: Soda-lime glass particle size distribution comparison between the Beckman Coulter LS 13 320 (solid) and high-speed DIH (dashed). Reprinted from [79].

It is also important to note that the high-speed DIH system generates a size distribution from particles at a very particular time and place. Because the dedicated sample analyzer does not generate size distributions in the same way, it is possible that the DIH-derived results will not converge to the Beckman Coulter reference distributions, and rather represent a more accurate characterization of the particles in the vicinity of the electrodes of the MIE tube. In addition to this, while the particle tracking algorithm functions to minimize multiple-counting bias as described in above, it is possible for the measured size distributions to have some level of bias. Finally, the particle size distributions generated by the high-speed DIH system are created by counting particles and then

Table 3.2: Average particle size distribution statistics measured using high-Speed DIH with average percent error as compared to the Beckman Coulter LS 13 320 statistics. Reprinted from [79].

	$\langle$D(3,2)$\rangle$ [µm]	$\langle d_{10} \rangle$ [µm]	$\langle d_{50} \rangle$ [µm]	$\langle d_{90} \rangle$ [µm]	$\langle$Polydispersity$\rangle$ $\langle \sigma_D \rangle$
Borosilicate Glass	58.8 (17.2%)	46.0 (1.6%)	59.6 (7.7%)	81.2 (0.9%)	0.59 (8.4%)
Soda-Lime Glass	57.1 (4.3%)	49.1 (9.5%)	61.8 (3.1%)	67.0 (1.3%)	0.29 (46.7%)

converting the resulting number-weighted size distribution into a volume-weighted distribution. This conversion process introduces some uncertainty into the analysis, so appropriate care must be taken when comparing the DIH-derived results to measurements on another basis. Detailed uncertainty quantification can also be a subject of a future study.

Since creating the high-speed DIH size distribution curves depends partly on a user-defined data binning procedure, it is also helpful to examine the representative diameters that arise from the raw data. These representative statistics stay fixed for a given analysis and will allow a quantitative comparison of the DIH-derived results to the reference data. The $\langle\ \rangle$ brackets are used to indicate that a given quantity reported in Table 3.2 is the arithmetic mean over all of the associated experimental realizations. The results reported in Table 3.2 suggest that high-speed DIH measurements of representative diameters are within 1–17% of their corresponding reference statistics. By contrast, measurements of polydispersity deviate more strongly from the reference values.

3.3.3 Transient Characterization

Although the analysis of this experiment is primarily focused on the short time interval of 117–122 ms, measurements from earlier times are utilized in Fig. 3.10 to present the overall dispersion behavior that is generally seen with the samples used for this experiment. Fig. 3.10 shows the onset of particles appearing in the interrogation volume around 30 ms, with the number of detected particles growing to some maximum between 50–70 ms. After approximately 90 ms, the number of detected particles settles to a relatively constant value. From this overall behavior, it can be seen that conditions in the ignition zone are likely to reach a steady-state for a period of time after the initial spike of particles appearing in the measurement area. This observation is a critical assertion for the repeatability and consistency of the MIE measurement. The following transient measurement results demonstrate how the experimental system can be used to assess conditions in the ignition zone of the MIE device. It is important to note that Fig. 3.10 describes the physical behavior observed in the ignition zone, and does not imply that the experimental system's detection process varies in efficiency over time. While the general dispersion behavior described above is typical, the specific time and count values will vary depending on the sample and the dispersion conditions.

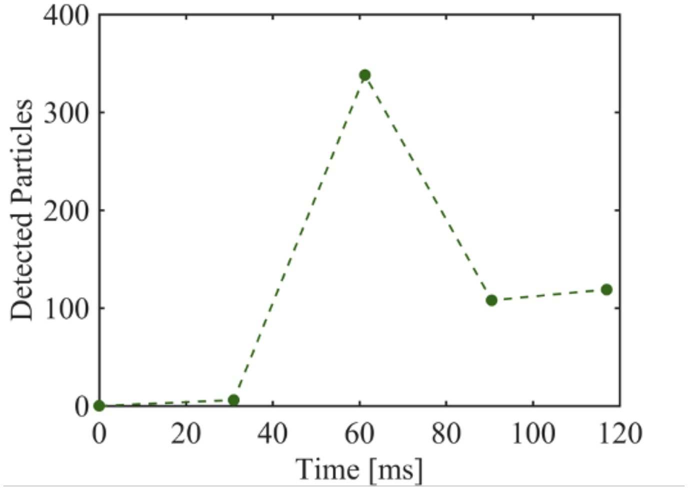

Figure 3.10: Number of borosilicate glass particles detected in the interrogation volume over time (Run 1). Reprinted from [79].

Transient volume, concentration, and in-plane velocity information from the borosilicate glass and soda-lime glass dispersions are shown in Figs. 3.11 to 3.13 to demonstrate how different dust types can present different transient profiles in the ignition zone near the mean ignition time of 119.437 ms. For these measurements, an error bar width of two standard deviations is used to characterize the spread of the data. Thus, the error bar half-width of one standard deviation shows roughly the average distance of the data from either side of the mean. Fig. 3.11 shows a comparison between the total measured particle volume in the ignition zone as a function of time for both samples. Although both volume profiles are relatively constant over the 5 ms measurement period, the borosilicate glass dispersions show almost 8× more volume of material in the ignition zone at this steady-state. The amount of material present in the ignition zone has important implications for the ignitability of a given dust sample.

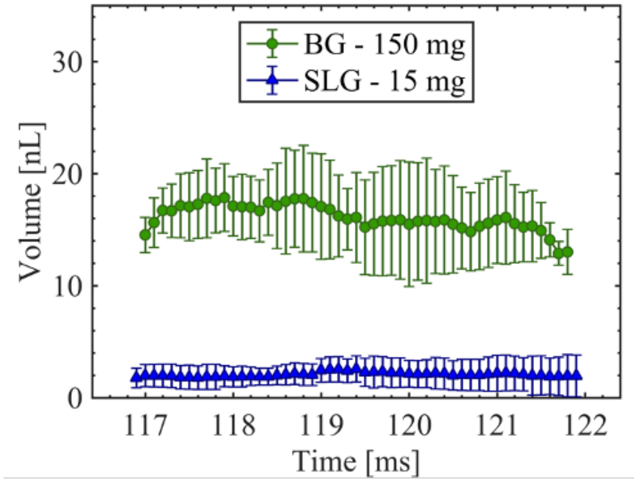

Figure 3.11: Transient volume profiles for the borosilicate glass (BG) and soda-lime glass (SLG) particles detected in the ignition zone. Error bar width is two standard deviations. Reprinted from [79].

A transient concentration can then be computed from the total volume of detected particles by using the density of the two materials, 2.23 g/cm^3 and 2.5 g/cm^3, for borosilicate glass and soda-lime glass, respectively. This concentration measurement represents a resolution improvement over the current convention to assign a nominal concentration to dispersion by dividing the mass loading by the total volume of the dispersion tube (1.2 L). Fig. 3.12 shows that the measured concentrations for the borosilicate glass dispersions differ from the nominal concentration of 125 g/m^3 by approximately 40%. Comparatively, the measured concentrations from the soda-lime glass dispersions differ from the nominal concentration of 12.5 g/cm^3 by approximately 10%. While assuming a uniformly distributed dust cloud is often reasonable, these results suggest that high-speed DIH can improve our understanding of critical conditions like the concentration of dust in the ignition zone. In future studies, collecting detailed concentration measurements at the time and place of ignition may be an essential step towards developing customized risk assessment strategies for different dust formulations and computational models for dust dispersion processes.

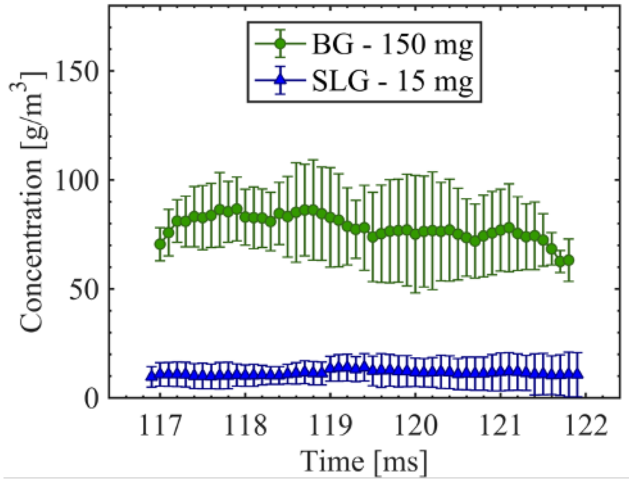

Figure 3.12: Transient concentration profiles for the borosilicate glass (BG) and soda-lime glass (SLG) particles detected in the ignition zone. Error bar width is two standard deviations. Reprinted from [79].

Finally, it is of interest to assess how the dynamic behavior of different particle dispersions differs in the ignition zone. Here the mean planar (x-y) velocity of all dust particles detected in a given hologram is plotted in Fig. 3.13 for both samples over the 5 ms measurement period. The planar velocity of a given particle is given by $V_{xy} = \sqrt{V_x^2 + V_y^2}$. These planar velocity profiles show that both samples exhibit the same average velocity behavior. However, the amount of scatter in the data for the soda-lime glass sample is larger than that seen in the borosilicate glass sample. This variation in behavior may reflect that the borosilicate glass sample disperses more consistently than the soda-lime glass sample. However, the scatter also suggests that more experimental realizations are required before making conclusions. Histograms of the mean x and y component velocities are shown in Fig. 3.14 to further explore the velocity variance observed in the SLG sample. It can be seen in Fig. 3.14 (a) that the mean x-velocity histogram appears gaussian-like, which is reasonable given the symmetry of the MIE tube. Conversely, the mean y-velocity histogram in Fig. 3.14 (b) shows velocities distributed over a larger range of values. These values show that over the 5 ms measurement period, the mean particle movement can correspond to falling, hovering, or rising behavior. These initial observations offer some insight into the variance seen in the data, and more detailed analyses may be implemented in future studies.

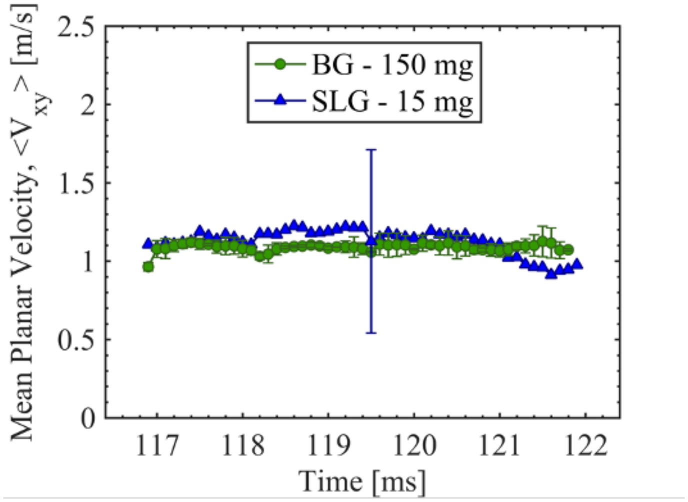

Figure 3.13: Transient mean planar velocity profiles for the borosilicate glass (BG) and soda-lime glass (SLG) particles detected in the ignition zone. Error bar width is two standard deviations. Only one representative error bar for the soda-lime glass sample is included for clarity. Reprinted from [79].

In addition to this, because the interrogation volume is minimal, it is of interest to discern how the dynamic behavior of microscopic dust particles are correlated to the larger flow and turbulence structures that are present in the dispersion tube. In the future, other well-developed velocity and vorticity measurement techniques such as particle image velocimetry (PIV) could be implemented together with high-speed DIH for enhanced understanding of the particle flow behavior.

3.4 DIH Conclusions

In conclusion, the present study demonstrates that high-speed DIH can be highly desirable for in-situ particle diagnostics in the dust explosion and process safety research fields. By coupling this versatile laser diagnostic method with the well-established testing methodology for the MIE, this research reveals an appealing pathway towards addressing fundamental dust cloud formation, ignition, and flame propagation processes within an industry-relevant context. The application of high-speed DIH in this work establishes particle characterization capability for spherical particles over a range of representative particle conditions. The high-speed DIH method was able to generate

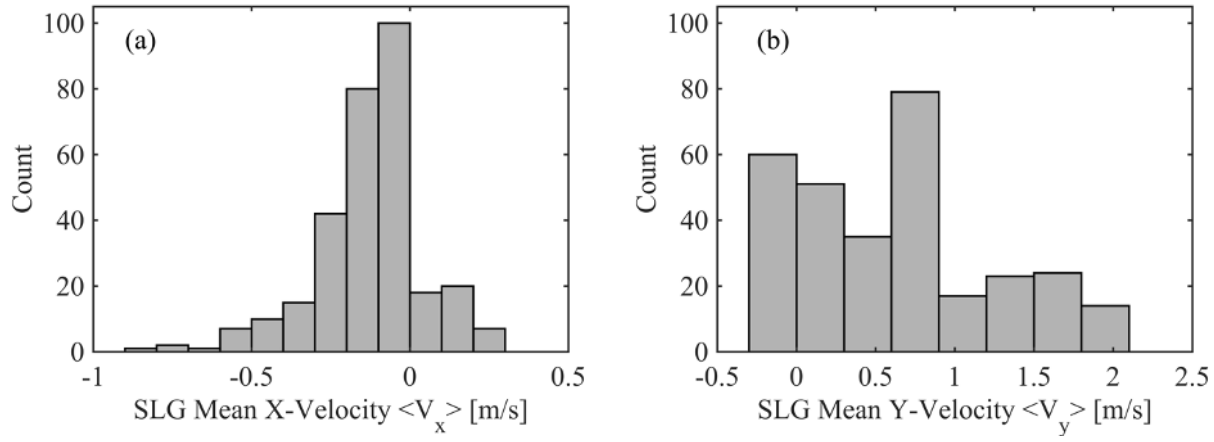

Figure 3.14: Mean x and y component velocities for the soda-lime glass (SLG) sample. Reprinted from [79].

dynamically measured particle size distributions with 5 ms of video and with mass loadings of 15 mg for soda-lime glass and 150 mg for borosilicate glass. The high-speed DIH results show a reasonable agreement with the reference particle size distributions obtained with a laser diffraction particle size analyzer. The high-speed DIH method also enabled the measurement of transient volume, concentration, and velocity profiles for borosilicate glass and soda-lime glass particles in the ignition zone. These results show that variations in dispersion behavior at the time and location of ignition can be measured and compared, which is a unique capability of the high-speed DIH method. While the present results are encouraging, this study has also revealed several areas of improvement that may be addressed in future experiments.

Most importantly, it is apparent that more experimental realizations are needed to produce statistically averaged results along with detailed uncertainty quantification. Also, the characterization of non-spherical morphologies is of interest. Furthermore, the mass loading and particle sizes that are used for the current high-speed DIH demonstrations are limited in applicability with respect to standard MIE testing. The provisional upper limit for mass loadings established by this experiment is 150 mg. The resulting nominal concentration of 125 g/m^3 is 0.5× smaller than the loading that is recommended as a starting point for standard MIE testing. In further studies, the potential for extrapolation of high-speed DIH data to larger mass loading scenarios can be investigated. The data produced by the high-speed DIH system might also be highly valuable to dust characterization efforts that require limited material usage, and may serve as critical validation data for 3D, time-resolved dust dispersion computational models. The practical constraints imposed by this unique experimental combination present new opportunities for high-speed DIH method development. Conversely, future high-speed DIH studies may provide unique insights to inform the design of new process safety equipment and experiments.

4. COMBINED DIGITAL IN-LINE HOLOGRAPHY AND PARTICLE IMAGE VELOCIMETRY FOR DUST CLOUD PARTICLE AND FLOW DIAGNOSTICS*

4.1 DIH & PIV Introduction

Dust fires and explosions pose a severe threat to people, assets, and the environment across a wide range of industries [1, 3]. To identify hazards and manage risks, key ignitability and explosibility properties of dust materials, such as the minimum ignition energy (MIE), must be measured [5]. The MIE of a dust cloud is the lowest energy required to ignite the combustible dust-air mixture with a high-voltage spark discharge. The MIE can thus predict the likelihood of a dust cloud igniting during industrial processing and handling activities. Dust cloud MIE values can be measured using a standard method such as ASTM E2019 [11] and testing equipment such as the MIKE3 device. The MIKE3 device is also employed for studying fundamental aspects of dust cloud ignitability since test conditions can be controlled, the data is familiar, and the resulting insights can be readily transferred to industry. However, conventional MIE measurements are insufficient to resolve the multi-scale physics and chemistry of dust explosions, and advanced methods must be developed to probe the dust cloud dispersion, ignition, and flame propagation processes that evolve inside the MIKE3 device. Laser measurement approaches offer promising pathways to new experimental investigations with the MIKE3 device through in-situ, non-intrusive, and multi-dimensional measurement capabilities.

While many different techniques can be used to study dust explosions, laser diagnostic methods offer several key advantages. Unlike measurement strategies that use physical probes, laser diagnostic methods enable non-intrusive measurements since cameras can passively image the dust cloud from a safe distance, and laser probes can traverse the measurement space with minimal effect on the flow or chemistry. Laser diagnostic methods can thus be implemented for in-situ

---

*Reprinted with permission from "Investigation of aluminum dust cloud dispersion characteristics in an explosion hazard testing device using laser-based particle and flow diagnostics" by C. Schweizer, C. V. Mashuga, and W. D. Kulatilaka, 2022. *Process Safety and Environmental Protection*, vol. 166, pp. 310-319, Copyright [2022] by Institute of Chemical Engineers. Published by Elsevier Ltd.

measurements in extreme environments, where physical probes might disturb the dust cloud or get damaged from the combustion. Finally, modern high-speed cameras enable time-resolved investigations, and sophisticated lens and laser configurations allow for 2D and 3D measurements at the relevant spatial scale.

Despite these advantages, achieving a comprehensive understanding of dust cloud ignitability remains a complex challenge. Measured dust cloud MIE values are influenced by many factors, including attributes of the spark circuit [20, 21, 29, 30], characteristics of the dust particle such as the particle size distribution [24], polydispersity [25], and morphology [27, 28], the composition of the oxidizer [32, 34], and turbulence levels [35]. From these studies, it is clear that dust cloud ignitability is dependent on both particle and flow behavior. Since the macroscopic dust cloud may be much larger than the micron-sized particles that comprise it, acquiring particle and flow diagnostics at the appropriate scales is a difficult task.

To extend the current state of experimental dust cloud MIE research and study the dust cloud dispersion process in MIE testing equipment, digital in-line holography (DIH) was used in a previous study to demonstrate new in-situ dust cloud characterization capabilities [79]. DIH is a three-dimensional (3D) imaging and particle diagnostic technique that uses a single coherent light source and camera to create interference pattern images, or holograms, that encode 3D particle position information [42]. These holograms are then numerically refocused to detect, size, and track particles in the measurement volume of interest. These 3D particle diagnostic capabilities were then leveraged to investigate the influence of particle size, polydispersity, density, and morphology on in-situ dust cloud characteristics, such as particle concentration and velocity, in the ignition zone of the MIKE3 device [79–81]. In a follow-on study, a new model system was assembled to mimic the geometry and operation of the MIKE3 device. The new model system enabled an additional laser measurement method, namely particle image velocimetry (PIV), to be implemented for expanded in-situ characterization efforts [82]. PIV is a well-established flow visualization and measurement technique whereby micron- or sub-micron-sized seed particles are entrained in a flow, illuminated by a pair of laser pulses, and imaged with a camera. The displacement of the seed particles over a known time period yields an instantaneous velocity measurement that can be determined over the entire area of interest [54]. With an experimental apparatus combining DIH and PIV, the measurable area inside the MIKE3 device is expanded, enabling micro- and macro-scale investigations of the dust cloud dispersion process.

In the present study, DIH and PIV are combined to measure aluminum dust clouds, from 15-mg mass loadings, in the MIKE3 glass tube. Quantitative size and velocity measurements from the micron-sized aluminum dust particles are produced with the DIH configuration, and quantitative flow velocity and vorticity measurements are made with the PIV configuration. To investigate the variability of the dust cloud dispersion process, thirty independent dust dispersions are measured with each method. The measured quantities are then examined in detail to determine underlying particle and flow behavior trends. The large number of experimental repetitions allows for the wide range of possible dust cloud behaviors to be observed, and reduces our uncertainty in the average trends. While the DIH and PIV measurements are not collected simultaneously, velocity measurements from each method are compared. The experimental apparatus, sample selection, and data analysis are described in detail in Section 4.2. The results obtained from this experiment are reported and discussed in Section 4.3. Finally, the major conclusions of this work and areas for future study are summarized in Section 4.4.

4.2 DIH & PIV Experimental

To develop advanced diagnostic methods for dust cloud characterization studies, a model dust dispersion system is assembled to mimic the testing environment of the MIKE3 device. The experimental apparatus, which can be seen in Fig. 4.1, uses the standard MIKE3 nozzle, glass tube, and lid assembly to closely simulate the geometry of the original device. Additionally, the experimental apparatus is assembled on an optical table without the standard enclosure to enable the precise alignment of components and provide unobstructed optical access to the measurement region inside the glass tube. Timing and control instrumentation is then used to synchronize the dust cloud dispersion event with subsequent DIH and PIV measurements.

A simplified schematic of the experimental apparatus can be seen in Fig. 4.2. The DIH exper-

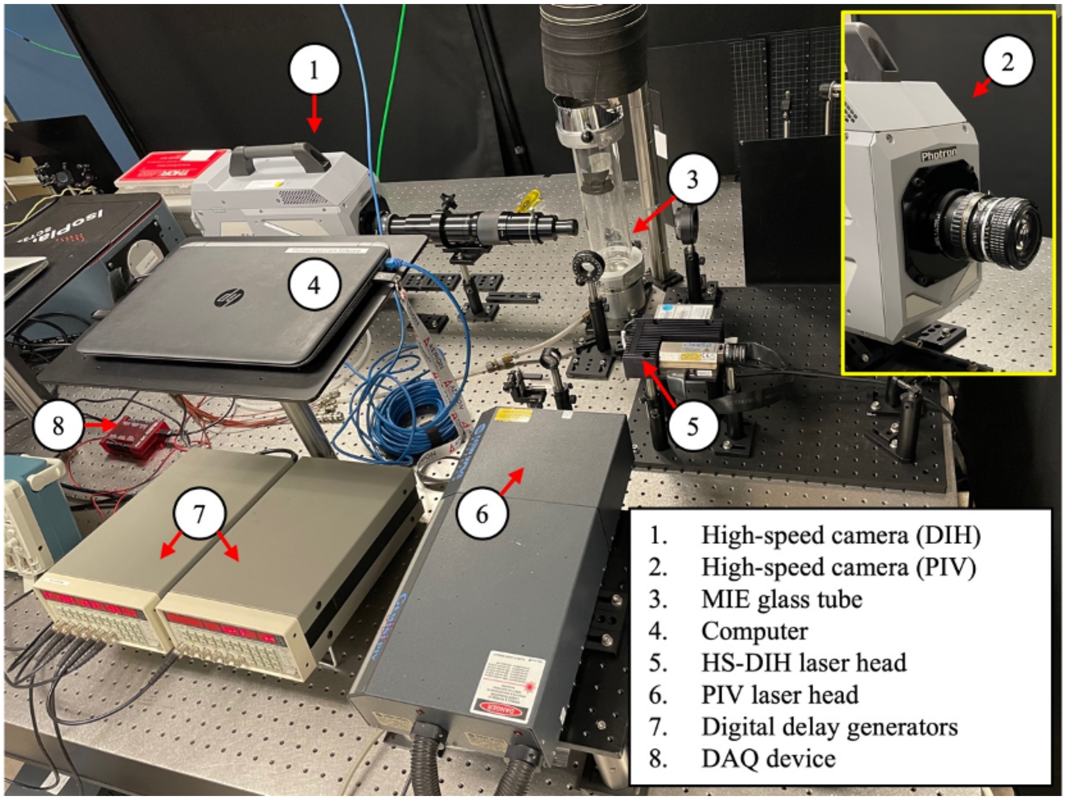

Figure 4.1: Photograph of the experimental apparatus. Reprinted from [93].

imental configuration uses a continuous-wave, diode-pumped solid-state laser (Oxxius, 532 nm, 250 mW), a high-speed camera (Photron FASTCAM SA-Z, monochrome, 1024 pixel × 1024 pixel) fitted with a long-distance microscope lens (Infinity K2 DistaMax with CF-4 objective), and the combination of optics as shown to produce 3D particle diagnostic measurements. Analysis of a 1951 USAF resolution test chart calibration image yields an effective pixel size of approximately 3.49 μm/pixel, and an image size of approximately 3.58 mm × 3.58 mm. The PIV experimental configuration uses a dual-pulse, Nd:YAG laser (New Wave Research Gemini, 532 nm, 250 mJ/pulse, 5-ns pulse duration), a high-speed camera fitted with a visible camera lens (Nikon, 50-mm, f/1.2), a 532 nm bandpass filter (FWHM = 10 nm), and the combination of optics as shown to produce 2D flow diagnostic measurements. The effective pixel size of the imaging system is quantified using a calibration image of a ruler and estimated to be 50 μm/pixel, with a corresponding image size of approximately 51.2 mm × 51.2 mm. For both the DIH and PIV configurations, a flexible duct is positioned above the glass dispersion tube to collect fugitive dust in and around the dispersion tube.

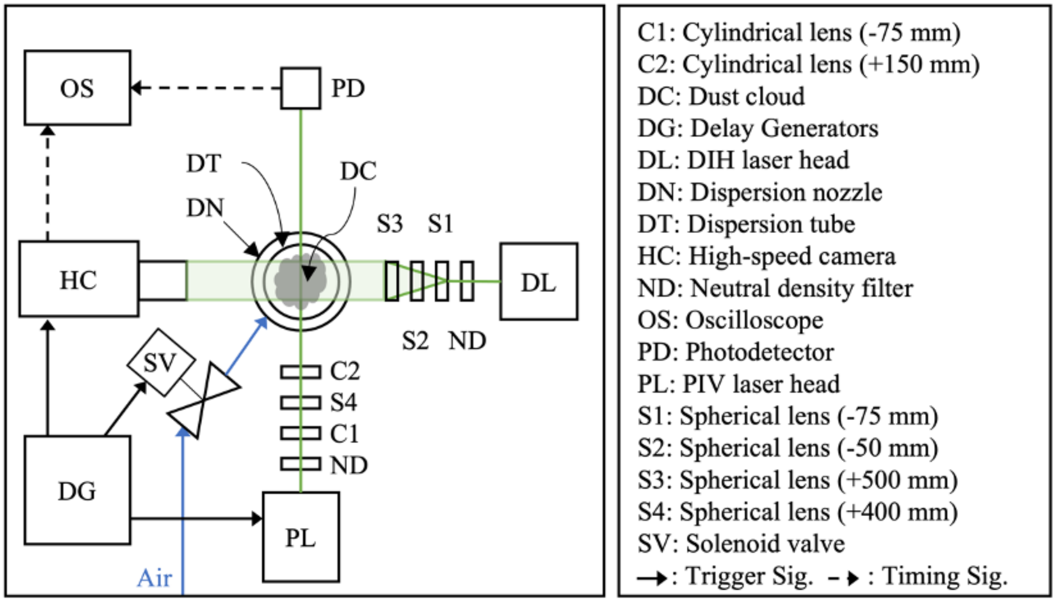

Figure 4.2: Simplified schematic of the experimental apparatus configured for DIH and PIV measurements. Reprinted from [93].

To initiate an experiment, a computer-run Python script enables a data acquisition (DAQ) device (LabJack U3-HV) to produce an analog start signal. To decouple computer-DAQ communication latency from the timing of the experiment, the analog start signal is sent to one of two digital delay generators (Princeton Instruments DG645). After receiving the analog start signal from the DAQ device, the first digital delay generator outputs trigger pulses to the dispersion equipment, the high-speed camera, and the second digital delay generator. The trigger pulse to the dispersion equipment activates a DC solid-state relay to complete the electrical circuit powering a 24-V DC solenoid valve. The solenoid valve is actuated for a preset amount of time, and oxidizer from a compressed air cylinder is then sent through the glass dispersion tube. The trigger pulse to the high-speed camera resets the camera's internal record timing and initiates video capture. The resulting exposure timing is monitored with a digital oscilloscope (Tektronix DPO 2024B, 200 MHz, 1 GS/s) to ensure measurement synchronization. For PIV experiments, the trigger pulse to the second delay generator initiates a subsequent burst of pulses to trigger a train of PIV laser pulse pairs at the desired frequency ($\leq$ 15 Hz). The second digital delay generator is also used to adjust the time separation between each laser pulse in a pair. The resulting train of PIV laser pulse pairs is monitored with a photodetector (Thorlabs DET10A) and the digital oscilloscope to ensure measurement synchronization.

In this work, the experimental apparatus is configured to disperse dust clouds with a 50-psi supply pressure from the compressed air cylinder. This pressure was selected to simultaneously accommodate the competing constraints of the DIH and PIV measurement systems. Large dispersion pressures resulted in suspended particle concentrations that were too large for individual particle detection and tracking by DIH. Conversely, small dispersion pressures resulted in seeding inhomogeneity that was unsuitable for reliable flow tracing by PIV. Additionally, no ignition electrodes are fitted into the glass tube to establish a baseline flow configuration. Since no sparks can be generated for measurement synchronization, as was done in previous studies [79–81], an artificial target signal is generated by one of the digital delay generators. This target signal appears 120 ms after the solenoid valve is actuated, which simulates the spark timing of a typical MIKE3 MIE test. The subsequent DIH and PIV measurements are centered on the target signal using the timing signals and the digital oscilloscope. Additionally, the DIH and PIV lasers are positioned such that the resulting probe regions coincide with the central ignition zone. The geometry for this experiment can be seen in Fig. 4.3 (a). Therefore, even though the ignition electrodes are not present, quantitative data can be extracted from dispersed dust clouds at the typical time and location of ignition. It is important to note that the experimental apparatus currently does not accommodate simultaneous DIH and PIV measurements. Thus, separate experiments are required for measurements with each laser configuration.

With the given experimental configuration, a 15-mg sample of aluminum powder (Sigma-Aldrich, spherical, supplier specified mean size $\leq$ 30 μm) is selected. This sample represents a dust material with broad industrial and safety relevance [83], and also satisfies the particle detection and flow tracing constraints of DIH and PIV, respectively. For the DIH configuration, video is recorded at 20 kHz to accurately track fast-moving dust particles over micrometer length scales.

For the PIV configuration, a 10 Hz train of laser pulse pairs, with an intra-pair pulse separation of 250 µs, is recorded at 4 kHz to appropriately track particle displacements from the dispersion event over a larger area. To compensate for varying sampling rates, downstream data processing only considers measurements collected over the same time period. This time period is constrained by the PIV laser pulse pair separation of 250 µs. Thus, six raw DIH images and two raw PIV images are produced per experiment. The sampling schemes for each laser measurement method can be seen in Fig. 4.3 (b).

In this work, experiments are repeated until thirty successfully-processed cases are produced for each measurement configuration. To ensure the independence of experiments, excess dust from a completed dispersion is completely removed from the nozzle cup and glass tube. A new 15-mg sample is then loaded into the nozzle cup for the subsequent dispersion.

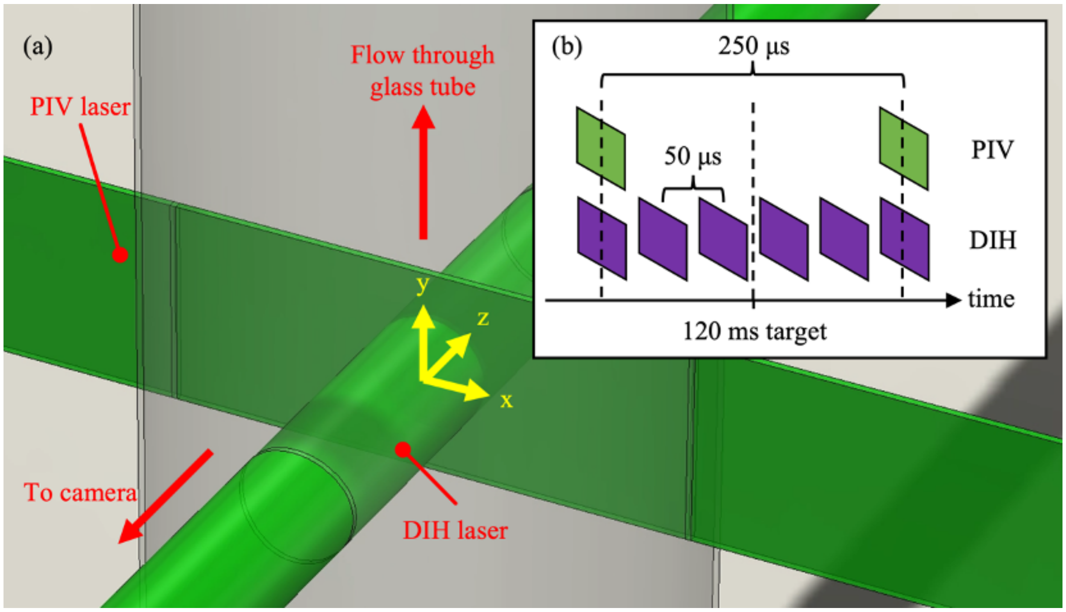

Figure 4.3: (a) Experimental geometry and (b) sampling schemes for the DIH and PIV measurement configurations. Reprinted from [93].

The raw DIH data is processed using the particle detection and tracking methods developed and described in previous publications [76, 77]. The processing codes [53] numerically refocus each raw hologram using Eq. 4.1:

$$E(x, y; z) = \mathcal{F}^{-1}\left\{\mathcal{F}\{I_0(x, y)\} \cdot \exp\left(\frac{2\pi i z}{\lambda}\sqrt{1 - \lambda^2 f_x^2 - \lambda^2 f_y^2}\right)\right\} \tag{4.1}$$

Here, $E(x, y; z)$ is the reconstructed complex amplitude distribution at the specified depth along the optical axis z, I_0 is the intensity distribution of the experimental hologram, $\mathcal{F}$ is the Fourier transform, λ is the laser wavelength, and f_x and f_x are the transverse spatial frequencies. The reconstructed intensity distribution at the specified depth z is then calculated with $I(x, y; z) = |E(x, y; z)|^2$. Using minimum intensity and maximum edge sharpness focus criteria, a hybrid algorithm is then implemented to detect particles in the volume of interest and determine their corresponding 3D spatial locations. Detected particles can then be tracked across subsequent camera frames to reveal trajectories through the ignition zone. Thus, quantitative size, position, and velocity data are extracted from the particles detected in the volume of interest.

The raw PIV data processing is conducted using commercial software (LaVision Davis). Particle displacement vectors throughout the measurement area are calculated by cross-correlating sub-regions of the flow from two sequentially-captured particle images. The particle displacement vectors, combined with the known change in the time between the illuminating laser pulses, yield an instantaneous velocity vector field. From this description, it is clear that PIV inherently measures the distribution of seed particle velocities in the measurement area. However, if the seed particles can quickly adjust to the motion of the surrounding fluid, the particle velocity is approximately equal to the fluid or flow velocity. This flow tracing fidelity can be characterized by the Stokes number, with values less than 0.1 corresponding to flow tracing accuracy with errors less than 1% [84]. The velocity estimation is given by Eq. 4.2:

$$\vec{v} = \frac{\Delta\vec{L}}{\Delta t} \approx \vec{u} \tag{4.2}$$

Here, $\vec{v}$ is the instantaneous particle velocity vector, $\Delta\vec{L}$ is the particle displacement vector, Δt is the change in time, and $\vec{u}$ is the instantaneous flow velocity vector. Assuming a 2D flow, the vorticity, or local spinning motion of the fluid, can then be calculated with Eq. 4.3:

$$\omega = \frac{\partial u_y}{\partial x} - \frac{\partial u_x}{\partial y} \tag{4.3}$$

Here ω is the vorticity scalar, u_x is the x-component of the flow velocity vector, and u_y is the y-component of the flow velocity vector. Lastly, the turbulence level can be characterized by the root-mean-square (RMS) of the flow velocity fluctuations. The RMS velocity for the given vector component is calculated with Eq. 4.4:

$$u_{\text{RMS}} = \sqrt{\frac{1}{N}\sum_{i=1}^{N}(u_i - \bar{u})} \tag{4.4}$$

For a given position in the PIV measurement area, u_{RMS} is the RMS velocity, u_i is the flow velocity in the i^{th} PIV realization, $\bar{u}$ is the mean flow velocity, and N is the total number of PIV realizations in the ensemble. Pre- and post-processing operations, such as area masking and filtering, are also applied to the raw PIV data to improve the fidelity of the results.

4.3 DIH & PIV Results and Discussion

4.3.1 DIH Particle Diagnostics

From each raw DIH image, aluminum particles in the measurement volume are detected and counted. Quantitative size, position, and velocity data are also extracted from the holograms. As seen in Fig. 4.4, the total number of detected particles varies by more than an order of magnitude across thirty experiments. This data emphasizes the stochastic nature of the dust cloud dispersion process and highlights a potential challenge in adequately assessing the characteristics of a given dust cloud with only a limited number of measurements or experimental runs. Additional assessment of the data in Fig. 4.4 showed no significant autocorrelation, suggesting that the data was generated by a stochastic dust dispersion process. A mean of 78 detected particles and a standard deviation of 53 detected particles is calculated. An expanded uncertainty (95% confidence level, coverage factor = 2.045) is also determined, yielding a measurement of the number of detected particles, $n = 78 \pm 20$.

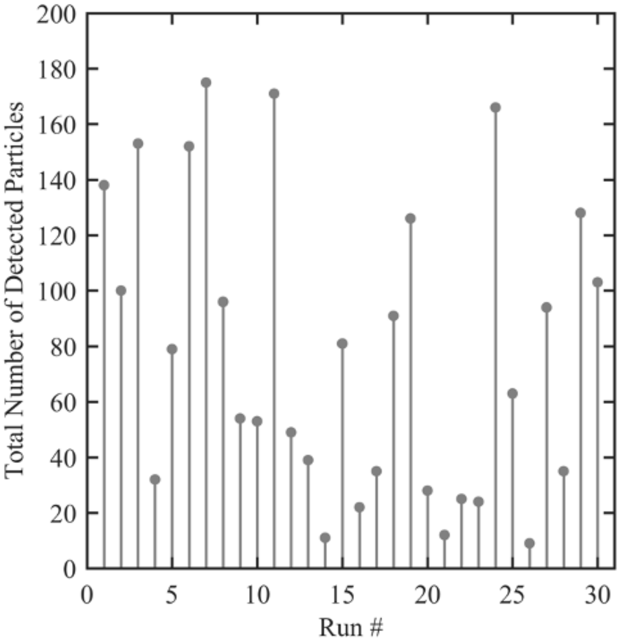

Figure 4.4: Total number of detected particles for each experimental run. Reprinted from [93].

Once the particles are detected and sized, a particle size distribution is created. The particle size distributions from the thirty DIH experiments can be seen in Fig. 4.5, with each curve representing the results from an individual run. Each size distribution gives a visual representation of the range of particles that were detected for each run, and shows which particle sizes are the most prevalent in the ignition zone. A color outline for each curve is also given, which corresponds to the number of particles that were detected at a particular size (right-side ordinate). Finally, the total number of detected particles for each run is included (left-side ordinate), which corresponds to the sum of all particles in the given distribution. It is important to note that the distributions in Fig. 4.5 and Fig. 4.7 are organized in descending order based on the total number of detected particles. This ordering is for visualization purposes only and does not reflect the actual order in which the experiments were completed, as shown in Fig. 4.4. From the thirty experiments, a mean of 18.9 µm and a standard deviation of 1.7 µm is calculated, yielding a measurement for the average detected particle diameter, $\bar{D} = 18.9 \pm 0.6$ µm. These statistics suggest that the average size of detected aluminum particles can be associated with a narrow range of values at the time and location of ignition.

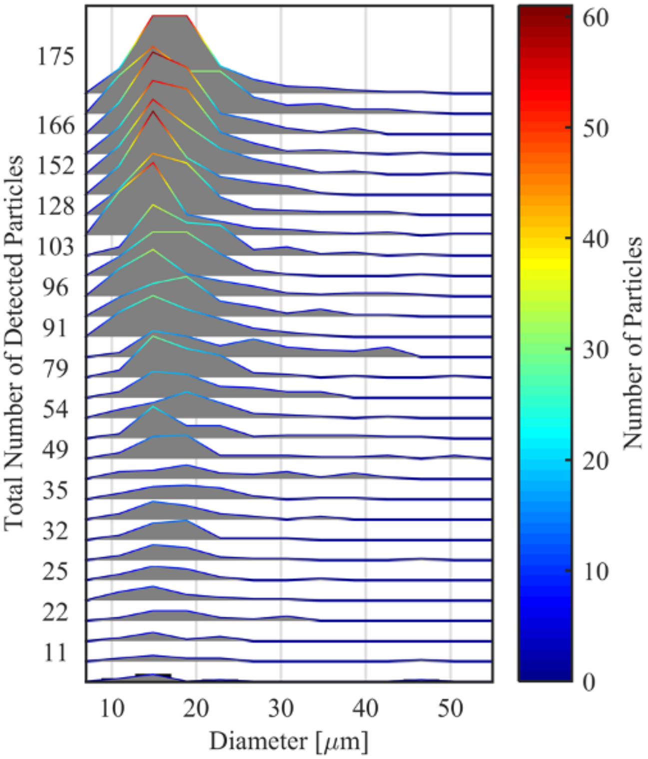

Figure 4.5: Particle size distribution data from thirty DIH experiments. Reprinted from [93].

To extend the characterization of aluminum particle sizes, the data from each DIH experiment are aggregated to yield a combined particle size distribution. Due to the large number of particles in the combined dataset, the resulting histogram seen in Fig. 4.6 (a) is smooth and appears well-characterized by the lognormal distribution: $f(x, \mu, \sigma) = \frac{1}{x\sigma\sqrt{2\pi}} \exp\left[-\frac{(\ln(x)-\mu)^2}{2\sigma^2}\right]$ (parameters: $\mu = 2.89$, $\sigma = 0.31$), which is observed in a variety of particle systems [85, 86]. The size distribution is right-skewed with a mean of 18.9 μm, a median of 17.2 μm, and a standard deviation of 6.7 μm. These combined size statistics agree with the initial analysis of particle size data from individual experiments, and give additional insight into the underlying distribution and variability of detected particle sizes.

To validate the size data measured with DIH, the combined particle size distribution is con-

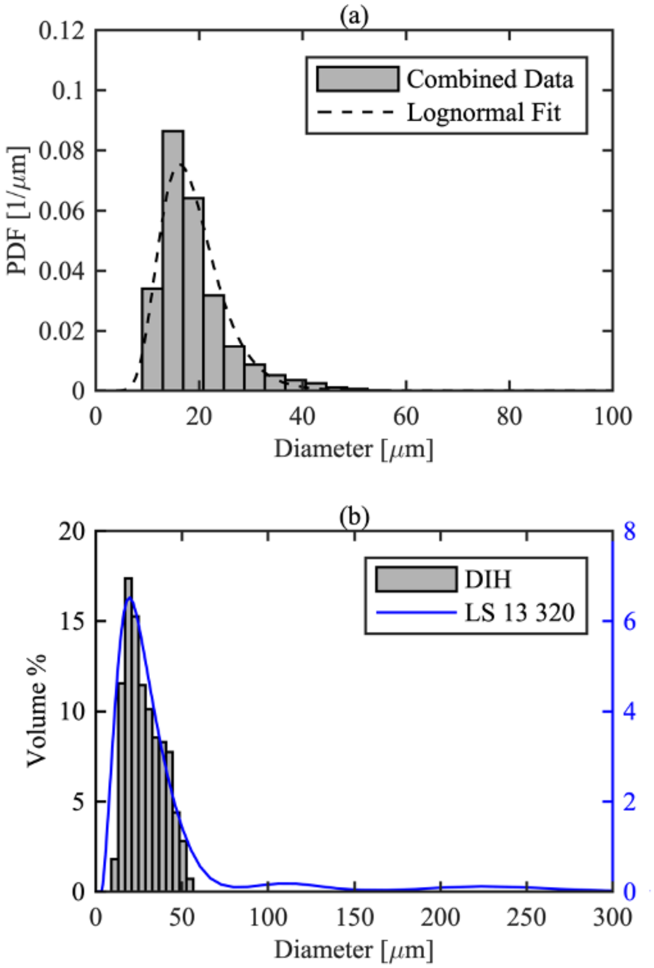

Figure 4.6: (a) Combined particle size distribution and (b) volumetric size distribution comparison. Reprinted from [93].

verted into a volumetric size distribution and compared with the results from a laser diffraction particle size analyzer (Beckman Coulter LS 13 320), which also generates a volumetric size distribution. From the volumetric size distributions shown in Fig. 4.6 (b), the primary mode around 20 µm is well-captured by the DIH result, along with the decreasing trend to 50 µm. However, the second and third modes near 125 µm and 225 µm are not observed. This discrepancy may arise because the particle size analyzer creates its volumetric size distribution through an ex-situ analysis, during which the entirety of the given sample is processed. By contrast, the DIH configuration

Table 4.1: Particle size statistics measured using DIH and the Beckman Coulter LS 13 320 particle size analyzer. Reprinted from [93].

	D(0,0) [μm]	d_{10} [μm]	d_{50}	d_{90}	σ_D
DIH	17.9	15.8	26.0	42.5	1.03
LS 13 320	7.9	8.9	19.1	38.9	1.58

measures the dust cloud at a specific time, location, and flow condition. For the given particle-flow combination, the DIH result suggests that particles larger than 55 μm are rarely seen at the time and location of ignition, even if such particles are generally present in the sample. Since the local particle size distribution in the ignition zone will impact whether ignition occurs, characterizations based on in-situ measurements might be necessary to assess dust cloud ignitability accurately.

A comparison of particle size measurements between the DIH and particle sizer analyses can be seen in Table 4.1. The geometric mean diameter or D(0,0) is relevant in particle size distribution analysis as it is equal to the number median diameter of the lognormal distribution [87]. Good agreement is observed in the DIH results between the calculated D(0,0) value of 17.9 μm, and the previously mentioned median diameter of 17.2 μm, which provides additional evidence that the particle sizes are lognormally distributed. Also included in Table 4.1 are the 10th, 50th, and 90th volume percentile diameters denoted as d_{10}, d_{50}, and d_{90}. The polydispersity is then calculated with $\sigma_D = (d_{90} - d_{10})/d_{50}$. The larger polydispersity value from the particle size analyzer indicates a broader distribution than the distribution measured via DIH, which is also confirmed graphically in Fig. 4.6 (b).

A similar analysis is conducted for the particle velocities measured using DIH. In this work, v_x indicates lateral (right-left) particle motion in the plane of the DIH image, while v_y indicates particle motion along the flow axis (up-down) of the glass dispersion tube. Finally, v_z denotes particle motion in or out of the DIH image plane. Similar to the particle size results, the x-component velocity distributions from the thirty DIH experiments shown in Fig. 4.7 highlight the dust cloud dispersion process variability. Due to the stochastic nature of the dust cloud dispersion event, the motion of the particles in the ignition zone may favor a particular direction during an experiment.

Additionally, the particle motion data spread may differ from experiment to experiment. These observations can be easily seen from the distributions in Fig. 4.7, where individual experiments are biased to either side of zero with varying distribution widths. While a priori knowledge of the flow geometry suggests that the particle motion should produce a roughly symmetrical velocity distribution in the x-component, it may be difficult to confirm this behavior with a limited number of experiments. However, with thirty independent experiments, the expected trend can be confirmed. A mean of 0.05 m/s and a standard deviation of 0.14 m/s are calculated, yielding a measurement for the average detected x-component velocity, $\bar{v}_x = 0.05 \pm 0.05$ m/s.

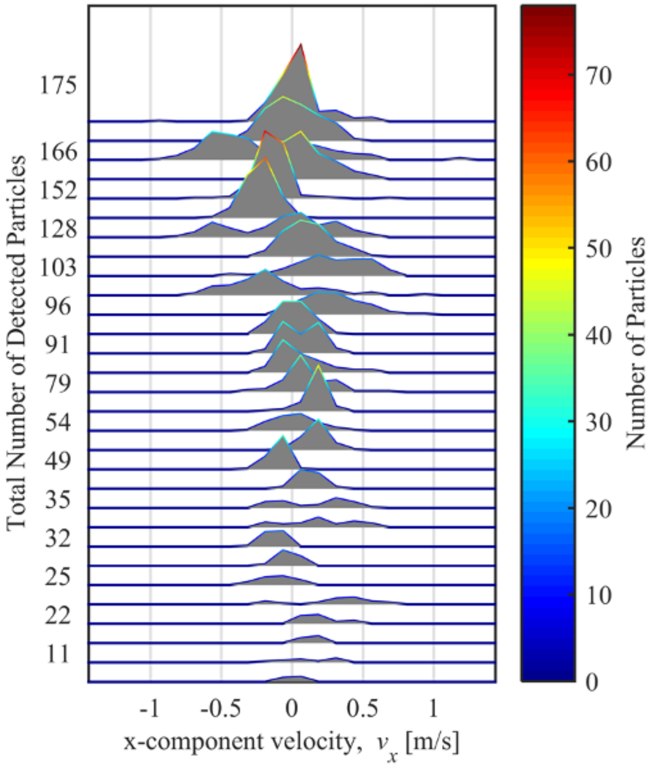

Figure 4.7: x-component particle velocity data from thirty DIH experiments. Reprinted from [93].

Statistics for the average x-, y-, and z-component particle velocities are summarized in Table 4.2. The average x- and z-component particle velocities have similar mean values near zero, with larger relative variability (coefficient of variation) than the average y-component particle velocity. This data, along with the previously mentioned particle number and size statistics, provide

Table 4.2: Statistics for the average particle velocities measured from thirty DIH experiments. Reprinted from [93].

Quantity	Mean [m/s]	Standard Deviation [m/s]	Coefficient of Variation [%]	Expanded Uncertainty [m/s]
$\bar{v_x}$	0.05	0.14	285	0.05
$\bar{v_y}$	0.60	0.23	38.2	0.09
$\bar{v_z}$	-0.07	0.44	-589	0.16

new insight into the dust cloud dispersion process resulting from small-scale mass loadings.

Similar to the particle size data, the velocity data extracted from the thirty DIH experiments are aggregated to yield combined velocity distributions. The smooth histograms seen in Fig. 4.8 (a) enable underlying trends in particle motion to be assessed. The x-component and z-component velocity data present expected symmetrical distributions centered on zero. These observations are consistent with the axially symmetric flow geometry of the dust cloud dispersion event. Higher variability in the measured z-component velocity is observed, which is an inherent by-product of the DIH method. The y-component velocities show a strong positive trend, corresponding to particle motion upward through the glass dispersion tube.

A combined planar velocity distribution for the detected particles is then generated with $v_{xy} = \sqrt{v_x^2 + v_y^2}$. Shown in Fig. 4.8 (b), the planar velocity distribution appears well-characterized by the Weibull distribution: $f(x, \beta, \theta) = \frac{\beta}{\theta}\left(\frac{x}{\beta}\right)^{\beta-1} \exp\left[-\left(\frac{x}{\theta}\right)^{\beta}\right]$ (parameters: $\theta = 0.86$, $\beta = 2.12$), which is often helpful for velocity characterization [88, 89]. From the combined planar velocity data, a mean of 0.76 m/s and a standard deviation of 0.38 m/s are calculated. Additionally, the Weibull scale parameter θ corresponds to a characteristic planar velocity of 0.86 m/s. In other words, 63.2% of all planar velocities are below 0.86 m/s.

To identify additional trends in the dust cloud dynamics inside the MIKE3 glass tube, the joint distribution of particle size and planar velocity is plotted in Fig. 4.9. Each point in the scatterplot represents a single detected particle and its respective size and planar velocity. The correlation between each quantity can be observed, and the most-likely size-velocity pairs can be identified. The joint distribution emphasizes that the distribution of possible planar velocities is conditional

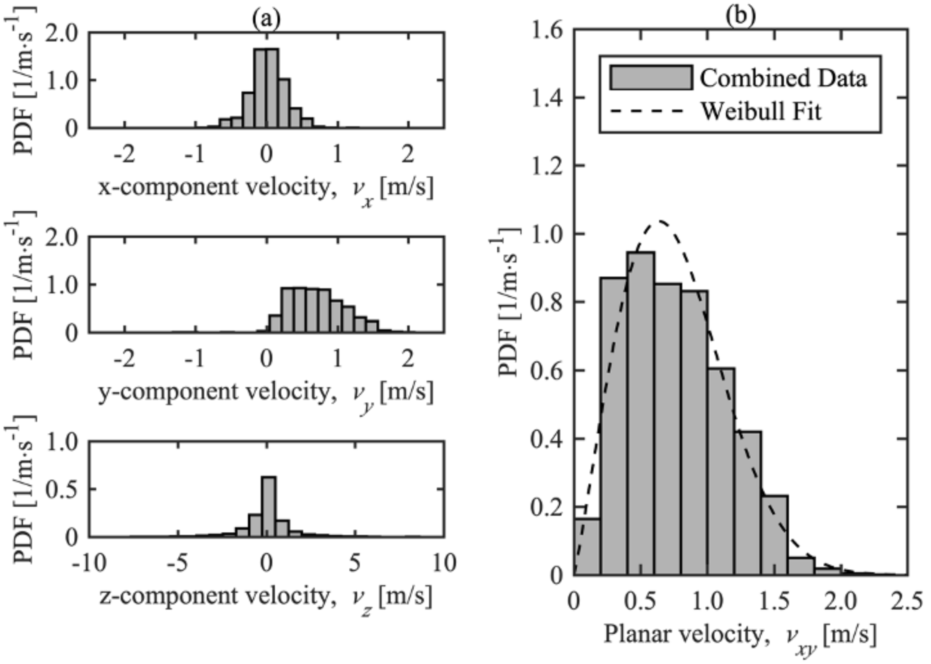

Figure 4.8: (a) Combined single-component velocity distributions and (b) combined planar velocity distribution. Reprinted from [93].

on particle size and vice versa. Conditional probability distributions can be extracted from the joint distribution, and collapsing the data onto either the size or planar velocity axis recovers the individual marginal distributions previously shown in Fig. 4.6 (a) or Fig. 4.8 (b), respectively. While the marginal distributions are amenable to characterization with well-known theoretical distributions such as the lognormal and Weibull distributions, the joint distribution may provide additional utility for prediction or design activities where particle information is limited. Fig. 4.9 also shows a lack of particles smaller than $\sim$10 μm. This observation is explained by the detection limit of the DIH measurement configuration, which depends on the effective pixel size of the imaging system. Smaller particles may indeed be present in the measurement volume, so care must be taken when interpreting size-velocity relationships.

4.3.2 PIV Flow Diagnostics

To complement the detailed particle diagnostics data provided by DIH, the flow velocimetry data from the PIV measurement configuration is analyzed. The Stokes number for the experimental

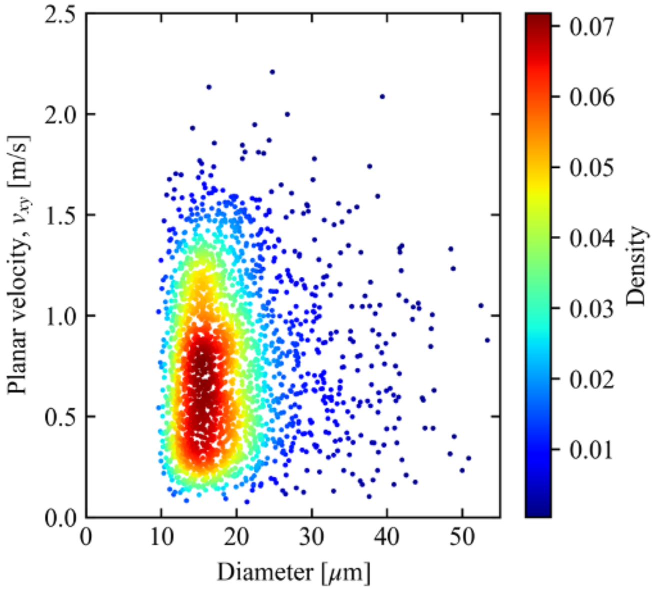

Figure 4.9: Scatterplot of particle sizes and planar velocities. Reprinted from [93].

particle-flow combination is estimated to assess the flow tracing fidelity of the aluminum dust particles. These calculations utilize the lognormal particle size distribution derived from the DIH analysis and external gas velocity data from similar explosion-tube flow studies [90, 91]. The Stokes number is given by $\tau_p u_f / l$, where u_f is the fluid velocity and l is the diameter of the tube. Finally, τ_p is the particle time constant given by $d_p^2 \rho_p / 18\mu_f$, where d_p is the particle diameter, ρ_p is the particle density, and μ_f is the fluid dynamic viscosity. A conservative estimate, using the average particle diameter from the lognormal size distribution, yields an average Stokes number of 0.03-0.04. Additionally, the probability of exceeding a Stokes number of 0.1 is estimated to be less than 5%. Based on these estimates, which capture the flow tracing behavior of the entire distribution of particle sizes, the aluminum particles are expected to trace the flow with acceptable fidelity (tracing errors less than 1% in the majority of cases). For the present study, only data from the central region of the raw PIV images (30 mm width × 20 mm height) are considered. The PIV measurement extent is thus ~45× larger than the DIH image extent. Using the additional z-component velocity data from the DIH measurement configuration, the perspective error due to out-of-plane motion is estimated to be less than 2% of the mean flow velocity, with errors decreasing for locations closer to the optical axis of the camera lens.

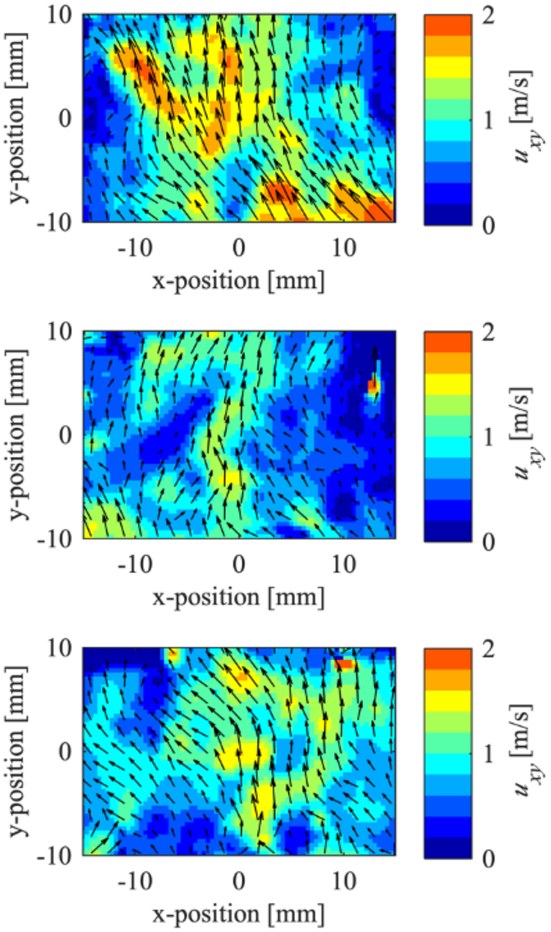

Figure 4.10: Instantaneous flow velocity vector fields from individual PIV experiments. Reprinted from [93].

A sample of three instantaneous flow velocity vector fields, calculated from individual PIV experiments can be seen in Fig. 4.10. The arrows denote the flow velocity vector $\vec{u}$, and the background colormap represents the flow velocity vector magnitude, $u_{xy} = \sqrt{u_x^2 + u_y^2}$. Large-scale flow structures and velocity variations are easily seen from these instantaneous vector fields. The flow velocity magnitudes from these sample fields range from approximately 0 m/s to 2 m/s. This observation is consistent with the DIH-derived planar velocity distribution in Fig. 4.8 (b), which shows most velocities between 0 m/s and 2 m/s.

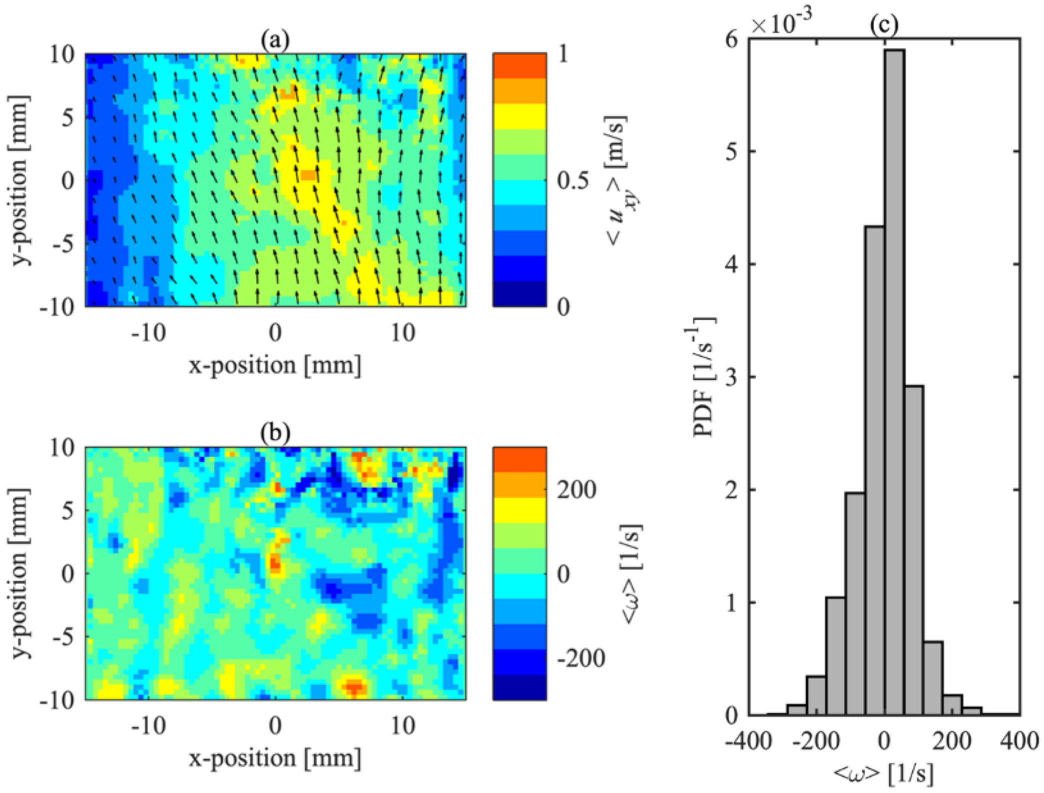

Figure 4.11: (a) Average velocity vector field, (b) average vorticity scalar field, and (c) histogram of the average vorticity values. Reprinted from [93].

An average flow velocity vector field is generated to further assess flow behavior trends in the central ignition region. The average field, which can be seen in Fig. 4.11 (a), is created by taking the arithmetic mean of the instantaneous velocity data from all thirty individual PIV experiments at each measurement point in the image. This average field shows a dominant vertical vector trend, corresponding to the upward flow of compressed air through the tube. Unexpectedly, the average field appears to vary across the measurement area, increasing from left to right. One possible source of this spatial variability could be the relative alignment of the dispersion nozzle's discharge ports to the PIV laser. The average field also shows that a large proportion of average velocities range from 0.5 m/s to 1 m/s, which is consistent with the velocity analysis provided by the DIH measurement configuration. An average flow vorticity scalar field is also generated and shown in Fig. 4.11 (b). Finally, a histogram of the average vorticities is given in Fig. 4.11 (c).

From the histogram, it can be seen that the data is approximately symmetric and centered on zero, with average vorticity values rarely exceeding ± 0.05 rotations per measurement period (± 200 1/s). Since the vorticity calculations rely on a 2D flow assumption, additional effort is required to determine if these calculations adequately capture the vorticity behavior in the MIKE3 glass tube. The RMS velocity is then calculated using Eq. 4.4 to characterize the turbulence in tube. An average RMS velocity of 0.50 m/s over the horizontal centerline of the PIV measurement area is calculated.

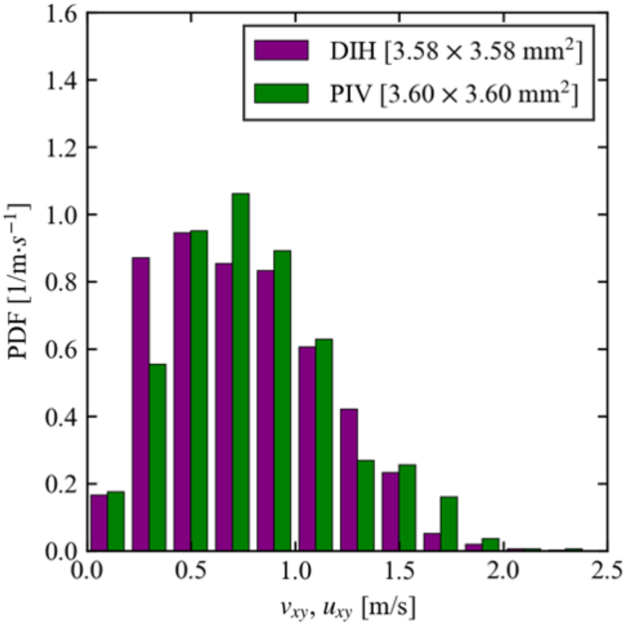

Figure 4.12: Velocity distribution comparison between DIH and PIV. Reprinted from [93].

4.3.3 DIH and PIV Velocity Measurement Comparisons

Finally, the velocity data from the DIH and PIV analyses are compared to assess the similarities and differences between the two methods. For these comparisons, the combined planar velocity distribution, shown in Fig. 4.8 (b), from the DIH analysis is used. Similarly, the PIV velocity data from the thirty individual runs are aggregated to form a corresponding combined flow velocity distribution. Since the full combined PIV dataset includes information from a large spatial extent, subregions of the measurement area can be examined separately. For an initial comparison, PIV measurements are constrained to a planar region close to the DIH image size. Thus, a PIV subregion of 3.60 mm × 3.60 mm is selected. The combined velocity distributions shown in Fig. 4.12 show reasonable agreement between the two methods. Both distributions have most measurements between 0 m/s and 2.5 m/s, and present similar right-skewed shapes.

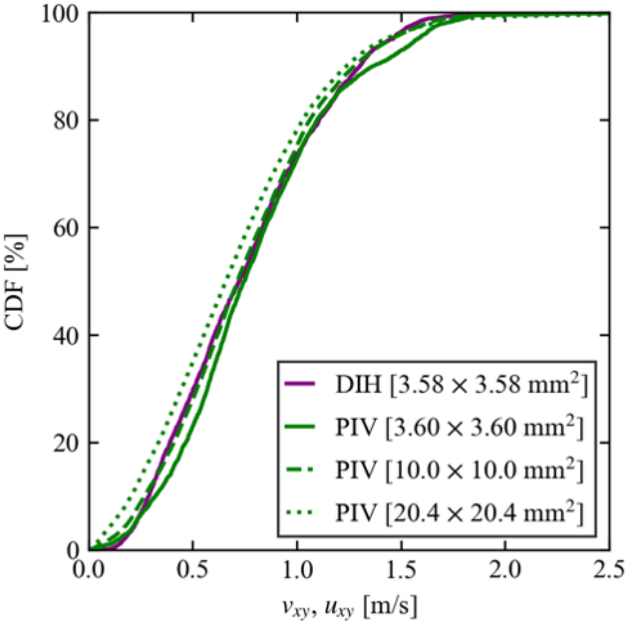

Figure 4.13: Velocity distribution comparison between DIH and PIV for different PIV subregion sizes. Reprinted from [93].

The resulting velocity distributions from increasingly larger PIV subregions are then compared to the DIH distribution in Fig. 4.13. The cumulative distribution function (CDF) curve is used to facilitate the comparison of multiple distributions at once. It can be seen from the curves in Fig. 4.13 that the PIV distributions closely match the DIH distribution, even for larger subregions. However, as the subregions increase in size, the PIV distribution curves begin to exhibit a shift towards smaller velocity values. While general consistency is observed between the DIH and PIV data, it is important to note that the two techniques operate with different working principles, assumptions, and measurement extents. Therefore, care must be taken when interpreting velocity comparison results.

4.4 DIH & PIV Conclusions

The present work constitutes a detailed investigation of aluminum dust cloud dispersion characteristics in the MIKE3 glass tube and demonstrates that a wide variety of quantitative particle and flow data can be collected at the time and location of ignition. The DIH analysis revealed trends for particle sizes and velocities in the ignition zone and yielded new insights into the variability of the dust cloud dispersion process. Particle sizes were observed to follow a lognormal distribution, and particle velocities were observed to follow a Weibull distribution. The PIV analysis yielded velocity and vorticity measurements highlighting flow structures and characteristics over a large spatial extent. Data from the DIH analysis was also leveraged to estimate bounds on flow tracing accuracy and perspective error for the PIV measurement configuration. An initial comparison between the DIH and PIV velocity measurements showed reasonable agreement between the two methods over a range of spatial subregions.

It is important to note that these data and statistics are specific to the dust sample and experimental configuration used for this work. Additional study is required to determine the trends for larger mass loadings and different particle types dispersed with the standard MIKE3 device, which also uses a higher supply pressure of 7 bar. Nevertheless, this work has demonstrated the complementary nature of DIH and PIV and their combined utility for small-scale dust cloud characterization studies. Future work focuses on the development of laser-based diagnostic methods for large dust clouds (> 300-mg) and realistic combustion scenarios.

5. CHEMILUMINESCENCE IMAGING FOR DUST CLOUD IGNITION DIAGNOSTICS*

5.1 Chemiluminescence Introduction

Dust fires and explosions present severe and often unrecognized risks in many industries [3]. Therefore, dust ignitability and explosibility properties must be measured to identify hazards and implement appropriate safeguards in industrial facilities [5]. One crucial parameter is the minimum ignition energy (MIE). The MIE of a dust cloud is the lowest energy required to ignite the combustible dust-air mixture with a high-voltage spark discharge. Dust cloud MIE measurements help predict the likelihood of dust cloud ignition during solids handling activities and are essential for determining the grounding and bonding requirements for plant equipment [92]. Reliable dust cloud MIE measurements are made with testing equipment like the MIKE3 device according to standard methods such as ASTM E2019 [11]. Ultimately, the testing of dust materials for compliance with consensus codes, standards, and regulations constitutes an essential element of modern industrial risk management systems [6].

The MIKE3 device and similar vertical explosion tube setups have also been used to study fundamental aspects of dust cloud ignitability. These experiments are appealing because they can reliably produce dust explosions, the data is familiar, and the resulting insights are readily transferable to industry. Previous studies have demonstrated that dust cloud MIE values are influenced by particle characteristics such as the size distribution [22, 23], polydispersity [25], and morphology [27, 28]. Aspects of the testing environment, such as the spark discharge method [29, 31] and the oxidizer composition [33, 34] can also lead to varied MIE results. These findings are consistent with the dust explosion pentagon, a conceptual model similar to the fire triangle, which establishes fuel, oxidizer, mixing, confinement, and ignition as essential causation factors [6].

To complement conventional MIE data, advanced measurement methods have also been devel-

---

*Reprinted with permission from "Investigation of niacin and aluminum dust cloud ignition characteristics in an explosion hazard testing device using high-speed imaging" by C. Schweizer, C. V. Mashuga, and W. D. Kulatilaka, 2022. *Process Safety and Environmental Protection*, vol. 166, pp. 320-327, Copyright [2022] by Institute of Chemical Engineers. Published by Elsevier Ltd.

oped to resolve the underlying physics and chemistry of dust cloud combustion. Recent experiments in vertical explosion tube setups have leveraged cameras, lasers, and other sensors to collect high-resolution data from dust clouds. For example, digital in-line holography (DIH) was used in a series of experiments to collect quantitative particle data from dispersed dust clouds prior to ignition [79–81] inside the MIKE3 vertical tube. These investigations demonstrated that particle properties like size, density, and morphology can influence the particle concentrations and velocities measured near the ignition electrodes. Follow-on studies have combined DIH with particle image velocimetry (PIV) to enable micro-scale particle and macro-scale flow measurements in the MIKE3 glass tube [82, 93]. The statistics from many repeated experiments were used to accommodate the stochastic nature of the dust cloud dispersion process, and characterize the particle and flow trends in the ignition zone. In addition to these dust cloud dispersion investigations, many experiments have focused on the flame propagation behavior of burning dust clouds, yielding flame temperature and flame speed measurements from a variety of dust materials [91, 94, 95]. Chemiluminescence imaging has also been implemented [96, 97] to obtain species-specific data from the dust cloud combustion reaction zone. Chemiluminescence in flames refers to the emission of light from chemically excited species as they return to their electronic ground state. Excited-state species can be formed through collisions and destroyed via spontaneous emission and collisional quenching. In hydrocarbon flames, excited-state radicals such as hydroxyl (OH*) and methylidyne (CH*) help mark the reaction zone and flame front, respectively [58]. Therefore, flame chemiluminescence can be leveraged to analyze the flame structure in burning dust clouds with improved specificity. Also, in contrast to the aforementioned vertical tube investigations, some experiments have used transparent balloons to investigate dust flame propagation at nearly constant pressure conditions and with minimal wall effects [98, 99].

In the present work, high-speed and species-specific (OH* and CH*) imaging is implemented to measure spark-ignited dust clouds inside the MIKE3 device. The focus of this work is on the early flame kernel development process in the central ignition region for 10 ms after the ignition spark. Quantitative flame kernel size, position, and velocity measurements are extracted from high-speed image sequences using an intensity thresholding algorithm. Niacin and aluminum dust samples are selected to investigate the combustion behavior arising from an organic and metal fuel, respectively. Aluminum is commonly found in industrial settings and is well-studied due to its numerous applications, for example, as a solid rocket propellant additive [100, 101]. Niacin is also well studied and is regularly used for international calibration and certification activities [102]. Additionally, qualitative observations of the flame structure and propagation behavior of the two dust types are discussed in detail.

The present work describes a unique experiment to combine high-speed broadband, OH*, and CH* imaging for in-situ and non-intrusive flame kernel measurements inside the standard MIKE3 device. It demonstrates advanced dust cloud ignition and combustion measurements that are fully compatible with the operation of the MIKE3 device and the production of standard MIE data. Most previous flame propagation studies in similar configurations and spatial domains have had limited temporal and spatial resolution or reduced sensitivity. Furthermore, earlier studies have focused on tracking the leading flame edge for flame speed measurements, rather than focusing on the growth and motion of the flame kernel itself. Therefore, this work represents a substantial investigation of dust cloud ignitability within the context of an industry-standard testing environment. Additionally, when chemiluminescence imaging was employed, either OH* or CH* were solely detected. Some previous studies were also conducted in non-standard or modified devices, as opposed to industry-standard MIKE3 MIE testing devices. The experimental apparatus, dust sample selection and preparation process, and data analysis procedure are described in Section 5.2. The results obtained from this experiment are reported and discussed in Section 5.3. Finally, the major conclusions of this work and areas for future study are summarized in Section 5.4.

5.2 Chemiluminescence Experimental

5.2.1 Dust Cloud Ignition and Imaging Apparatus

The experimental apparatus used for this work is shown in Fig. 5.1. Dust clouds were created and ignited with a dust cloud MIE testing device (Kühner MIKE3). The MIKE3 device contains a cup to hold dust material, a mushroom-shaped nozzle to disperse dust with a burst of compressed air (7-bar pressure), a vertical glass tube (1.2-L volume) to constrain the flow, and a pair of tungsten electrodes to generate a spark discharge. To deliver the spark energies required for this work (30 mJ for niacin and 300 mJ for aluminum), the MIKE3 device employed a moving-electrode discharge circuit. In this arrangement, the moving electrode is first brought away from the stationary electrode during the charging period to avoid premature breakdown of the air. The moving electrode is then pneumatically advanced to the preset 6-mm electrode gap position such that the spark discharge occurs at the correct time during the dispersion event. A nominal ignition delay of 120 ms was selected for this work to match the typical MIE testing procedure. However, the actual discharge time varied for each run, and an effective delay of 125–130 ms was typically observed before ignition.

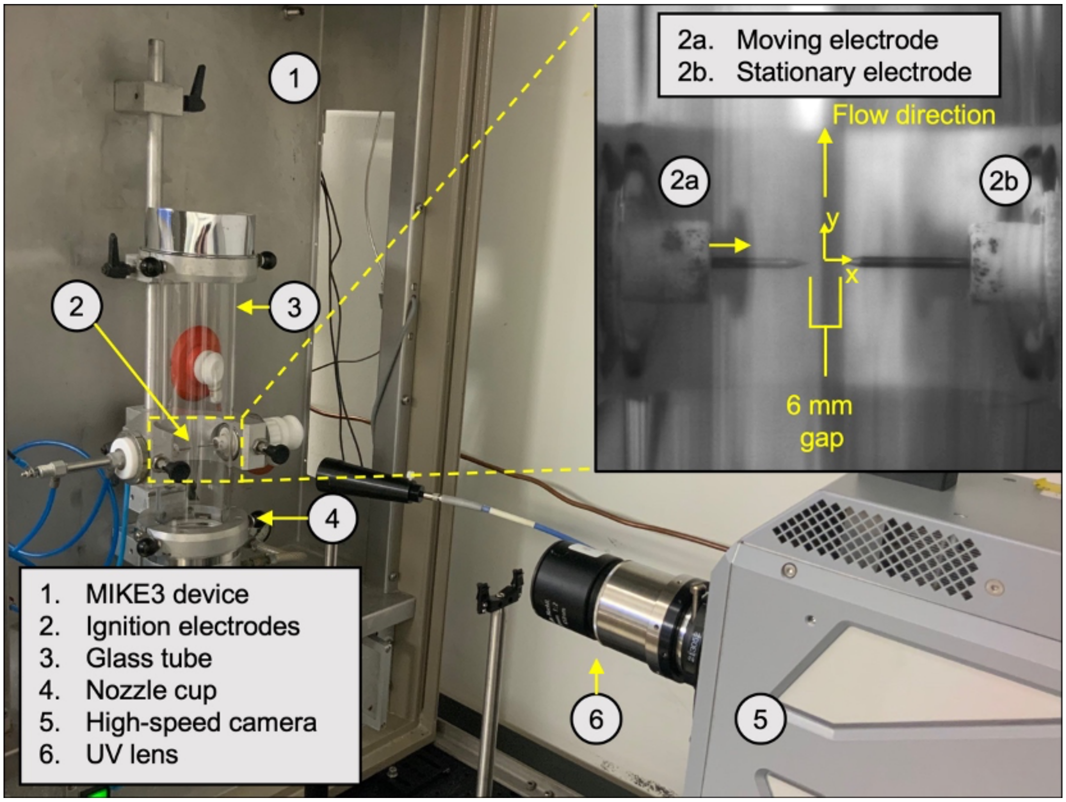

Figure 5.1: Experimental apparatus. The inset on the top right shows the specific region of interest for this study. Reprinted from [108].

The resulting dust flame was imaged with a high-speed camera (Photron FASTCAM SA-Z, 1024 × 1024 pixels, 12-bit monochrome sensor) fitted with an ultraviolet-sensitive (UV) lens (Bernhard Halle Nachfolger, 100-mm focal length, f:2). The UV lens is optimized (achromatic) for collection from 195–450 nm, but also transmits light from the visible and near-infrared spectral regions. The MIKE3 device and the high-speed camera were synchronized with a digital delay generator (Princeton Instruments DG645) via a 5-volt trigger signal from the solenoid valve that actuates the burst of air inside the MIKE3 device. A calibration image of the 6-mm electrode gap (set with a spacer block) and a ruler were used to estimate an effective pixel size of 81.6 μm/pix and an experimental field-of-view area of 83.6 × 83.6 mm^2.

5.2.2 Dust Sample Preparation and Characterization

While standard MIE tests accommodate both "go" and "no-go" ignition results, the testing conditions and dust samples used for this work were carefully selected and prepared to ensure reliable ignition. Niacin ($C_6H_5NO_2$, 1.47-g/cm^3 density, Lonza) and aluminum (Al, 2.7-g/cm^3 density, Sigma-Aldrich) powder samples were selected for this work. Firstly, a sufficiently large spark energy of 30 mJ and 300 mJ was chosen, respectively, to ignite the niacin and aluminum dust clouds. To further improve ignition probability and reduce moisture-induced agglomeration, the dust samples were sieved (63 μm or U.S. standard 230 mesh), dried in a nitrogen-purged oven (50–60 °C for 4 hours), and stored in a desiccator prior to testing. This sample preparation procedure is consistent with the ASTM standard, which recommends testing the finest and driest materials that may be found inside the process or facility of interest (i.e., the most hazardous materials).

A 600-mg dust loading, which represents a typical starting point for dust cloud MIE testing [11], was selected for both samples in this work. Assuming the dispersed dust cloud occupies the entire 1.2-L volume of the glass tube, the 600-mg dust loading corresponds to a mass concentration of 500 g/m^3. Assuming complete combustion with air [10], this mass concentration corresponds to a nominal equivalence ratio ϕ = 2.9 for niacin and ϕ = 1.6 for aluminum.

A laser diffraction particle size analyzer (Beckman Coulter LS 13 320) was also used to conduct an ex-situ characterization of the niacin and aluminum powder samples. The resulting particle

Table 5.1: Particle size data for the niacin and aluminum samples. Reprinted from [108].

Description [unit]	Niacin Sample	Aluminum Sample
d_{10} [µm]	5.5	9.2
d_{50} [µm]	18.7	19.5
d_{90} [µm]	50.6	39.0
polydispersity, σ_D	2.4	1.5
D(3,2) [µm]	8.2	16.5
Specific surface area [cm^2/g]	4971	1347

size data, summarized in Table 5.1, includes the 10th, 50th, and 90th volume percentile diameters denoted as d_{10}, d_{50}, and d_{90}, the polydispersity σ_D, which is calculated with $\sigma_D = (d_{90} - d_{10})/d_{50}$, the Sauter mean diameter denoted as D(3,2), and the specific surface area. The size data show that the samples have similar median values, although the niacin size distribution is broader than that of the aluminum sample. The aluminum sample also has a smaller specific surface area than the niacin sample since the quantity is inversely proportional to the material density and the Sauter mean diameter.

5.2.3 High-Speed Imaging Configurations

Three high-speed imaging configurations were used to study the early flame kernel development of niacin dust flames in different spectral regions. The frame rate, shutter time, and external filtering options were selected so the flame kernel could be imaged with sufficient resolution and signal levels over the 10-ms period. The first imaging configuration collected the broadband flame emission (4 kHz, 200 µs, neutral density filter OD 0.6) over the entire sensitivity range of the high-speed camera. For the second imaging configuration, OH* chemiluminescence signals were selectively detected by attaching a narrow bandpass filter centered at 315 nm to the UV lens (4 kHz, 200 µs, Semrock FF01-315/15-50). For the third imaging configuration, CH* chemiluminescence signals were selectively detected by attaching a narrow bandpass filter centered at 434 nm to the UV lens (1 kHz, 800 µs, Semrock FF01-434/17-50). Only a broadband imaging configuration was implemented for the aluminum sample (4 kHz, 50 µs, neutral density filter OD 2.6) to collect the broadband flame emission over the entire sensitivity range of the high-speed camera.

One imaging configuration was used at a time for this work, and multiple runs were completed to observe general trends arising from the stochastic dust cloud ignition event. Four individual runs were conducted using each of the three imaging configurations for the niacin sample, yielding measurements from $3 \times 4 = 12$ total runs. For the aluminum sample, three individual runs were completed using the single imaging configuration, yielding measurements from $3 \times 1 = 3$ total runs.

Preliminary spectral analysis of the niacin dust flame was conducted with a spectrometer (Ocean Optics HR2000+) and a digital camera. The spectrometer revealed a large broadband signal and emissions in the near-UV region that likely correspond to chemiluminescence from OH* and CH* radicals and light from the ionized air in the electrode gap. However, the spectrometer did not have the time resolution to capture the temporal evolution of the dust flame spectrum. Nevertheless, high-speed color images from the digital camera corroborated the spectrometer data and revealed that the flame kernel had a blue-purple hue for the first 10–15 ms after the spark, after which a more prominent orange color appeared.

5.2.4 Image Processing and Data Analysis

The raw images from each experiment were processed with a Python script to detect the flame kernel and measure its features across subsequent frames. A median filter was first applied to a given raw image to remove noise while preserving important features like the flame edge. Next, the flame kernel was separated from the background using an automatic intensity-thresholding algorithm. For this work, the automated algorithms (Otsu's or Yen's method) implemented in the scikit-image Python library [103] were found to be a suitable starting point for detecting the flame kernel. After a second noise removal step, the area of the flame kernel and the position of its centroid were measured. In cases where multiple kernels were detected, the size-weighted average centroid position was measured instead. The results of the automatic thresholding process were then reviewed and manually adjusted if the flame kernel was not accurately identified. Adjustments were typically needed when the dynamic range of the scene suddenly changed, usually from rapid flame kernel intensity fluctuations. Once the flame kernel was detected and reviewed, the equivalent area diameter d_{eq} was calculated from the projected flame area A with:

$$d_{\text{eq}} = \sqrt{\frac{4A}{\pi}} \tag{5.1}$$

Once the flame kernel velocity components v_x and v_y were determined from the flame kernel centroid position, the transverse velocity $v_{x\text{-}y}$ was calculated with:

$$v_{x\text{-}y} = \sqrt{v_x^2 + v_y^2} \tag{5.2}$$

Finally, the pixel measurements were converted to length units and shifted so that the horizontal axis aligned with the electrode height and the vertical axis aligned with the center of the electrode gap (see Fig. 5.1. Thus, the flame kernel motion relative to the central electrode position could be measured over the 10-ms period. The flexible detection and tracking algorithm described above, combined with the completion of multiple experimental repetitions for each imaging configuration and sample, enable a wide range of possible ignition behaviors to be measured. General trends can then be determined to characterize the stochastic ignition process.

5.3 Chemiluminescence Results and Discussion

5.3.1 Niacin Flame Kernel Measurements

A sample set of processed niacin flame kernel images can be seen in Fig. 5.2. The broadband (top row), OH* (middle row), and CH* (bottom row) emission images show the developing flame kernel at five different time steps (2–10 ms). A green line is drawn around the detected flame kernel, and its centroid is marked with a white dot to reveal the evolving flame kernel trajectory. Green lines are also drawn on the edges of each image to indicate the position of the tube walls. Finally, the last image in each row applies a 1.33× zoom so that the final shape and trajectory of the flame kernel can be examined in greater detail.

All three imaging configurations show that the flame kernel forms at a central position near the spark gap. The flame kernel then moves away from its initial position and rapidly grows into

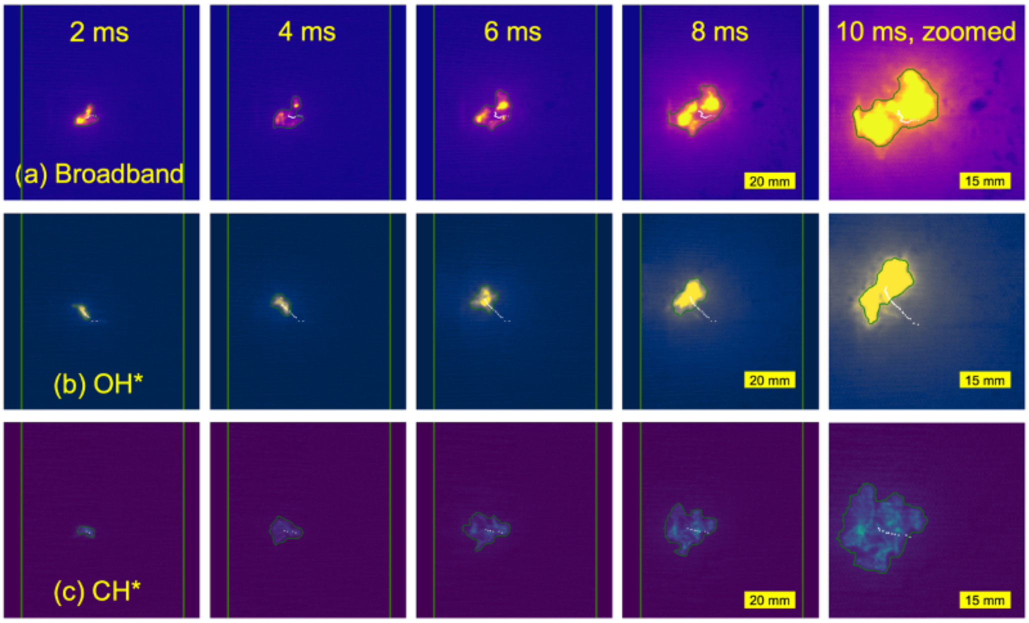

Figure 5.2: A sample set of niacin flame kernel images from (a) broadband, (b) OH*, and (c) CH* recordings. Each row represents an individual run (with a fresh batch of dust) from the given imaging configuration, and the last image in each row applies a 1.33× zoom. The vertical green lines represent the tube walls. Reprinted from [108].

an irregular plume shape. The flame kernels shown in Fig. 5.2 all travel upward through the tube, likely due to buoyancy effects and the residual velocity of the dust cloud caused by the burst of compressed air. However, downward-traveling flame kernels were also observed, which suggests that the initial motion of the flame kernel may be influenced by other factors such as the local distribution of fuel near the electrodes and the shape of the spark discharge path. The flame kernels also show an apparent motion towards the moving-electrode side of the tube. Possible explanations for this asymmetrical behavior will be explored further by analyzing the quantitative position and velocity data.

The flame kernels from the three imaging configurations show a mostly continuous flame zone. However, the broadband images also show evidence of discrete burning clusters of particles in the earlier times steps. These features are less prominent or absent in the OH* and CH* images, indicating that these emissions arise from particle incandescence. The CH* images also show non-luminous regions throughout the flame kernel, demonstrating non-uniform flame kernel structure development. These observations are consistent with other studies that have investigated the flame propagation mechanisms for non-charring organic dust materials [97, 104]. These studies demonstrated that burning dust clouds might develop continuous (kinetics-controlled regime) or discrete (devolatilization-controlled regime) reaction zone structures depending on properties like the particle size distribution and the fuel volatility.

The quantitative size measurements calculated with Eq. 5.1 are extracted from the high-speed videos and plotted in Fig. 5.3 to show the growth trends of the niacin flame kernel. Overall, data from all three imaging configurations are similar and show that over the 10-ms period, the flame kernel diameter grows to approximately 3× its original size. The broadband and OH* kernels have initial dimensions of 5–10 mm, while the CH* kernels have slightly smaller initial sizes of 3–5 mm. Fig. 5.3 also shows that the size of the flame kernel can decrease from its initial size before starting to grow again. Residual light emission from the spark discharge may contribute to the initial size of the flame kernel. This initial behavior may also indicate that the flame kernel shrinks to a critical size during the earliest moments of the combustion process. The initial shrinkage of the flame kernel likely explains the smaller initial CH* kernel sizes, which are measured at a slightly later time than the first broadband and OH* measurement because of the slower frame rate.

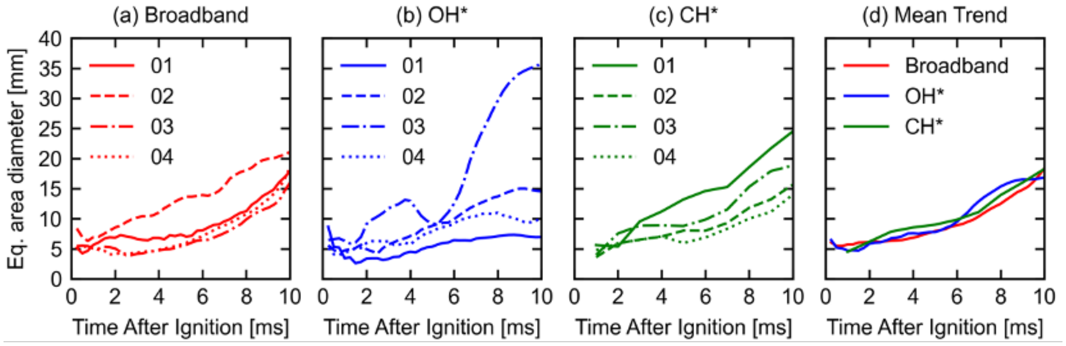

Figure 5.3: Temporal evolution of the niacin flame kernel size showing the (a) broadband, (b) OH*, (c) CH*, and (d) mean trends. The legend entries 01, 02, 03, and 04 correspond to the four individual runs completed for each imaging configuration. Reprinted from [108].

One of the OH* curves (run 3) seen in Fig. 5.3 (b) also shows a unique phenomenon, whereby a decrease in size that starts at approximately 4 ms is followed by a second increasing trend, resulting in the flame kernel growing to 35 mm in size. The high-speed video for this particular run showed that the temporary decrease in size corresponded to a smaller but more intense flame kernel growing out of the first. Examining the mean trend lines in Fig. 5.3 (d), the flame kernel size data from each imaging configuration essentially overlap. This observation suggests a well-defined reaction zone where burning particles and excited-state radicals are tightly confined.

Next, the quantitative position and velocity measurements are extracted from the high-speed videos and plotted in Fig. 5.4 to show the motion trends of the niacin flame kernel. The x-position data (top row) corroborate the observations from Fig. 5.2 and establish a prominent trend toward the moving-electrode side of the tube, with the flame kernels forming to the left of the spark gap centerline. This asymmetry may be caused by sudden changes in the flow field as the moving electrode closes the spark gap. Additionally, the ionization of the spark gap begins to occur slightly before the moving electrode reaches its final position [105], which results in asymmetric spark formation with respect to the tube centerline, and may result in a slight asymmetry in heating that favors the moving electrode side. The influence of the moving electrode on the observed asymmetry in flame kernel development may be further investigated by implementing the static electrode arrangement of the MIKE3 device, which is used to generate lower ignition energies (<10 mJ). Despite this, the low-energy configuration was not included in this study, as it was prone to discharge misfires due to charge loss. Finally, the moving electrode arrangement may be implemented with an inert dust material and investigated using high-speed imaging or other techniques like particle image velocimetry (PIV) to investigate the influence of the electrode movement and spark-generated shock waves on the dust cloud ignition or non-ignition.

From Fig. 5.2, it can also be seen that most of the flame kernels move away from the spark gap centerline, although some cases show the flame kernel centroid returning to a central position. The mean trend for the x-position shows that the OH* and CH* kernels travel approximately 3 mm further than the broadband kernel.

The y-position data (middle row) show that the flame kernels most often form below the elec-

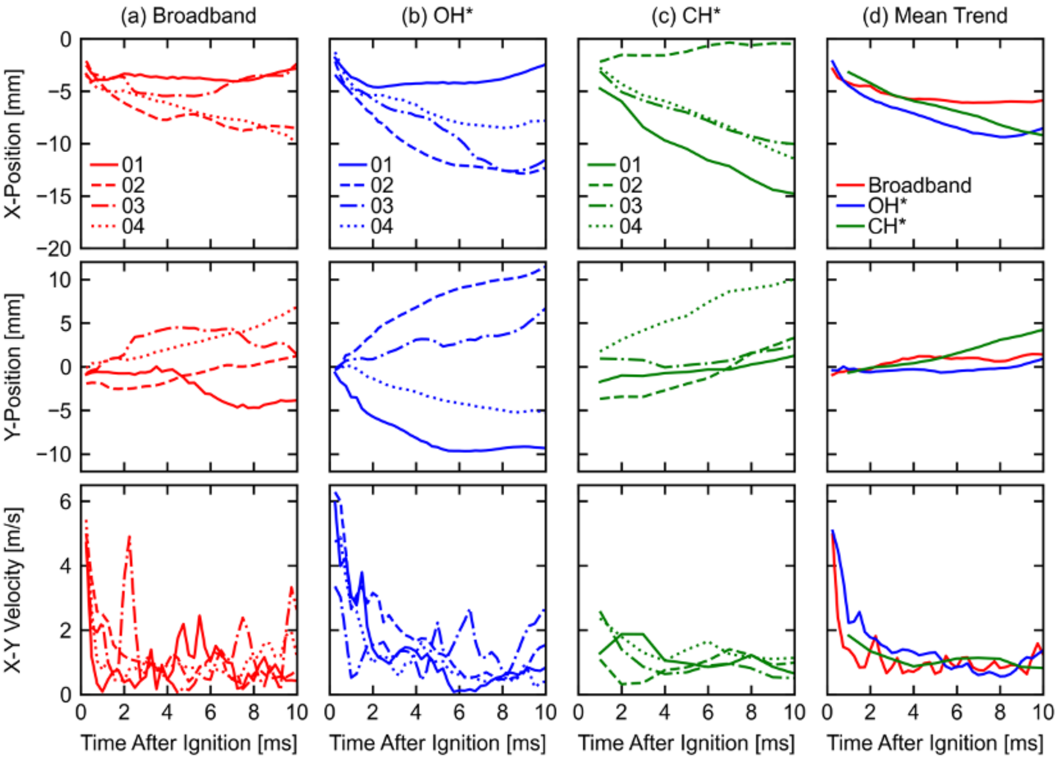

Figure 5.4: Temporal evolution of the niacin flame kernel position and velocity showing the (a) broadband, (b) OH*, (c) CH*, and (d) mean trends. Reprinted from [108].

trode height. A clear symmetric trend is also seen with the OH* data, confirming that the flame kernel can oppose the bulk flow motion and buoyancy effects. A similar trend is also seen with the broadband data. For the CH* data, only an upward trend in motion is seen. The subtle difference in trends highlights the stochastic nature of the dust cloud ignition process. The mean trends show that the CH* kernels travel approximately 3 mm further than the broadband and OH* kernels.

The x-y velocity data (bottom row) show that the flame kernel develops with a large initial velocity that gradually decreases. The data from individual runs also show large fluctuations, which could be caused by the rapidly shifting position of the flame kernel centroid due to changes in the flame kernel geometry. Finally, an analysis of the mean trend of the individual curves shows a decrease from 5 m/s to approximately 1m/s.

5.3.2 *Aluminum Flame Kernel Measurements*

A sample set of processed aluminum flame kernel images can be seen in Fig. 5.5. Similar to the niacin results, the aluminum flame kernel forms at a central position near the electrode gap and gradually grows in size. However, the aluminum flame kernel appears to grow slower than the niacin flame kernels and is therefore much smaller by the end of the 10-ms period. The interior structure of the flame kernel remains unresolved due to the intense emission from the combustion. Compared to the niacin flame kernels, the aluminum flame kernel in Fig. 5.5 also appears more spherical.

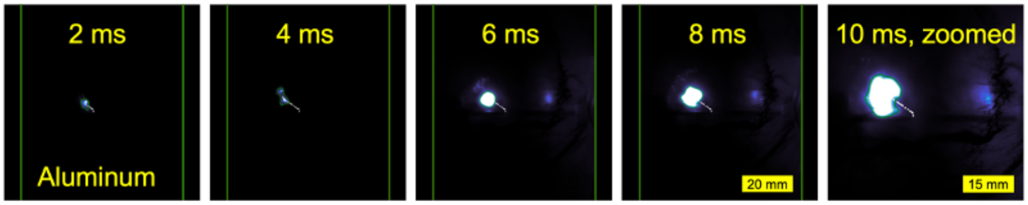

Figure 5.5: A sample set of aluminum flame kernel images recorded using broadband imaging. The last image applies a 1.33× zoom, and the vertical green lines represent the tube walls. Reprinted from [108].

Discrete burning particles were also observed near the edges of the aluminum flame kernel, which was not observed in the niacin videos. These discrete burning particles, which can be seen in Fig. 5.6 (a), were ejected from the interior of the intense luminous reaction zone shortly after ignition. While many of the aluminum particles quickly cooled down, a nearby group of particles was also able to form a secondary flame kernel. While it is difficult to ascertain the phase of the burning fuel or combustion products, filament structures were sometimes observed on the inner wall of the tube wall and the electrode surfaces, as seen in Fig. 5.6 (b). These structures suggest the presence of molten material in the reaction zone, and thus a mixed-phase combustion process, which has also been observed in other aluminum combustion experiments [94, 106].

Next, the quantitative size, position, and velocity measurements are extracted from the high-speed videos and plotted in Fig. 5.7 to highlight the growth and motion trends of the aluminum flame kernel. The size data show that the flame kernels grow from 7 mm to 11 mm, which confirms

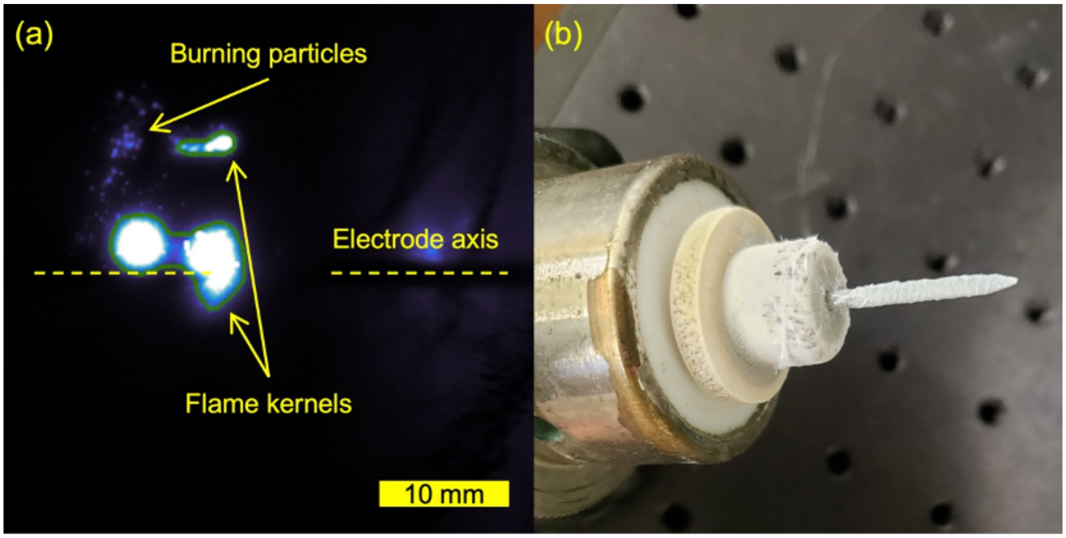

Figure 5.6: (a) Sample image showing discrete burning aluminum particles and a secondary flame kernel ejected from the primary flame kernel. (b) Image of filament material on the electrode surface. Reprinted from [108].

a slower growth trend when compared to the niacin flame kernels. However, one of the cases (run 2) demonstrated rapid growth to 15 mm before intense reflections completely degraded the quality of the flame kernel detection procedure.

The x-position data show that the aluminum flame kernels form 3 mm to the left of the spark gap centerline and travel further in the same direction. The same trend toward the moving-electrode side of the tube is therefore seen between the aluminum and niacin samples. The y-position data show that the flame kernels form at or slightly below the electrode height and travel 5 mm upward through the tube. Finally, the x-y velocity data show that the aluminum flame kernels have an initial velocity that gradually decreases to approximately 1 m/s. The lower initial velocity of $\sim$3 m/s may be caused by the higher density of the aluminum sample.

5.4 Chemiluminescence Conclusions

In this study, the flame kernels arising from spark-ignited niacin and aluminum dust clouds were analyzed using high-speed and species-specific (OH* and CH*) imaging. High-speed videos were processed with an intensity thresholding algorithm to detect and track the developing flame

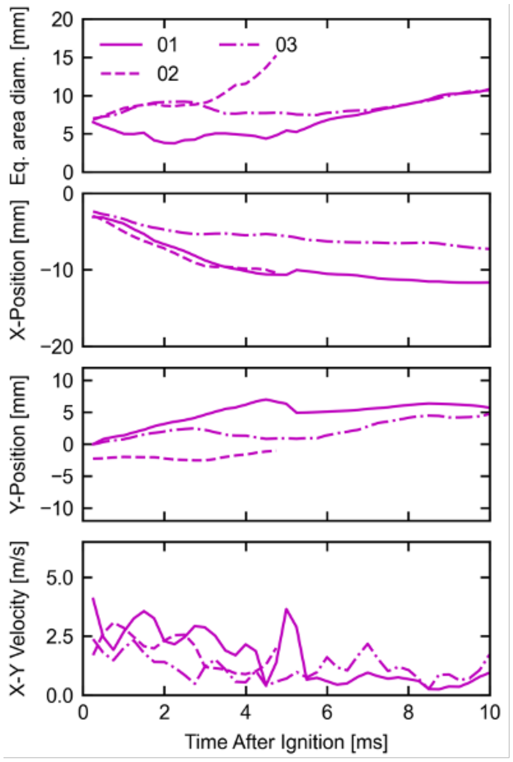

Figure 5.7: Temporal evolution of the aluminum flame kernel size, position, and velocity. Reprinted from [108].

kernel after ignition. Quantitative size, position, and velocity data were extracted from the flame kernel images to investigate growth and motion trends. The niacin flame kernels showed a continuous and non-uniform reaction zone comprising burning particle clusters and excited-state species. The niacin flame kernels grew from 5 mm to 17 mm and traveled away from the central electrode region with an initial velocity of 5 m/s.

The aluminum flame kernels showed a bright reaction zone with an unresolved internal structure. However, discrete burning particles were also observed near the flame kernel boundary, and evidence of molten material was also discovered in the tube after some experiments. The aluminum flame kernels grew from 7 mm to 10 mm and traveled away from the central electrode region with an initial velocity of 3 m/s. The niacin and aluminum flame kernels traveled away from the central spark gap and slowed down to 1 m/s.

Knowledge of the flame kernel development is essential to understanding the dust cloud ignition process. Accurately identifying the flame kernel boundary was challenging due to the extensive and fluctuating dynamic range of the dust cloud ignition event. However, the results from multiple runs demonstrated good agreement when comparing the mean trends for each imaging configuration. Therefore, these findings can provide critical insights into developing dust explosion suppression technologies. In follow-on investigations, the OH* and CH* species-specific analysis can be applied to other organic dust materials to compare their flame kernel development trends. Future studies could also incorporate chemiluminescence from other species such as oxides of aluminum (AlO) to establish a substance-specific understanding of spark-ignited dust clouds. Finally, while this work focused on the early growth and motion of the flame kernel, the analysis may be extended in future studies to explore the flame propagation at later times and the overall combustion process. However, high-dynamic range imaging strategies must be developed to accommodate the rapidly increasing intensity from the burning dust cloud from the start to the end.

6. OH-PLIF IMAGING FOR DUST CLOUD COMBUSTION DIAGNOSTICS

6.1 OH-PLIF Introduction

Dust fires and explosions present severe and often unrecognized risks to a wide range of process industries [1, 3]. As such, dust ignitability and explosibility properties must be measured to identify hazards in industrial facilities and implement appropriate safeguards [5, 6]. One crucial hazard parameter is the minimum ignition energy (MIE), which is defined as the lowest energy required to ignite the combustible dust-air mixture with a high-voltage spark discharge. Reliable dust cloud MIE measurements are made with testing equipment like the MIKE3 device according to standard methods such as ASTM E2019 [11]. The MIKE3 device, while immensely important for industrial safety testing, has also been used to study fundamental aspects of dust cloud ignitability. Ignition studies using the MIKE3 device or similar vertical explosion tube setups have demonstrated that dust cloud MIE values are influenced by sample properties such as the particle size distribution [22, 23], polydispersity [25], and morphology [27, 28]. Aspects of the testing environment, such as the spark discharge method [29, 31] and the oxidizer composition [33, 34] can also lead to varied MIE results. While these previous investigations have clearly demonstrated the complex dependencies of the MIE, there is still a considerable lack of evidence for explaining the mechanisms that produce these dependencies.

To complement conventional MIE data, which is a single-point measurement for a given dust material, advanced methods have also been developed to resolve the underlying physics and chemistry of dust cloud combustion. Recent experiments in vertical explosion tube setups have leveraged cameras, lasers, and other sensors to collect high-resolution data from dust clouds. For example, digital in-line holography (DIH) was used in a series of experiments to collect quantitative particle data from dispersed dust clouds in the MIKE3 device prior to ignition [79–81]. These investigations demonstrated that dust sample properties such as particle size, density, and morphology could influence the particle concentrations and velocities that were measured near the ignition electrodes. Follow on studies have combined DIH with particle image velocimetry (PIV) to enable micro-scale particle and macro-scale flow measurements in the MIKE3 explosion tube [93]. The data from many repeated experiments were used to statistically characterize the particle and flow behavior that arose in the ignition zone.

In addition to these dust cloud dispersion investigations, high-speed flame photography and pyrometry experiments have further elucidated the combustion behavior of burning dust clouds, yielding flame propagation and flame temperature measurements from a variety of dust materials [91, 94, 95]. Spectrally-filtered imaging techniques, such as chemiluminescence imaging, have also been implemented [96, 97, 107] to obtain species-specific data from the dust cloud combustion reaction zone. In a recent study, multiple chemiluminescence-imaging configurations were combined to detect excited-state hydroxyl (OH*) and methylidyne (CH*) radicals in niacin dust flames, which enabled the analysis of the flame structure and propagation with improved specificity [108].

It is clear that the number and sophistication of optical techniques implemented for dust explosion measurements continues to increase. Despite this encouraging trend, the implementation of laser-based techniques for dust flame diagnostics is still an underdeveloped research area. For example, within the broader combustion diagnostics community, planar laser-induced fluorescence (PLIF) has been proven as an indispensable tool for obtaining measurements of intermediate species such as the hydroxyl radical (OH) [62], which is a key constituent in hydrogen and hydrocarbon combustion reactions. Importantly, OH is a primary marker of the reaction zone and also indicates the heat release process in flames [109].

In the PLIF technique, targeted molecules are excited to a higher energy state by the absorption of photons in a pulsed laser sheet, which is tuned to a specific electronic transition of that molecule. These molecules will then return to the initial energy state and emit fluorescence photons that can be spectrally separated and detected. This fluorescence signal, which can be collected with a suitable camera and lens system, is proportional to the number of molecules in the original ground state. Thus, OH-PLIF imaging studies enable the collection of spatially and temporally resolved OH concentration data for the analysis of the flame structure and flame propagation behavior in burning dust cloud environments. Despite these beneficial capabilities, the implementation of OH-PLIF for dust flame diagnostics remains largely unexplored, due to the increased complexity compared to passive diagnostics and the harsh dust cloud environment. Implementation of laser-based diagnostics in the MIKE3 device is also challenging due to the geometry of the setup and the need to synchronize measurements with the unsteady explosion process. Thus, the aim of this study is to expand the current knowledge of dust cloud combustion through the application of OH-PLIF in the MIKE3 device.

In the present study, OH-PLIF imaging is implemented to visualize and measure the flame structure of burning niacin dust clouds in the MIKE3 device. Qualitative morphology categories are identified and quantitative area and two-dimensional (2D) curvature measurements are extracted from the detected flame regions. Finally, the average OH distribution in the ignition zone is assessed. Details of the experimental apparatus, data collection and analysis procedure, and the sample preparation process are described in detail in Section 6.2. The results obtained from this experiment are reported and discussed in Section 6.3. Finally, the major conclusions of this work and areas for future study are summarized in Section 6.4.

6.2 OH-PLIF Experimental

6.2.1 Experimental Apparatus

The experimental apparatus used for this work is shown in Fig. 6.1. Dust clouds were generated and ignited with a dust cloud MIE testing device (Kühner MIKE3). For standard MIE tests, dust material is loaded into a cup at the base of a vertical explosion tube (1.2-L volume). Once the test is initiated, a mushroom-shaped nozzle in the cup disperses the dust sample with a burst of compressed dry air (7-bar pressure). Two tungsten electrodes then generate a spark discharge at a predetermined energy level and time delay with respect to the dispersion. In this work, ten niacin dust samples were dispersed and ignited in the MIKE3 device with a nominal ignition delay of 120 ms. This delay value is commonly selected to obtain data when the turbulence of the dust cloud is reduced, although the optimal delay time for determining the MIE will depend on the specific dust sample being tested. To reliably ignite the ten niacin dust samples, an ignition energy of 1000 mJ was selected. For this spark energy, the MIKE3 device employs a moving-electrode discharge circuit. In this arrangement, the moving electrode is brought away from its home position prior to the dispersion to avoid premature breakdown of the air in the spark gap due to the large charging voltage. The moving electrode is then advanced back to the home position such that the spark discharge occurs at the appropriate time. The actual discharge time will vary for each experimental run, with an effective delay of 125–130 ms typically observed.

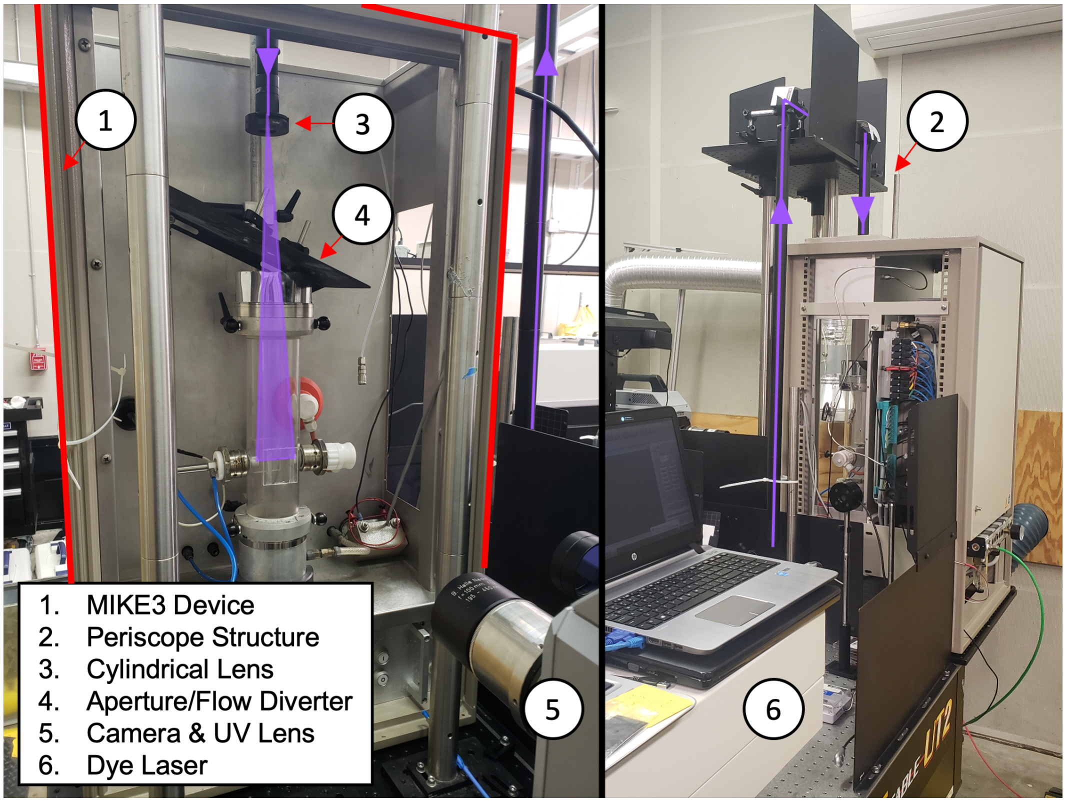

Figure 6.1: Photograph of the experimental apparatus. Left: front-side view. Right: back side view.

For OH-PLIF imaging studies, laser pulses at 282.750 nm were used to excite the Q1(5) line of the OH $A^2\Sigma^+$–$X^2\Pi$ (1,0) band, followed by fluorescence-emission detection in the (0,0) and (0,1) bands. The ultraviolet (UV) beam was generated by frequency doubling the 565.50 nm output beam from a tunable dye laser (Continuum Vista) with a beta barium borate (BBO) crystal (Type I SHG, P-coating). The dye laser used a lasing mixture of Rhodamine 590 and methanol and was pumped by the 532 nm output beam of a 10 Hz nanosecond Nd:YAG laser (Continuum Powerlite 8000). As seen in Fig. 6.1, the UV laser beam was guided above the MIKE3 device using a periscope structure and formed into a thin laser sheet using a spherical lens (Thorlabs LA6009, f = +500 mm) and cylindrical lens (Thorlabs LK4349RM, f = 50 mm) combination. The pulse energy after the sheet-forming optics was fixed and measured to be $\sim$2.2 mJ/pulse. A metal plate, with an aperture opening covered by a quartz window, was also fitted above the explosion tube. The metal plate was used to pass the central section of the beam sheet to the probe volume and divert the flow of combustion products away from the sheet forming optics. The UV laser sheet was passed through the center of the explosion tube, with the sheet plane coincident with the electrode axis and perpendicular to the imaging system.

As can be seen in Fig. 6.1, a modified explosion tube, fitted with fused-silica windows, was used instead of the standard glass tube. This modified explosion tube, which was used in previous DIH studies of dust clouds [80, 81, 93], has the same geometry as the standard tube, but also enables improved UV radiation transmission. The subsequent OH fluorescence emissions from the laser excited niacin dust flames were then collected with an intensified charge-coupled device (ICCD) camera (Princeton Instruments PI-Max4 1024i, 1024×1024 pixels, 16-bit monochrome sensor) fitted with a UV-sensitive lens (Bernhard Halle Nachfolger, 100-mm focal length, f:2). A 315 nm bandpass filter (Semrock FF01 315/15-50) was also attached to the UV lens to selectively transmit OH fluorescence while blocking other sources of interference such as Raleigh and Mie scattering. A calibration image was used to estimate an effective pixel size of approximately 50.0 μm/pix and a full image area of approximately 51.2 mm × 51.2 mm. This full image was cropped to yield a final experimental field of view (FOV) area of approximately 27.0 mm (width) × 46.0 mm (height), which corresponds to the central ignition region that is viewable through the windows in the tube. A schematic of the OH-PLIF experimental apparatus and photographs of the experimental FOV can be seen in Fig. 6.2.

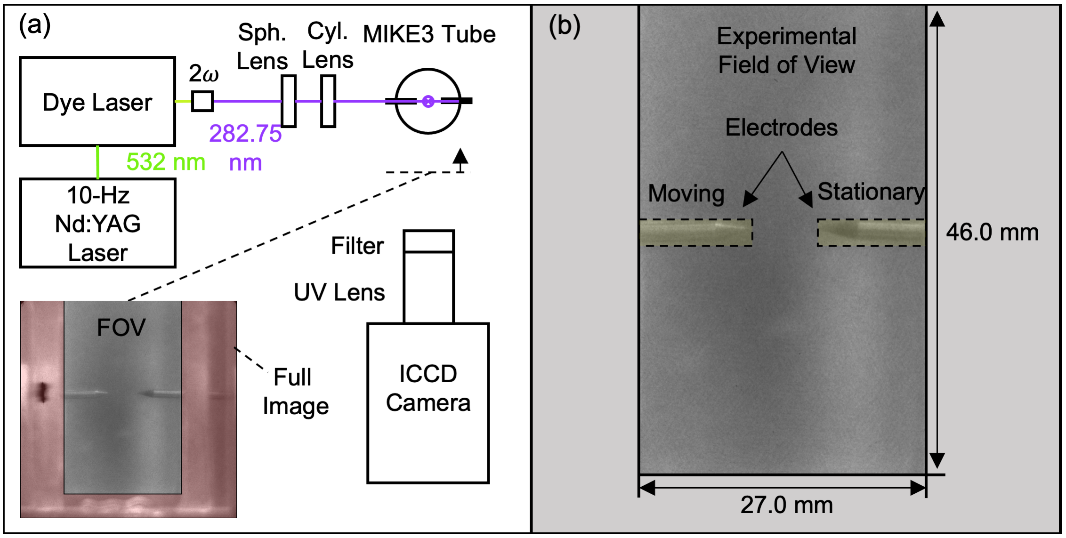

Figure 6.2: (a) Schematic of the OH-PLIF experimental apparatus. (b) Detailed view of the experimental field of view.

6.2.2 Data Collection

The UV pulses from the laser system and recordings with the ICCD camera were initiated by the dispersion from the MIKE3 device and synchronized by a digital delay generator (Princeton Instruments DG645). OH-PLIF images were obtained several milliseconds after the spark discharge to visualize and measure the niacin dust flames after the intense spark emission had subsided and the initial flame kernel had sufficient time to develop. In this work, a 10-ns gate for each image recording was implemented to selectively collect the OH-fluorescence signal. Since the time delay between the burst of compressed air and the discharge of the spark had an uncertainty on the order of milliseconds, a photodiode (Thorlabs DET210) was used to precisely measure the time delay between the rising edge of the spark emission signal and the rising edge of the ICCD camera recording gate. This time difference was successfully measured for nine out of ten experiments, with one run failing to produce a suitable spark emission signal. A mean time delay with expanded uncertainty (95% confidence level, coverage factor = 2.306) of 8.41 ms ± 0.71 ms for the OH-PLIF image recordings was measured.

The ICCD camera was also operated in the Dual Image Feature (DIF) mode such that a secondary image was obtained 5 μs after the recording of the OH-PLIF image. This secondary image was captured with the same 10-ns gate as the OH-PLIF image, but without a corresponding laser pulse. Using previously measured velocities in the tube [93, 108], the displacement of features between the sequentially-captured images was estimated to not exceed $\sim$15 μm, which is less than the pixel size of the imaging system. Thus, the secondary recording provided a near-instantaneous background image to remove interfering OH* chemiluminescence signals, as well as other broadband emission signals that transmitted through the bandpass filter.

6.2.3 Data Reduction and Analysis

Following the completion of the ten niacin ignition experiments, a Hencken burner was installed and translated across the beam sheet to characterize the laser intensity distribution in the experimental FOV. From this analysis, the beam sheet profile was observed to be nearly Gaussian, with the edges having intensities of $\sim$18% of the maximum value at the height of the electrodes. Since the dust cloud stochastically modified the intensity distribution of the beam sheet for each of the ten experiments, no intensity correction was applied to the data obtained in this work. Thus, the raw OH-PLIF images were only corrected by subtracting the secondary OH* image to account for OH* chemiluminescence and other broadband emission interferences. The noise-subtracted OH-PLIF images were then processed to identify the flame regions with sufficiently large OH concentrations. A median filtering operation and Otsu's method for automatic image thresholding were found to be suitable for accurately separating the flame signal from the background. The signal-to-noise ratio (SNR) for each image was then calculated with:

$$\text{SNR} = \frac{\mu_S - \mu_B}{\sigma_B} \tag{6.1}$$

Here μ_S is the mean pixel intensity value inside the segmented flame region, while μ_B and σ_B are the pixel intensity mean and standard deviation values inside the background region (the complement of the flame region), respectively. For these SNR calculations, the electrode areas were removed from the signal region to prevent the inclusion of reflected fluorescence emissions from the electrode surfaces.

To further analyze the niacin dust flame structure, the area of the flame region was measured, and the pixel coordinates of the corresponding flame front contour were extracted. The contour was subsequently parametrized and interpolated, yielding coordinate functions $x(s)$, and $y(s)$ for a given point, s, along the flame front path. The local 2D flame curvature [110] was then calculated with:

$$H = \frac{x'y'' - y'x''}{(x'^2 + y'^2)^{3/2}} \tag{6.2}$$

Here the prime and double prime symbols represent the first and second derivative with respect to the flame path parameter s, respectively. The value of H is signed, with positive curvature values corresponding to regions that are convex to the unburnt reactants in the background region. Likewise, negative curvature values correspond to regions that are convex to the burnt products in the flame region. In this work, a smoothed cubic spline was used to approximate the flame front contour since it was largely insensitive to the prescribed interpolation spacing and reduced spurious curvature calculations arising from the initially extracted position of the flame front contour in pixel coordinates.

6.2.4 Dust Sample Selection, Preparation, and Characterization

A niacin (pyradine-3-carboxylic acid or nicotinic acid, $C_6H_5NO_2$, 1.47-g/cm^3 density, supplier: Lonza) powder sample was selected for this work as an industrially-relevant organic dust material. This particular powder sample was used in the 2017 international calibration-round-robin test for the MIKE3 device (CaRo 17 [102]), and is identical to the dust sample used in a previous flame chemiluminescence imaging study [108]. To further improve the ignition probability in the MIKE3 device and reduce the impact of agglomeration, the dust samples were sieved (63 µm or U.S. standard 230 mesh) prior to testing. While the samples in this work were unable to be dried, this sample preparation procedure is largely consistent with the ASTM E2019 standard [11], which recommends testing the finest and driest (i.e. most hazardous) materials that may be found in a facility.

Preliminary ignition and imaging studies were conducted to determine suitable mass loadings for the OH-PLIF imaging study. Small mass loadings approaching the minimum explosible concentration ($\sim$50 mg) were found to unacceptably reduce ignition probability, resulting in a large proportion of non-ignitions. Conversely, the dust clouds from larger mass loadings ($\sim$300 mg) resulted in severe attenuation of the UV laser beam by the dust cloud along the length of the explosion tube. To balance these considerations, a mass loading of 100 mg was selected for this work. This mass loading corresponds to a nominal mass concentration of $\sim$83.3 g/m^3 assuming an evenly dispersed dust cloud in the explosion tube, and a nominal equivalence ratio ϕ = 0.48 assuming complete combustion with air.

6.3 OH-PLIF Results and Discussion

6.3.1 Flattened-Plume Morphologies

From the ten niacin dust ignitions, ten processed OH-PLIF images were obtained and categorized based on the qualitative morphologies of the observed flame regions. Three processed OH-PLIF images, presenting "flattened-plume" morphologies, are shown in Fig. 6.3. These images are organized by increasing time delay (Δt), and also include the run number, the SNR calculated with Eq. 6.1, and a scale bar. The flame regions in Fig. 6.3 are distinguished by a continuous, but not necessarily uniform, reaction zone and an irregularly-shaped flame front. The majority of the flame signal is concentrated above the electrodes in a single plume that is flattened in the width direction. In Figs. 6.3(a) and 6.3(b), smaller "islands" of flame signal are also observed near the primary flame plume.

In all three cases, the flattened plume extends to nearly the entire width of the experimental FOV, with the vertical position increasing slightly from earlier to later times. This trend suggests that the niacin dust flame will tend to propagate upward through the tube, likely due to the bulk motion of the dust cloud (forced convection) and thermally-induced buoyancy effects (natural convection). This finding is consistent with a previous analysis of the flow field in the MIKE3 device under similar testing conditions [93], which reported a positive-vertical velocity distribution in the ignition zone at the nominal ignition delay of 120 ms. The upward propagation observed in this work is also consistent with a previous time-resolved chemiluminescence-imaging study of niacin ignitions in the MIKE3 device [108]. While this previous study implemented larger mass loadings of 600 mg, irregularly-shaped plumes that travelled upward through the explosion tube were also observed. Since the plumes measured in this work are planar sections of the niacin dust flame, the current study demonstrates the improved capability of OH-PLIF to resolve local flame wrinkling during the unsteady and turbulent combustion process. Such spatially-resolved morphological features are largely inaccessible with line-of-sight techniques such as chemiluminescence imaging.

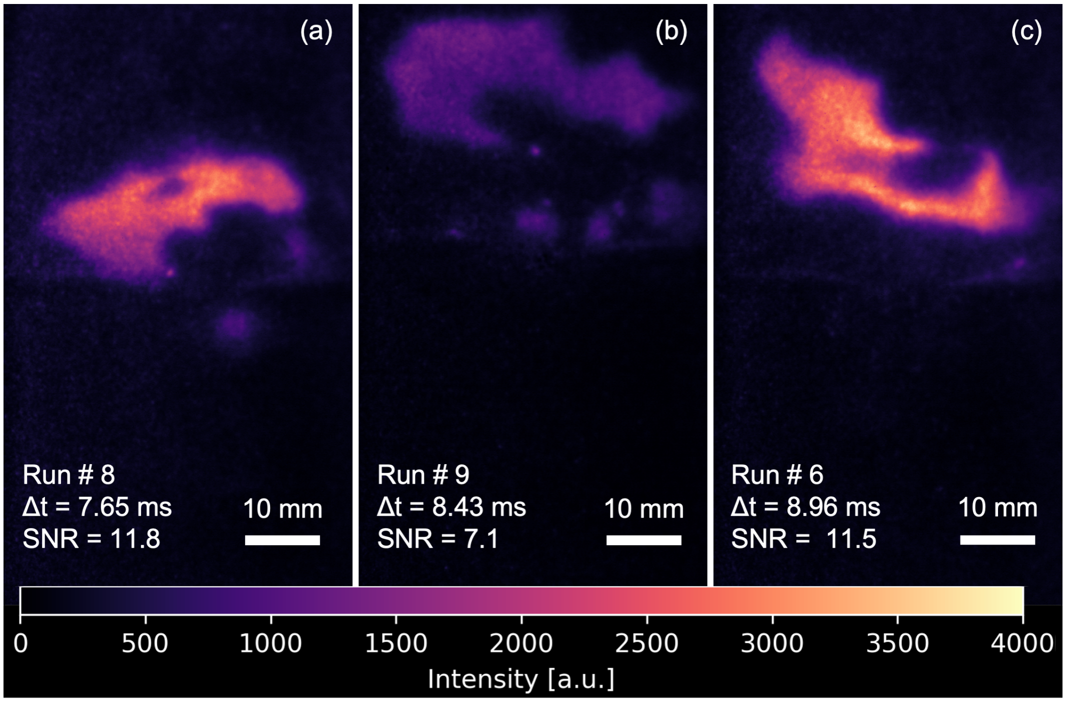

Figure 6.3: Processed OH-PLIF images showing the flattened-plume morphology. The images from (a) run # 8, (b) run # 9, and (c) run # 6 include the time delay (Δt) and the signal-to-noise-ratio (SNR). The scale bars indicate a 10-mm linear distance.

The flame regions in Figs. 6.3(a) and 6.3(c) share similar intensity values between ∼500–4000 counts. By contrast, the flame region in Fig. 6.3(b) shows lower intensity values between ∼200–1500 counts, resulting in a reduced SNR value. For the images in Fig. 6.3, a mean SNR value of 10.1 is calculated, which represents the current best-case SNR for single-shot OH-PLIF imaging in the harsh environment of the burning dust cloud. Further analysis of the spatial distribution of OH in these dust flames is challenging due to the lack of a laser-intensity correction. Despite this, it is likely that the distribution of OH in the reaction zone will be correlated with the spatial distribution of particles in the dust cloud (i.e. the local equivalence ratio). Spatial gradients in the equivalence ratio will be driven by the non-uniformity (polydispersity) of the dust cloud's particle size distribution and inertial particle clustering due to turbulence.

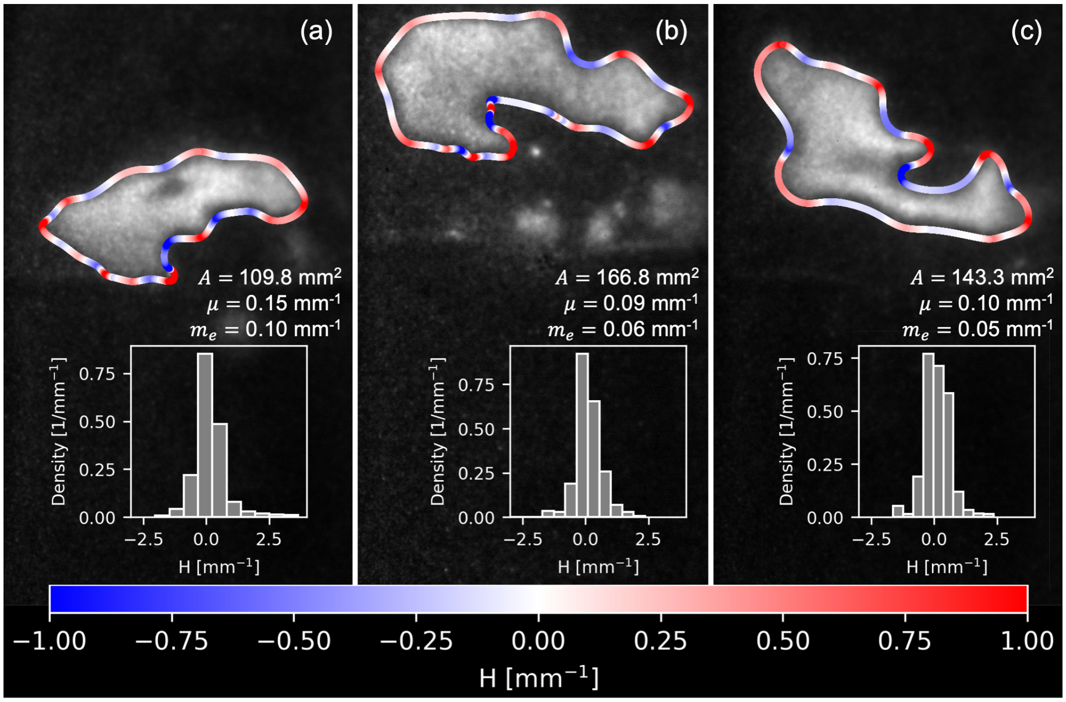

Figure 6.4: Flattened-plume OH-PLIF images showing quantitative morphology measurements. The images from (a) run # 8, (b) run # 9, and (c) run # 6 include the flame front curvature contour, the curvature histogram, the flame area (A), the mean curvature (μ), and the median curvature (m_e).

The quantitative flame area and flame front curvature measurements that were subsequently obtained from the flattened-plume OH-PLIF images are shown in Fig. 6.4. In addition to being the closest to the electrodes, the flame region in Fig. 6.4(a) is also the smallest in the group with a flame area of $\sim$110 mm^2. The flames regions in Figs. 6.4(b) and 6.4(c), which occur at similar later times, have similar areas near $\sim$150 mm^2. Equivalent-area diameters, calculated with $d_{eq} = \sqrt{4A/\pi}$, of 11.8 mm, 14.6 mm, and 13.5 mm are obtained from the flame regions in Figs. 6.4(a), 6.4(b), and 6.4(c), respectively. This observed growth trend and the quantitative size values are in excellent agreement with the aforementioned niacin ignition study [108], which reported a size increase of 10 mm to 15 mm from 7 ms to 9 ms after the spark.

The flame front contour in Fig. 6.4 that encloses the segmented flame region is color coded by the curvature value, H, that was calculated with Eq. 6.2. The color scale in Fig. 6.4 does not cover the full range of measurements, but is instead truncated to show the subtle changes between positive and negative curvature along the flame front. The flame front contour clearly distinguishes the convex and concave regions of the flattened flame plume, with the absolute value of the curvature increasing with the tightness of bends along the path. Cusp and corner features are observed in an alternating fashion along the flame front path, with sharper bends often appearing in close proximity.

Curvature histograms, which approximate the continuous probability density function (PDF), are shown in Fig. 6.4 to depict the full distribution of curvature values. Curvature statistics, including the mean (μ) and median (m_e) curvature values, are also reported to determine general trends for the three flames. From the histograms, it can be seen that the curvature distributions are roughly symmetric and centered near zero, spanning values between $\pm$ 3 mm^{-1}. The curvature statistics reveal that all three distributions are right skewed, corresponding to a distribution with $\mu > m_e$. The right-skewed distributions suggest a preferential flame shape that is convex on average to the unburnt reactant region, and therefore show evidence for an expanding flame surface even without time-resolved flame images. The histograms also indicate a rough balance of positive and negative curvatures, although the conditions that may influence this balance are still unclear.

6.3.2 Elongated-Plume Morphologies

Three processed OH-PLIF images, showing qualitatively different "elongated-plume" morphologies, can be seen in Fig. 6.5. These images are similarly organized by increasing time delay (Δt), and include the run number, the SNR calculated with Eq. 6.1, and a scale bar. Compared to the flattened-plume shapes shown in Fig. 6.3, the flame regions in Fig. 6.5 are instead generally elongated in the height direction. An irregularly-shaped flame front is still observed, but the reaction zone is now partially or fully separated into flame regions of different sizes. Small speckles can also be seen throughout the background region, corresponding to scattering of the fluorescence signal from unburnt particles.

The elongated plumes also show a characteristic flame region that extends between and below the electrodes. This region likely corresponds to the region where the flame is initiated due to the spark discharge. Due to the convective processes mentioned previously, the flame preferentially expands in the positive-vertical direction. Nevertheless, the OH-PLIF signal found underneath the electrodes emphasizes the importance of the local fuel distribution in the ignition zone.

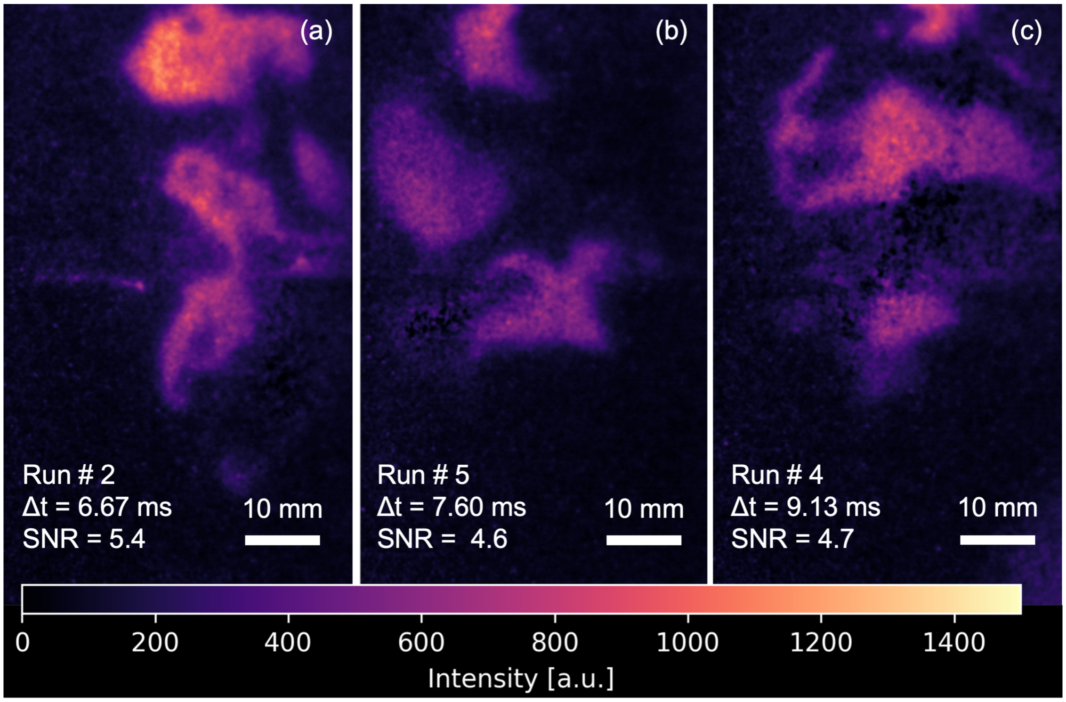

Figure 6.5: Processed OH-PLIF images showing the elongated-plume morphology. The images from (a) run # 2, (b) run # 5, and (c) run # 4 include the time delay (Δt) and the signal-to-noise-ratio (SNR). The scale bars indicate a 10-mm linear distance.

The elongated plumes in Fig. 6.5 present lower OH signal intensities than the flattened-plumes observed in Fig. 6.5, with values up to $\sim$1500 counts. A mean SNR of 4.9 is calculated, which is nearly half the mean value for the flattened-plume OH-PLIF images. The low signal in the flame regions and the high degree of fluorescence scattering in the background regions result in a consistently-reduced SNR. These patterns may arise from particular configurations of the of the dust cloud or the ignition event that differ from the flattened-plumes. Simultaneously-implemented diagnostics, such as PIV, may be helpful to investigate the complex interactions between the particles in the dust cloud, the dispersing flow, and the reaction zone.

The area measurements extracted from the three elongated-plumes are shown in Fig. 6.6. For these images, only the largest flame region was measured. Since the elongated plumes have a disconnected structure that produces flame regions of varying size, the variability of the measured flame area is large when compared to the flattened plumes. Prominent cusp and corner structures are also seen along the flame front contours in Figs. 6.6(a) and 6.6(c). Despite this, the mean curvature values for the three flame regions are still positive, which corresponds to a positive average radius of curvature and an expanding flame surface. Similar to the flattened plumes, the curvature distributions for the three flame regions are right skewed, with $\mu > m_e$.

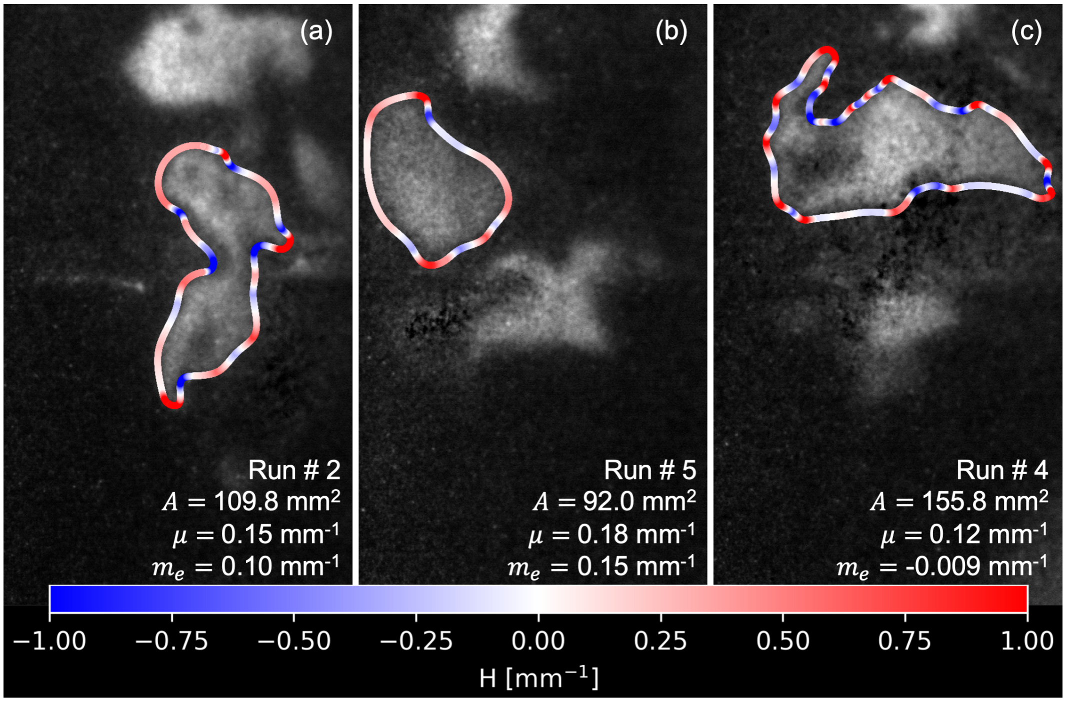

Figure 6.6: Elongated-plume OH-PLIF images showing quantitative morphology measurements. The images from (a) run # 2, (b) run # 5, and (c) run # 4 include the flame front curvature contour, the flame area (A), the mean curvature (μ), and the median curvature (m_e).

The curvature histograms for the three elongated plumes are shown in Fig. 6.7. The histograms show curvature values between 2.5–5.5 mm^{-1}, which is a wider range than that observed in the flattened plumes, but this affect seems to be primarily driven by the sharp corner area found in

Fig 6.6(c). The histograms demonstrate how cusp and corner areas cause the distribution to shift in shape. The multiple sharp cusps in Fig. 6.6(a) cause the corresponding histogram to broaden on the negative side, while the intensely sharp corner in Fig. 6.6(c) extends the far end of the distribution tail toward the positive side. Nevertheless, the central locations of the distributions remain very similar. No clear trend in the evolution of the curvature histogram from earlier to later times is identified. In potential follow-on studies, time-resolved OH-PLIF studies may be helpful for tracking the evolution of the curvature distribution over time.

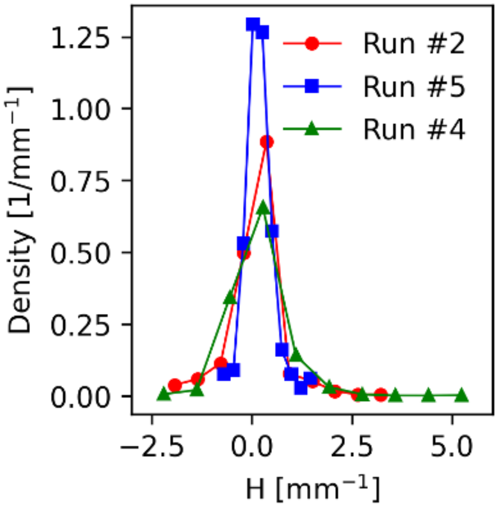

Figure 6.7: Histograms showing the distribution of curvatures along the elongated-plume flame front for run # 2, run # 5, and run # 4.

It is unclear whether the proposed morphology categories accurately represent the full range of observable niacin flame behavior. A broad continuum of morphologies may arise from different flow and ignition conditions. The features highlighted in this work may also be explained by the planar nature of the measurement. For example, the disconnected flame regions observed in Fig. 6.5 may actually be part of a continuous flame that extends beyond the OH PLIF measurement section.

6.3.3 *Average OH-PLIF Distribution*

The remaining OH-PLIF images are combined with the ones presented above to form an mean OH-PLIF image, whereby the intensity value at each pixel in the experimental FOV is the arithmetic mean value of that pixel across the stack of ten processed OH-PLIF images. The mean OH-PLIF image, which can be seen in Fig. 6.8, is used to assess the average distribution of OH signal in the experimental FOV. The mean OH-PLIF image shows more OH signal above the electrodes, with the maximum occurring ∼8 mm above the electrode surface. Vertical line profiles are also extracted and plotted in Fig. 6.8, which show the average OH-PLIF signal intensity along the centerline and along right and left offset positions.

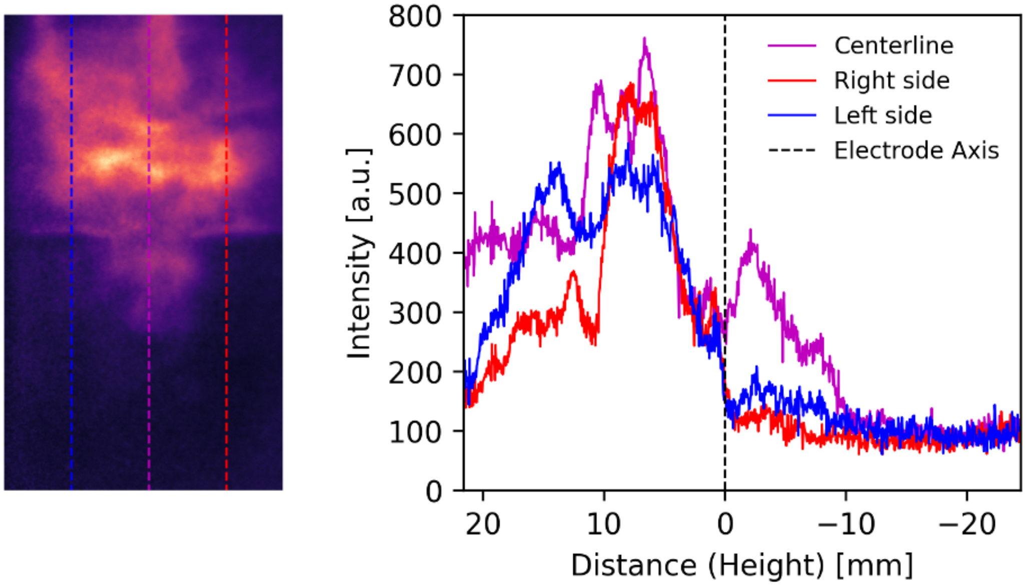

Figure 6.8: Left: Mean OH-PLIF image showing the line-profile positions. Right: Centerline, offset-right, and offset-left line profiles from the mean OH-PLIF image.

The centerline profile shows OH signal appearing underneath the electrodes, with values slowly decaying to the background value by ∼10 mm below the electrode axis. The right-side offset profile shows less OH signal than the left-side offset profile, in the region from 10-20 mm above the electrode axis. This behavior corroborates a similar observation made in the chemiluminescence study where flame kernel motion favored the left, or moving electrode, side of the ignition zone.

It was suggested that this preferential combustion behavior was produced by local asymmetries induced by the moving electrode in the initial stages of the ignition process [108].

6.4 OH-PLIF Conclusions

The present work constitutes a detailed investigation of niacin dust cloud combustion in the MIKE3 device. OH-PLIF was successfully implemented in the challenging dust cloud environment for qualitative flame structure visualization and quantitative flame area and 2D curvature measurements. The OH-PLIF analysis revealed different niacin dust flame morphology categories, namely flattened plumes and elongated plumes. The flattened plumes presented mostly continuous flame regions, relatively large SNR values, and positively skewed curvature distributions. The elongated plumes presented disconnected flame regions with lower SNR values, and showed wider but still positively-skewed curvature distributions. The mean OH-PLIF image also showed the maximum OH signal $\sim$8 mm above the electrodes. OH signal underneath the electrodes was observed until $\sim$10 mm below the electrode axis. Finally, OH signal was more abundant on the moving electrode side of the ignition area.

Additional investigations are required to assess the impact of the stochastic dust cloud on the laser sheet intensity distribution and the feasibility of implementing intensity corrections for dust flame OH-PLIF data. Furthermore, the dependence of the measured OH-signal on dust sample properties and the selected mass loading must be considered when comparing OH-PLIF images at different conditions.

7. SUMMARY

In this work, we have successfully implemented DIH, PIV, chemiluminescence imaging, and OH-PLIF diagnostics to conduct detailed investigations of the dust cloud dispersion, ignition, and flame propagation processes inside the MIKE3 device. Firstly, DIH was implemented to monitor the particle dynamics in the region between the MIKE3 ignition electrodes. In-situ particle size, concentration, and velocity data were obtained near the critical time when ignition would typically occur. The measurements from borosilicate and soda-lime glass clearly demonstrated that different dust materials and size distributions can give rise to different particle conditions in the ignition zone. Thus, the findings from this study suggest that the state of the dust cloud prior to ignition is a fundamental factor that explains differences in ignitability between dusts.

In the second study, DIH and PIV were coupled to investigate aluminum dust cloud dispersions in the MIKE3 glass tube. This application of multiple laser diagnostic methods addressed the need for both particle and flow data to more-comprehensively characterize the dust cloud prior to ignition. The in-situ particle and flow data from a large number of experiments were then used to demonstrate that the pre-ignition state of the dust cloud can be robustly characterized with distribution and statistical analyses. The particle size distribution obtained by measuring the dispersed aluminum dust clouds was found to be well characterized by the lognormal distributon, while the planar particle velocity distribution agreed well with the Weibull distribution. Furthermore, the particle size distribution obtained in this worked showed good agreement with the ex-situ particle size distribution for small sizes but not for larger ones, indicating the importance of in-situ measurements for accurately characterizing the dust cloud in the ignition zone.

In the third study, broadband and chemiluminescence imaging diagnostics were implemented to investigate the early flame kernel development process from spark-ignited niacin and aluminum dust clouds. The qualitative flame structure observations and quantitative flame kernel growth and motion measurements demonstrated how dust cloud ignitability can be probed with time-resolved and spectrally-selective imaging diagnostics. Using broadband, OH*, and CH* chemiluminescence imaging configurations, the evolution of the flame kernel for the first 10 ms after the spark was analyzed. An asymmetric flame kernel motion away from the central ignition region was discovered, with such behavior being possibly influenced by the moving-electrode spark circuit.

In the final study, OH-PLIF was implemented to investigate the flame structure of burning niacin dust clouds in the MIKE3 device. The OH-PLIF images, which were corrected to remove interference from OH* chemiluminescence, showed irregularly-shaped and non-uniform reaction zones. Two flame morphology categories were proposed based on qualitative differences in the visual appearance of the flame regions, namely "flattened plumes" and "elongated plumes". Quantitative flame area and 2D curvature measurements showed evidence for an expanding flame surface, even without time-resolved imaging capability. Additionally, the mean OH distribution in the ignition zone corroborated the asymmetric flame propagation that was observed in the previous study.

The dust cloud dispersion, ignition, and flame propagation processes that compose dust explosions are complex and difficult to comprehensively investigate. The combination of advanced optical diagnostics implemented in the novel experiments of this work enabled each of these processes to be analyzed. The dispersion process prior to ignition was characterized with DIH and PIV, the ignition process and flame kernel development were characterized with chemiluminescence imaging, and the reaction zone and flame propagation were characterized with OH-PLIF. Hence, this work broadly expands the current knowledge of the physics and chemistry of dust explosions. Furthermore, these unique experiments were conducted using the MIKE3 device over a wide range of material types and testing conditions. Therefore, fundamental insights are obtained within the standardized safety testing framework that is familiar and relevant to industry.

REFERENCES

[1] Z. Yuan, N. Khakzad, F. Khan, and P. Amyotte, “Dust explosions: A threat to the process industries,” *Process Safety and Environmental Protection*, vol. 98, pp. 57–71, Nov. 2015.

[2] U. S. Chemical Safety and Hazard Investigation Board, “Investigation Report: Combustible Dust Hazard Study,” Report 2006-H-1, United States. Chemical Safety and Hazard Investigation Board, 2006.

[3] G. Joseph, “Combustible dusts: A serious industrial hazard,” *Journal of Hazardous Materials*, vol. 142, pp. 589–591, Apr. 2007.

[4] C. Cloney, “2021 Mid-Year Combustible Dust Incident Report,” Report Version #1, DustEx Research Ltd., 2021.

[5] R. K. Eckhoff, *Dust explosions in the process industries*. Gulf Professional Pub, 3rd ed., 2003.

[6] P. R. Amyotte and R. K. Eckhoff, “Dust explosion causation, prevention and mitigation: An overview,” *Journal of Chemical Health and Safety*, vol. 17, pp. 15–28, Jan. 2010.

[7] D. Frurip, L. Britton, W. Fenlon, J. Going, B. K. Harrison, J. Niemeier, and E. A. Ural, “The role of ASTM E27 methods in hazard assessment: Part I. Thermal stability, compatibility, and energy release estimation methods,” *Process Safety Progress*, vol. 23, pp. 266–278, Dec. 2004.

[8] L. G. Britton, K. L. Cashdollar, W. Fenlon, D. Frurip, J. Going, B. K. Harrison, J. Niemeier, and E. A. Ural, “The role of ASTM E27 methods in hazard assessment part II: Flammability and ignitability,” *Process Safety Progress*, vol. 24, pp. 12–28, Mar. 2005.

[9] Center for Chemical Process Safety, *Guidelines for risk based process safety*. Hoboken, N.J: Wiley-Interscience, 2007.

[10] R. Ogle, *Dust explosion dynamics*. Amsterdam: Elsevier ; Butterworth-Heinemann, 2017.

[11] ASTM E2019-03(2019, “Test Method for Minimum Ignition Energy of a Dust Cloud in Air,” 2003.

[12] ISO/IEC 80079-20-2 , “Explosive atmospheres – Part 20-2: Material characteristics – Combustible dusts test methods,” 2016.

[13] “Calibration-Round-Robin CaRo21 Final Report,” Report B054_248, Cesana AG, Bettingen, Switzerland, 2022.

[14] National Fire Protection Association, *NFPA 652: Standard on the fundamentals of combustible dust.* 2019.

[15] P. B. Kowalczuk and J. Drzymala, “Physical meaning of the Sauter mean diameter of spherical particulate matter,” *Particulate Science and Technology*, vol. 34, pp. 645–647, Nov. 2016.

[16] Seymour Lowell and Joan E. Shields, *Powder Surface Area and Porosity*. Springer Dordrecht, 3rd ed ed., Nov. 2013.

[17] M. Modarres, *Risk Analysis in Engineering: Techniques, Tools, and Trends*. CRC Press, 2016.

[18] S. Kaplan and B. J. Garrick, “On The Quantitative Definition of Risk,” *Risk Analysis*, vol. 1, no. 1, pp. 11–27, 1981.

[19] D. A. Crowl, *Chemical process safety: fundamentals with applications*. Boston, MA: Pearson Education, Inc, 4th ed., 2019.

[20] A. R. Boyle and F. J. Llewellyn, “The electrostatic ignitibility of dust clouds and powders,” *Journal of the Society of Chemical Industry*, vol. 69, no. 6, pp. 173–181, 1950.

[21] L. E. Line, H. A. Rhodes, and T. E. Gilmer, “The Spark Ignition of Dust Clouds.,” *The Journal of Physical Chemistry*, vol. 63, pp. 290–294, Feb. 1959.

[22] M. Mittal, “Explosion characteristics of micron- and nano-size magnesium powders,” *Journal of Loss Prevention in the Process Industries*, vol. 27, pp. 55–64, Jan. 2014.

[23] P. Bagaria, J. Zhang, and C. Mashuga, “Effect of dust dispersion on particle breakage and size distribution in the minimum ignition energy apparatus,” *Journal of Loss Prevention in the Process Industries*, vol. 56, pp. 518–523, Nov. 2018.

[24] P. Bagaria, B. Hall, A. Dastidar, and C. Mashuga, “Effect of particle size reduction due to

dust dispersion on minimum ignition energy (MIE)," *Powder Technology*, vol. 356, pp. 304–309, Nov. 2019.

[25] D. Castellanos, P. Bagaria, and C. V. Mashuga, "Effect of particle size polydispersity on dust cloud minimum ignition energy," *Powder Technology*, vol. 367, pp. 782–787, May 2020.

[26] G. O. Thomas, G. Oakley, and J. D. o. P. Brenton, "Influence of the morphology of lycopodium dust on its minimum ignition energy," *Combustion and Flame; (United States)*, vol. 85:3, June 1991.

[27] P. Bagaria, S. Prasad, J. Sun, R. Bellair, and C. Mashuga, "Effect of particle morphology on dust minimum ignition energy," *Powder Technology*, vol. 355, pp. 1–6, Oct. 2019.

[28] N. S. Reding, T. M. Farrell, A. Verma, and M. B. Shiflett, "Effect of particle morphology on metal dust deflagration sensitivity and severity," *Journal of Loss Prevention in the Process Industries*, vol. 70, p. 104396, May 2021.

[29] R. K. Eckhoff, "Towards absolute minimum ignition energies for dust clouds?," *Combustion and Flame*, vol. 24, pp. 53–64, Feb. 1975.

[30] R. K. Eckhoff and G. Enstad, "Why are "long" electric sparks more effective dust explosion initiators than "short" ones?," *Combustion and Flame*, vol. 27, pp. 129–131, Aug. 1976.

[31] E. Randeberg and R. K. Eckhoff, "Initiation of dust explosions by electric spark discharges triggered by the explosive dust cloud itself," *Journal of Loss Prevention in the Process Industries*, vol. 19, pp. 154–160, Mar. 2006.

[32] G. Ackroyd, M. Bailey, and R. Mullins, "The effect of reduced oxygen levels on the electrostatic ignition sensitivity of dusts," *Journal of Physics: Conference Series*, vol. 301, p. 012034, June 2011.

[33] P. Chaudhari and C. V. Mashuga, "Partial inerting of dust clouds using a modified standard minimum ignition energy device," *Journal of Loss Prevention in the Process Industries*, vol. 48, pp. 145–150, July 2017.

[34] P. Chaudhari, B. Ravi, P. Bagaria, and C. Mashuga, "Improved partial inerting MIE test method for combustible dusts and its CFD validation," *Process Safety and Environmental*

Protection, vol. 122, pp. 192–199, Feb. 2019.

[35] P. R. Amyotte, S. Chippett, and M. J. Pegg, "Effects of turbulence on dust explosions," *Progress in Energy and Combustion Science*, vol. 14, pp. 293–310, Jan. 1988.

[36] G. E. P. Box, J. S. Hunter, and W. G. Hunter, *Statistics for experimenters: design, innovation, and discovery*. Wiley-Interscience, 2nd ed., 2005.

[37] J. J. Shynk, *Probability, Random Variables, and Random Processes: Theory and Signal Processing Applications*. John Wiley & Sons, Incorporated, 2012.

[38] C. R. Rao, G. Kallianpur, P. R. Krishnaiah, and J. K. Ghosh, eds., *Statistics and probability: essays in honor of C.R. Rao*. Amsterdam ; New York : New York: North-Holland Pub. Co. ; Sole distributors for the U.S.A. and Canada, Elsevier North-Holland, 1982.

[39] R. Xu, *Particle characterization: light scattering methods*. Dordrecht London: Kluwer Academic, 2000.

[40] M. Alderliesten, "Mean Particle Diameters. Part I: Evaluation of definition systems," *Particle & Particle Systems Characterization*, vol. 7, no. 1-4, pp. 233–241, 1990.

[41] M. Alderliesten, "Mean Particle Diameters. from Statistical Definition to Physical Understanding," *Journal of Biopharmaceutical Statistics*, vol. 15, pp. 295–325, Mar. 2005.

[42] J. Katz and J. Sheng, "Applications of Holography in Fluid Mechanics and Particle Dynamics," *Annual Review of Fluid Mechanics*, vol. 42, pp. 531–555, Jan. 2010.

[43] D. Gabor, "A New Microscopic Principle," *Nature*, vol. 161, pp. 777–778, May 1948.

[44] J. P. Fugal, R. A. Shaw, E. W. Saw, and A. V. Sergeyev, "Airborne digital holographic system for cloud particle measurements," *Applied Optics*, vol. 43, pp. 5987–5995, Nov. 2004.

[45] J. Sheng, E. Malkiel, J. Katz, J. Adolf, R. Belas, and A. R. Place, "Digital holographic microscopy reveals prey-induced changes in swimming behavior of predatory dinoflagellates," *Proceedings of the National Academy of Sciences*, vol. 104, pp. 17512–17517, Oct. 2007.

[46] D. W. Pfitsch, E. Malkiel, M. Takagi, Y. Ronzhes, S. King, J. Sheng, and J. Katz, "Analysis of In-situ Microscopic Organism Behavior in Data Acquired Using a Free-drifting Submersible Holographic Imaging System," in *OCEANS 2007*, pp. 1–8, Sept. 2007.

[47] L. Tian, N. Loomis, J. A. Domínguez-Caballero, and G. Barbastathis, “Quantitative measurement of size and three-dimensional position of fast-moving bubbles in air-water mixture flows using digital holography,” *Applied Optics*, vol. 49, pp. 1549–1554, Mar. 2010.

[48] F. Lamadie, L. Bruel, and M. Himbert, “Digital holographic measurement of liquid–liquid two-phase flows,” *Optics and Lasers in Engineering*, vol. 50, pp. 1716–1725, Dec. 2012.

[49] D. R. Guildenbecher, M. A. Cooper, W. Gill, H. L. Stauffacher, M. S. Oliver, and T. W. Grasser, “Quantitative, three-dimensional imaging of aluminum drop combustion in solid propellant plumes via digital in-line holography,” *Optics Letters*, vol. 39, pp. 5126–5129, Sept. 2014.

[50] N. A. Buchmann, C. Atkinson, and J. Soria, “Ultra-high-speed tomographic digital holographic velocimetry in supersonic particle-laden jet flows,” *Measurement Science and Technology*, vol. 24, p. 024005, Dec. 2012.

[51] D. R. Guildenbecher, M. A. Cooper, and P. E. Sojka, “High-speed (20 kHz) digital in-line holography for transient particle tracking and sizing in multiphase flows,” *Applied Optics*, vol. 55, pp. 2892–2903, Apr. 2016.

[52] T. Latychevskaia and H.-W. Fink, “Practical algorithms for simulation and reconstruction of digital in-line holograms,” *Applied Optics*, vol. 54, pp. 2424–2434, Mar. 2015.

[53] D. R. Guildenbecher, “Sandia Particle Holography Processor v. 1.0,” Tech. Rep. HOLOSAND V.1.0; 003893MLTPL00, Sandia National Laboratory, Dec. 2015.

[54] R. J. Adrian and J. Westerweel, *Particle Image Velocimetry*. Cambridge University Press, 2011.

[55] J. Westerweel, G. E. Elsinga, and R. J. Adrian, “Particle Image Velocimetry for Complex and Turbulent Flows,” *Annual Review of Fluid Mechanics*, vol. 45, pp. 409–436, Jan. 2013.

[56] C. Dennis and B. Bojko, “On the combustion of heterogeneous AP/HTPB composite propellants: A review,” *Fuel*, vol. 254, p. 115646, Oct. 2019.

[57] J. H. Glover, “Chemiluminescence in gas analysis and flame-emission spectrometry. A review,” *The Analyst*, vol. 100, no. 1192, p. 449, 1975.

[58] P. Parajuli, T. T. Paschal, M. A. Turner, Y. Wang, E. L. Petersen, and W. D. Kulatilaka, "High-Speed Hydroxyl and Methylidyne Chemiluminescence Imaging Diagnostics in Spherically Expanding Flames," *AIAA Journal*, pp. 1–9, June 2021.

[59] Y. Liu, J. Tan, M. Wan, L. Zhang, and X. Yao, "Quantitative Measurement of OH* and CH* Chemiluminescence in Jet Diffusion Flames," *ACS Omega*, vol. 5, pp. 15922–15930, July 2020.

[60] D. R. Crosley and G. P. Smith, "Laser-Induced Fluorescence Spectroscopy For Combustion Diagnostics," *Optical Engineering*, vol. 22, p. 545, Oct. 1983.

[61] R. K. Hanson, "Planar laser-induced fluorescence imaging," *Journal of Quantitative Spectroscopy and Radiative Transfer*, vol. 40, pp. 343–362, Sept. 1988.

[62] A. C. Eckbreth, *Laser diagnostics for combustion temperature and species*. No. 3, New York: Gordon and Breach Publ, 2nd ed., 1996.

[63] ASTM E1226-12a, "Test Method for Explosibility of Dust Clouds."

[64] ASTM E1491-06(2019), "Test Method for Minimum Autoignition Temperature of Dust Clouds."

[65] A. E1515-14, "Test Method for Minimum Explosible Concentration of Combustible Dusts."

[66] A. E2931-13(2019), "Test Method for Limiting Oxygen (Oxidant) Concentration of Combustible Dust Clouds."

[67] R. K. Eckhoff, "Ignition of Combustible Dust Clouds by Strong Capacitive Electric Sparks of Short Discharge Times," *Zeitschrift für Physikalische Chemie*, vol. 231, no. 10, pp. 1683–1707, 2017.

[68] R. Eckhoff, "Current status and expected future trends in dust explosion research," *Journal of Loss Prevention in the Process Industries*, vol. 18, pp. 225–237, July 2005.

[69] U. Schnars and W. Jueptner, *Digital holography: digital hologram recording, numerical reconstruction, and related techniques*. Berlin: Springer, 2005.

[70] S. Wang, Y. Pu, F. Jia, A. Gutkowski, and J. Jarosinski, "AN EXPERIMENTAL STUDY ON FLAME PROPAGATION IN CORNSTARCH DUST CLOUDS," *Combustion Science*

and Technology, vol. 178, pp. 1957–1975, Dec. 2006.

[71] C. Murillo, O. Dufaud, N. Bardin-Monnier, O. López, F. Munoz, and L. Perrin, “Dust explosions: CFD modeling as a tool to characterize the relevant parameters of the dust dispersion,” *Chemical Engineering Science*, vol. 104, pp. 103–116, Dec. 2013.

[72] Y. Wu, X. Wu, L. Yao, M. Brunel, S. Coëtmellec, D. Lebrun, G. Gréhan, and K. Cen, “3D boundary line measurement of irregular particle with digital holography,” *Powder Technology*, vol. 295, pp. 96–103, July 2016.

[73] Y. Wu, X. Wu, L. Yao, Z. Xue, C. Wu, H. Zhou, and K. Cen, “Simultaneous particle size and 3D position measurements of pulverized coal flame with digital inline holography,” *Fuel*, vol. 195, pp. 12–22, May 2017.

[74] X. Wu, L. Yao, Y. Wu, X. Lin, L. Chen, J. Chen, X. Gao, and K. Cen, “In-Situ Characterization of Coal Particle Combustion via Long Working Distance Digital In-Line Holography,” *Energy & Fuels*, vol. 32, pp. 8277–8286, Aug. 2018.

[75] X. Wu, Q. Jin, L. Zhao, X. Lin, Y. Wu, and Y. Zhou, “Digital holographic sizer for coal powder size distribution measurement: preliminary simulation and experiment,” *Measurement Science and Technology*, vol. 29, p. 124001, Dec. 2018.

[76] D. R. Guildenbecher, J. Gao, P. L. Reu, and J. Chen, “Digital holography simulations and experiments to quantify the accuracy of 3D particle location and 2D sizing using a proposed hybrid method,” *Applied Optics*, vol. 52, pp. 3790–3801, June 2013.

[77] J. Gao, D. R. Guildenbecher, P. L. Reu, and J. Chen, “Uncertainty characterization of particle depth measurement using digital in-line holography and the hybrid method,” *Optics Express*, vol. 21, p. 26432, Nov. 2013.

[78] Z. Falgout, Y. Chen, and D. R. Guildenbecher, “Improving the spatial dynamic range of digital inline particle holography,” *Applied Optics*, vol. 58, pp. A65–A73, Feb. 2019.

[79] C. Schweizer, S. Prasad, A. Saini, C. V. Mashuga, and W. D. Kulatilaka, “High-speed digital in-line holography for in-situ dust cloud characterization in a minimum ignition energy device,” *Powder Technology*, vol. 376, pp. 612–621, Oct. 2020.

[80] S. Prasad, C. Schweizer, P. Bagaria, A. Saini, W. D. Kulatilaka, and C. V. Mashuga, "Investigation of particle density on dust cloud dynamics in a minimum ignition energy apparatus using digital in-line holography," *Powder Technology*, vol. 384, pp. 297–303, May 2021.

[81] S. Prasad, C. Schweizer, P. Bagaria, W. D. Kulatilaka, and C. V. Mashuga, "Effect of particle morphology on dust cloud dynamics," *Powder Technology*, vol. 379, pp. 89–95, Feb. 2021.

[82] C. Schweizer, Y. Wang, C. V. Mashuga, and W. D. Kulatilaka, "Combustible Dust Cloud Characterization Using Multiple Laser Diagnostic Methods," in *AIAA SciTech 2021 Forum*, American Institute of Aeronautics and Astronautics, Jan. 2021.

[83] J. Taveau, S. Hochgreb, S. Lemkowitz, and D. Roekaerts, "Explosion hazards of aluminum finishing operations," *Journal of Loss Prevention in the Process Industries*, vol. 51, pp. 84–93, Jan. 2018.

[84] C. Tropea, A. L. Yarin, and J. F. Foss, eds., *Springer handbook of experimental fluid mechanics*. Springer handbooks, Berlin: Springer, 1st ed., 2007.

[85] M. Conde-Fontenla, C. Paz, M. Concheiro, and G. Ribatski, "On the width and mean value of bubble size distributions under subcooled flow boiling," *Experimental Thermal and Fluid Science*, vol. 124, p. 110368, June 2021.

[86] L. P. Zhang and Y. Y. Zhao, "Particle size distribution of tin powder produced by centrifugal atomisation using rotating cups," *Powder Technology*, vol. 318, pp. 62–67, Aug. 2017.

[87] J. E. Smith and M. L. Jordan, "Mathematical and graphical interpretation of the log-normal law for particle size distribution analysis," *Journal of Colloid Science*, vol. 19, pp. 549–559, Aug. 1964.

[88] A. H. Monahan, "The Probability Distribution of Sea Surface Wind Speeds. Part II: Dataset Intercomparison and Seasonal Variability," *Journal of Climate*, vol. 19, pp. 521–534, Feb. 2006.

[89] A. H. Monahan, Y. He, N. McFarlane, and A. Dai, "The Probability Distribution of Land Surface Wind Speeds," *Journal of Climate*, vol. 24, pp. 3892–3909, Aug. 2011.

[90] A. E. Berg, M. G. Christiansen, B. V. Balakin, and P. Kosinski, "Investigation of dust disper-

sion in a modified Hartmann tube using positron emission particle tracking and simulations," *Journal of Loss Prevention in the Process Industries*, vol. 55, pp. 178–190, Sept. 2018.

[91] S. Hosseinzadeh, M. Vanierschot, F. Norman, F. Verplaetsen, and J. Berghmans, "Flame propagation and flow field measurements in a Hartmann dust explosion tube," *Powder Technology*, vol. 323, pp. 346–356, Jan. 2018.

[92] S. G. Davis, P. C. Hinze, O. R. Hansen, and K. van Wingerden, "Does your facility have a dust problem: Methods for evaluating dust explosion hazards," *Journal of Loss Prevention in the Process Industries*, vol. 24, pp. 837–846, Nov. 2011.

[93] C. Schweizer, C. V. Mashuga, and W. D. Kulatilaka, "Investigation of aluminum dust cloud dispersion characteristics in an explosion hazard testing device using laser-based particle and flow diagnostics," *Process Safety and Environmental Protection*, vol. 166, pp. 310–319, Oct. 2022.

[94] P.-J. Chang, T. Mogi, and R. Dobashi, "An investigation on the dust explosion of micron and nano scale aluminium particles," *Journal of Loss Prevention in the Process Industries*, vol. 70, p. 104437, May 2021.

[95] B. Han, G. Li, C. Yuan, and Q. Wang, "Flame propagation of corn starch in a modified Hartmann tube with branch structure," *Powder Technology*, vol. 360, pp. 10–20, Jan. 2020.

[96] R. Dobashi and K. Senda, "Detailed analysis of flame propagation during dust explosions by UV band observations," *Journal of Loss Prevention in the Process Industries*, vol. 19, pp. 149–153, Mar. 2006.

[97] W. Gao, T. Mogi, J. Sun, and R. Dobashi, "Effects of particle thermal characteristics on flame structures during dust explosions of three long-chain monobasic alcohols in an open-space chamber," *Fuel*, vol. 113, pp. 86–96, Nov. 2013.

[98] T. Skjold, K. L. Olsen, and D. Castellanos, "A constant pressure dust explosion experiment," *Journal of Loss Prevention in the Process Industries*, vol. 26, pp. 562–570, May 2013.

[99] P. Julien, J. Vickery, S. Goroshin, D. L. Frost, and J. M. Bergthorson, "Freely-propagating flames in aluminum dust clouds," *Combustion and Flame*, vol. 162, pp. 4241–4253, Nov.

2015.

[100] M. O'Neil, N. A. Niemiec, A. R. Demko, E. L. Petersen, and W. D. Kulatilaka, "Laser-induced-breakdown-spectroscopy-based detection of metal particles released into the air during combustion of solid propellants," *Applied Optics*, vol. 57, p. 1910, Mar. 2018.

[101] M. O'Neil, A. Demko, E. L. Petersen, and W. D. Kulatilaka, "Ultrashort-pulse laser-induced breakdown spectroscopy for detecting airborne metals during energetic reactions," *Applied Optics*, vol. 58, pp. C79–C83, Apr. 2019.

[102] "Calibration-Round-Robin CaRo17 Final Report," Report B054_048, Cesana AG, Bettingen, Switzerland, 2018.

[103] S. v. d. Walt, J. L. Schönberger, J. Nunez-Iglesias, F. Boulogne, J. D. Warner, N. Yager, E. Gouillart, and T. Yu, "scikit-image: image processing in Python," *PeerJ*, vol. 2, p. e453, June 2014.

[104] W. Gao, T. Mogi, J. Yu, X. Yan, J. Sun, and R. Dobashi, "Flame propagation mechanisms in dust explosions," *Journal of Loss Prevention in the Process Industries*, vol. 36, pp. 186–194, July 2015.

[105] T. Chen, J. Van Caneghem, J. Degrève, F. Verplaetsen, J. Berghmans, and M. Vanierschot, "A numerical model for the calculation of the minimum ignition energy of pure and mixture dust clouds," *Process Safety and Environmental Protection*, vol. 164, pp. 271–282, Aug. 2022.

[106] Y. Chen, D. R. Guildenbecher, K. N. Hoffmeister, M. A. Cooper, H. L. Stauffacher, M. S. Oliver, and E. B. Washburn, "Study of aluminum particle combustion in solid propellant plumes using digital in-line holography and imaging pyrometry," *Combustion and Flame*, vol. 182, pp. 225–237, Aug. 2017.

[107] W. Gao, T. Mogi, J. Sun, J. Yu, and R. Dobashi, "Effects of particle size distributions on flame propagation mechanism during octadecanol dust explosions," *Powder Technology*, vol. 249, pp. 168–174, Nov. 2013.

[108] C. Schweizer, C. V. Mashuga, and W. D. Kulatilaka, "Investigation of niacin and aluminum

dust cloud ignition characteristics in an explosion hazard testing device using high-speed imaging," *Process Safety and Environmental Protection*, vol. 166, pp. 320–327, Oct. 2022.

[109] Y. Wang, A. Jain, and W. Kulatilaka, "Hydroxyl radical planar imaging in flames using femtosecond laser pulses," *Applied Physics B*, vol. 125, p. 90, May 2019.

[110] S. Gashi, J. Hult, K. W. Jenkins, N. Chakraborty, S. Cant, and C. F. Kaminski, "Curvature and wrinkling of premixed flame kernels—comparisons of OH PLIF and DNS data," *Proceedings of the Combustion Institute*, vol. 30, pp. 809–817, Jan. 2005.